THE UNSTEADY FORCES ON SLENDER DELTA WING HYDROFOILS OSCILLATING IN HEAVE

Thesis by

Raymond Kay DeLong

In Partial Fulfillment of the Requirements

for the Degree of

Doctor of Philosophy

California Institute of Technology

Pasadena, California

1968

(Submitted 24 May 1968)

ACKNOWLEDGMENTS

I would first like to thank Professor Allan Acosta who served as my advisor during my graduate study and without whose assistance this thesis would not be possible.

I would also like to express my gratitude to the Institute and to Douglas Aircraft Co., Inc. (now part of McDonnell Douglas Corporation) for the financial aid received during my stay here.

In the course of my investigations I wrote letters to many people inquiring about their work. To those who were kind enough to take the time to answer I say, "Thank you".

The undertaking of any experimental investigation of the scope herein discussed must always require the participation of others. In particular I would like to thank Mr. R. Lyon of the Institute's Central Engineering Services and Messrs. C. Eastvedt, H. Hamaguchi, J. Kingan and G. Lundgren of the Hydrodynamics Laboratory.

The assistance of Miss Cecilia Lin, Mr. H. Petrie and Mr. M. Wilson in the preparation and proofreading of this manuscript is gratefully acknowledged.

And finally, to Mrs. Phyllis Henderson, former secretary for the Hydrodynamics Laboratory and still my good friend, who so excellently typed this manuscript I express my most sincere appreciation.

THE UNSTEADY FORCES ON SLENDER DELTA WING HYDROFOILS OSCILLATING IN HEAVE

by

Raymond Kay DeLong

ABSTRACT

The investigations described herein are both experimental and theoretical. An experimental technique is described by which the models tested could be oscillated sinusoidally in heave. The apparatus used to gather the unsteady lift, drag and pitching moment data is also described.

The models tested were two flat delta wings with apex angles of 15^{o} and 30^{o} and they had sharp leading edges to insure flow separation. The models were fabricated from 0.25 inch aluminum plate and were approximately one foot in length.

Three distinct types of flow were investigated: 1) fully wetted, 2) ventilated and 3) planing. The experimental data are compared with the existing theories for steady motions in the case of fully wetted delta wings. Ventilation measurements, made only for the 30^{o} model at 20^{o} angle of attack, of lift and drag are presented.

A correction of the theory proposed by M. P. Tulin for high speed planing of slender bodies is presented and it is extended to unsteady motions. This is compared to the experimental measurements made at 6^{o} and 12^{o} angle of attack for the two models previously described.

This is the first extensive measurement of unsteady drag for any shape wing, the first measurement of unsteady planing forces, the first quantitative documentation of unstable oscillations near a free surface, and the first measurements of the unsteady forces on ventilated delta wings. The results of these investigations, both theoretical and experimental, are discussed and further investigations suggested.

TABLE OF CONTENTS

I. INTRODUCTION

A. Preliminary Remarks

A hydrofoil boat is one which derives its lift force primarily from "wings" mounted to and away from the boat's hull. The lift is generated by the acceleration of the fluid surrounding the foil. This situation is very similar to an airplane flying through the atmosphere and much terminology and technique applied to hydrofoil boats has its roots in aeronautics.

Conventional boats, commonly called displacement craft, are buoyed up by the static pressure of the surrounding fluid. The boat displaces an amount of water equal to the boat's weight, hence the name displacement craft. All conventional hydrofoil boats operate in two modes. At low speeds (e.g., when docking) they operate as displacement craft and may or may not have their foils retracted. At higher speeds (e.g., design cruise) the hull is lifted clear of the water and the entire force is generated by the hydrofoil system. In this mode the craft is said to be "flying".

The idea of using hydrofoils on boats is not new. It was first considered prior to the turn of the century. Even in 1919 Alexander Graham Bell, who is considerably more famous for another achievement, had built and operated a hydrofoil boat capable of 60 knots.

Much more recently, however, a resurgence of interest in hydrofoil craft has taken place. This interest stems for all applications from one basic advantage afforded by the hydrofoil system

over displacement craft. Displacement craft operate on the surface of the water and as a result are greatly affected by the surface waves generated by wind, other boats, etc. A hydrofoil boat can operate with its hull above the wave crests and its foils submerged far enough so that the waves affect the lift to a negligible extent. The result is that a hydrofoil boat has better seakeeping capability at high speeds than does a displacement craft.

This increased immunity to surface conditions is beneficial in both military and commercial applications. Currently the most likely military application is as a submarine chaser where the hydrofoil craft's ability to travel at high speeds in relatively rougher seas makes it a better choice. In commercial applications the dimunition of the wave influence gives a smoother ride. The decreased loading allows less fortress-like designs; indeed, since the craft operates somewhat like an airplane it must necessarily be built as light as possible, otherwise the operating range would suffer from the extra weight.

Various hydrofoil configurations are popularly used. These are described in the voluminous monograph of Abramson, et al (1). There are several basic types of foils used in various combinations. These are planing, deeply submerged and surface piercing. The total lift generated by the foils is not affected by their placement since the lift generated must in any event equal the weight of the craft.

The types of foils used and their arrangement will govern the stability of the craft, however. A planing foil has stability as long as the leading edge is never submerged because of the change in wetted

area but is obviously severely affected by the surface waves. A submerged foil will experience a decrease in lift as it nears the free surface but the effect is slight unless the foil is less than a fraction of a chord from the surface. Ladder foils and surface-piercing V-foils are much better in that they can be designed to give whatever quasi-steady stability is desired.

The type of stability discussed in the previous paragraph concerned the craft's natural tendency to return to the trim condition when perturbed. If the craft is suspended at three non-collinear points and the foils at each point have heave stability, the craft will also have pitch and roll stability. The pitch and roll "stiffness" depends on the separation of the points. The greater the horizontal distance between the foils the stiffer the suspension.

So far we have only been concerned with the lift force. For a boat which is to go other than in straight lines some means must also be included to generate side force for turning. In an airplane this side force is produced by banking the wing. This can also be done on a hydrofoil boat, but due to the interaction of the free surface it usually is not. What is generally done is to have the support strut generate the side force for inverted T and inverted π foils and for V-foils differential lift in the two halves may be used to generate side force. The latter system is used on the tail of a Beechcraft Bonanza airplane.

The infinite variety of ways in which the problem of building a hydrofoil boat can be attacked is part of what makes the problem interesting. It also will suffice here to say that a detailed examination

of the designer's problems is clearly beyond the scope of these introductory remarks and the entire thesis.

We will now confine ourselves to one facet of the design of hydrofoil boats, and that is its motion about its steady flight. If the boat is caused for any reason to oscillate about its mean path, the unsteady motion of the foils will give rise to unsteady forces caused by the acceleration of their fluid environment. The interaction of these elements (i.e., fluid and foil-boat system) is commonly called hydroelasticity.

Before an analysis can be made of the motion of the craft, a quantitative specification must be made of the forces experienced by the foils for various motions. It is the endeavor of this thesis to add to the still rather sparse quantity of information regarding unsteady hydrodynamics.

This investigation has been primarily concerned with delta planform foils and as such the work of previous authors will be for the most part also concerned with delta wings. References to other work will easily be found in references (1), (2) and (3).

B. Previous Investigations

The interest in triangular lifting surfaces hardly needs justification. They are common in aeronautics and from the studies of persons whose primary interest was motivated by aeronautical consideration we will consider previous "fully wetted" flow results. As was mentioned by Smith (4) the effect of Reynolds number on the general features of the flow about sharp edged delta wings is small.

Although viscosity is the physical property which determines the smooth outflow or lateral Kutta-Joukowski condition, the absolute value of the viscosity is not too important as long as the Reynolds number is moderately high.

Prior to the interest in flows about delta wings with leading edge separation R. T. Jones (5) presented a method for calculating the force on a slender body at small angle of attack. Jones' analysis, conducted in the cross-flow plane, is applicable to slender delta wings. The cross-flow plane solution used was for a flat lamina perpendicular to the flow. The infinite velocities at the lateral edges in this model clearly do not exist in the actual case. Jones' analysis is, however, satisfactory for slender delta wings at small angles of attack and his result is often called the linear contribution since it predicts the force to be linear with angle of attack.

Subsequent experimental investigations, particularly by Roy (6), caused interest in finding a model which represented the observed flow especially the smooth outflow condition at the leading edges. Legendre (7) proposed the addition of two vortices above and inboard of the two leading edges. The strength and position of the vortices would be determined by the smooth outflow condition at the leading edges with the condition that the vortices have no net force on them. The two vortices were implicitly assumed to be joined by a cut so that the lift on the foil or foil-vortex system would be uniquely determined.

Following a suggestion by Adams (8), Legendre modified the model with the vortices being joined to their respective leading edges by cuts rather than to each other. This had the advantage that the cut

could be interpreted physically as a vortex sheet feeding the primary vortex. His force condition was still on the vortex which meant that the lift on the foil depended on whether the forces or the cuts were included or not.

Brown and Michael (9) proposed a model, anticipated by Edwards (10), which placed the zero force condition at each vortex on the cut as well. That is, the net force on the vortex and cut taken together should be zero. The ambiguity in the lift calculation was then removed.

The Brown and Michael model has served as a basis for a number of other investigations. It has the advantage of basic simplicity and it reasonably represents the flow picture. It does not, however, predict the forces very well, being somewhat too high. The stability derivatives are likewise poorly predicted.

Trying to develop a model which was even closer to the physical flow and one which would better predict the forces, Mangler and Smith (11) proposed a model with the flow separated from the leading edge being represented by a spiral vortex sheet. Somewhat better agreement with experimental data was obtained than with the Brown and Michael model. It has the disadvantage that the added complexity requires that the problem be solved on a digital computer. Smith (4) has recently published some further calculations using this model. These are used in the discussion of the experimental results in Section V.

Apart from the foregoing studies, Gersten (12) presented a method of calculating the stability derivatives for triangular wings.

Gersten's method is basically one of lifting surface theory. It has the advantage that it predicts the forces fairly well but it has the aesthetic disadvantage that the trailing vortex field of his lifting surface theory does not physically resemble the actual flow.

These are the major efforts to predict the steady forces on fully wetted delta wings. There have been other studies of the vortex structure and some flow visualization studies, particularly Marsden, et al (13), but these are the models from which most current work extends. The studies in this area are currently active as will be noted by Küchemann's (14) report on the 1964 I.U.T.A.M. symposium held at Ann Arbor, Michigan. Several of the papers, notably (15), (16) and (17), presented at this symposium have since been published in volume seven of Progress in Aeronautical Science. Also the work of Garner and Lehrian (18) is notable but is really derived from Gersten's.

In the area of unsteady loads on non-stationary delta wings Jones' idea was discussed by Miles (19) and Garrick (20) for the linear problem. The unsteady problem with leading edge separation has been treated by Randall (21) who used the Brown and Michael model to calculate the force on a slender delta wing performing infinitesimal heaving oscillations. Lowson (22) used the same model for a slender delta wing performing finite heaving oscillations. The advisability of using this model for unsteady forces seems questionable in view of the not too good agreement with steady experiments, but they seem primarily interested in vortex position and it is suggested by Maltby, et al (23) that within experimental accuracy the work of

Randall shows encouraging agreement. Due to the computational difficulties no extension of the more realistic Mangler-Smith model has been made to unsteady flows but it would undoubtedly give superior force predictions.

Another investigation of the forces on delta wings oscillating in heave was presented by Lawrence and Gerber (24). They used slender wing theory to calculate the effect of reduced frequency on the unsteady forces on some rectangular and delta wings. The theory is limited to vanishingly small angles of attack, not a very practical case, but gives surprisingly good correlation within the bounds of the theory. This is discussed in Section V.

The other two types of flow investigated herein are unique to hydrodynamics, therefore no aeronautically inspired results will be available. The second flow type (i.e., ventilated or cavitating) has received but slight treatment for delta wings. Tulin (25) has presented a theory for slender partially cavitating delta wings. This was subsequently corrected by Kaplan, et al (26). This model, though interesting, is not applicable to the current study since only a fully ventilated foil was tested.

A theory presented by Cumberbatch and Wu (27) for cavity flow past a slender pointed stationary hydrofoil reasonably depicts the flow field of the current experiment. This theory treats the cavity-foil system as a slender body so that the problem may be solved in the cross-flow plane. The pressure condition on the cavity arises from the longitudinal change in the velocity potential and this condition is satisfied on the average at a circle representing the

cavity-foil system in the cross-flow. The computational details of the theory are fairly tedious. Extension of this approach to unsteady flows would seem to be very difficult. Experimental investigations of cavitating delta wings were performed by Reichardt and Sattler (28). They indicate poor correlation with the Cumberbatch-Wu theory but due to the small size of the models the results of the experiment are not unquestioned. An experimental investigation of the forces on steady ventilated delta wings by Kiceniuk (29) indicates fairly good agreement. The problem seems to be open for more detailed research.

The third type of flow investigated herein is planing of slender delta wing hydrofoils oscillating in heave. Planing of delta wings has received little attention. Previous investigations have been popularly interested in V-bottom hulls with some work being done on rectangular skis for operation on water-based aircraft. Some delta configuration foils were investigated for use on hydro-ski aircraft but they were mounted with the apex aft. The reason for this was to decrease the initial impact loads on landing.

The one notable exception which deals with delta wings is a theory presented by Tulin (30) on the planing of slender bodies at small angles of attack. Tulin's idea for the representation of the planing cross-flow is interesting. It is unfortunate that the paper contains many errors and his final answer is believed to be incorrect which is also unfortunate since it gives a better prediction of experimental data than does the correct solution. This problem is discussed more thoroughly and corrected in Section IV of this thesis.

The problem of unsteady planing has received very little attention; the major effort has gone toward predicting impact loads on hydro-skis attached to aircraft. This area is in need of further investigation.

C. Present Investigation

In the present investiations the interest is primarily in the forces experienced by the foil during an oscillatory heaving motion. No investigations into the vortex motion were undertaken. Two models of different apex angle were tested. The apex angles were 15^{o} and 30^{o}. In the fully wetted case, a term particularly apt here, the models were oscillated in heave at different angles of attack, free stream velocity, oscillation frequency, oscillation amplitude and depth of submergence. Measurements were made of the unsteady lift and drag forces and pitching moments. With this many parameters, the data gathering and processing was time-consuming, but the lack of availability of data on these effects made the job that much more worthwhile.

The data gathered for the ventilated delta wing were limited because of the additional parameter, cavity length, and because during the course of the experiments it was learned that the 15^{o} delta wing would not ventilate properly. It was felt that the influence of the ventilation strut on the flow field over the 15^{o} model was the cause of the problem. It was decided that data would be taken only for the 30^{o} model. It was further limited to one angle of attack ($\alpha = 20^{o}$), one submergence depth (D = 0.83 chords) and one

oscillation amplitude. The term oscillation amplitude as used here applies to the heaving velocity. This means that the heaving displacement decreases with frequency.

The added parameter cavity length and associated parameters air supply rate and ventilation number cause the data gathering to still be a fairly large task especially since in all the investigations reported herein the experiment essentially had to be run twice, once with the lift and pitching moment balance and once with the drag balance. Pitching moment data are not reported for the ventilation tests because the data from both balances are required to calculate the pitching moment about a point on the model and the data were found to be so sensitive to cavity length that data at the exact conditions of the "lift" runs were not gathered for drag. Instead the drag data are for slightly different conditions.

Both models were used in the planing tests. They were run at angles of attack of six and 12 degrees. Since the forces are smaller for a planing body than for a fully wetted one the tunnel velocity was run as high as practical (i.e., U = 22 ft/sec) to ease the measurement task.

The problem was further complicated by the fact that the unsteady forces are a direct function of the heaving amplitude. The desire for large unsteady forces for easy measurement was thwarted by the problem that if the model was allowed to perform large oscillations one of two things must happen: 1) the model exhibits a large wetted area change or 2) the model becomes submerged during part of the cycle. This second effect referred to here as part-cycle-

planing causes drastic changes in the unsteady forces as described in Section V.

The tests were performed with a slight amount of deadrise and with the amplitude of oscillation as low as was practical. Cursory examination of the effects of deadrise and oscillation amplitude showed them to be small as long as the part-cycle-planing mode was avoided.

In addition to the experimental investigations with the planing delta wings some theoretical calculations were also performed. These may be found in Section IV. The theory originally developed in reference (30) by M. P. Tulin is re-done correctly here and is also extended to quasi-steady heaving motions. The theoretical flow is compared to the assumed model in Section IV and the calculated results are compared with the experimental measurements in Section V.

II. EXPERIMENTAL APPARATUS

A. Free Surface Water Tunnel

The experimental work on the delta wings oscillating in heave was conducted in the Free Surface Water Tunnel at the California Institute of Technology. Reference (31) describes the tunnel in considerable detail so only its major features will be discussed here. The tunnel is shown in Figure 1. It is closed loop, recirculating and has a useable working section approximately 20 inches by 20 inches in cross section and about eight feet long. The distinguishing feature of the working section is that the upper surface is open to the atmosphere which enables the tunnel to be used for planing and near-surface tests.

The maximum velocity attainable in the working section is about 30 feet per second. This velocity is indicated on a manometer which gives the difference between the total head upstream from the nozzle and the static head in the working section.

A feature of the tunnel which was added after it was built and consequently is not discussed in reference (31) is the skimmer. Its function is to remove the fluid decelerated in the boundary layer on the upper surface of the nozzle. This fluid is added back into the circuit downstream of the working section. The result is that the velocity profile of the flow in the working section is constant near the free surface, allowing meaningful planing tests to be performed. There are of course boundary layers on the bottom and side walls of the working section but these do not ordinarily interfere with the

experiment. Figure 2 presents an overall view of the working section and test equipment.

B. Hydraulic Pump and Oscillator

The model was made to oscillate hydraulically. A Dennison variable displacement pump supplied oil at 1250 psi for these experiments. The pump and oil reservoir are shown in Figure 3. This oil, controlled by a servo valve, causes a double-acting piston to move up and down in a cylinder.

The servo valve and actuating mechanism are shown in Figures 4 and 6. It was designed and built by Team Corporation of El Monte, California. Not pointed out in the figures are the position and velocity transducers which sense the motion of the piston and provide feedback information to the servo controller. The position transducer is a linear variable differential transformer (LVDT) and the velocity transducer is nothing more than a magnetized iron core inside a coil of wire. The voltage generated is proportional to the number of lines of force being cut per unit time and hence the velocity.

C. Servo Controller

The device which took the input signal, compared it with the feedback and generated the signal to the servo valve is called the servo controller. It was designed and built by the McFadden Electronics Company of South Gate, California, and is Model 150A. It was designed to be operated with position, velocity or force feedback. It was run throughout these tests on velocity feedback

because this gave the best response in the frequency range of interest.

D. Models and Attachment Fixtures

The models, shown in Figure 5, are two sharp-edged delta wings with apex angles of 15 and 30 degrees. They were fabricated from one-quarter inch aluminum plate and are both approximately one foot in length. Their bottom sides are both flat and a two-stage bevel, rounded by hand, was used on the top. This produced quite sharp edges. The effect of camber is negligible, particularly in light of the leading edge separation which occurs in all three types of flow (i.e., planing, fully wetted and ventilated).

Provision for running different angles of attack was accomplished through spacers placed between the model and the force balance. This assures a simple rigid system in which the angle can be reset at will. It does not have the flexibility of a continuously variable device, but has proved very workable here.

E. Instrumentation

1. Lift and Pitching Moment Balance

The measurement of the unsteady lift and pitching moment forces was accomplished by a strain gage strut balance. That is, the balance is an extension of the support strut. The placement of the balance is shown in Figure 6. The balance was constructed so that the lift and pitching moment force would be taken out through two longitudinally spaced vertical links. The drag force was taken out by one horizontal link. On each of these primary load-carrying links

was attached a conventional wire strain gage bridge. By summing the forces in the two vertical links the lift is obtained; by differencing them the pitching moment is obtained. It was found in static tests after the balance was constructed that the drag element had an unacceptable amount of lift interaction and consequently this balance was not used for drag measurements but rather a new one was designed. It is described in some detail in the next section.

The lift and pitching moment balance is shown in Figure 7 before the installation of the strain gages. The wires for the bridges pass through a hole in the top of the balance, up through the center of the support strut and piston to a connector at the top of the oscillator. After the installation of the strain gages metal plates were soldered to the sides of the balance for mechanical protection and to provide support for the waterproofing which consisted of thin sheets of latex cemented around the outside of the balance. The balance was slightly pressurized via the hole carrying the wires to prevent water from entering the balance in the event of a leak.

The balance is fairly rigid having no natural frequencies below 200 cps, but a dynamic calibration of both lift and pitching moment was provided at each of the operating frequencies to obviate the effect of a dynamic magnification factor. The calibration is discussed in more detail later.

2. Drag Balance

As was mentioned the existing balance was found to be unacceptable for drag measurements due to the lift interaction. As

dynamic drag measurements are quite scarce a new balance was designed to measure drag only with the hope of isolating all other forces and moments and eliminating all interactions. The final balance showed in extensive static tests that it did just that to the least count of our equipment.

The balance is shown in Figure 8. It consists of two overlapping side plates which are about 0.2 inch thick and very rigid, one of which is attached to the support strut and the other to the model. The side plates are connected to each other in turn by a system of flexures and an instrumented link to measure the drag force. This drag link is shown in Figure 9.

The flexure system consists of four thin metal sheets lying in two vertical transverse planes. Each flexure is 0.8 inch high, 0.005 inch thick and 0.2 inch in the lateral direction. They were cut from sheet stock and furnace brazed in position. They carry all loads except drag for which they are comparatively flexible. The instrumented link carries most of the drag force providing high sensitivity. It is a flat bar approximately 0.3 inch high, 3 inches overall length and 0.050 inch thick except in the central instrumented portion where it is 0.030 inch thick. It is attached at the front to the grounded side and at the back to the model side. This puts the link in tension. Small "cut-outs" were machined into the link at each end just inboard of the attachments to prevent unwanted moments from getting to the instrumented section.

The strain gages are of the solid state type of which two are the P type and two the N type giving high gage factors and four active

gages. Their placement on the gaged section was further planned to cancel any moments which might creep in. Temperature compensation is also provided by gage matching but that is of little importance in this application.

Because the gages could not be in place during the brazing the balance was designed so that the drag link could be inserted through an opening in the trailing edge after brazing and fastened in place by dowel pins and cap screws through access holes in the side pieces. The opening in the trailing edge was filled with a brass plug to provide support for the waterproofing. This has the added advantage of easing maintenance should the gage fail. Waterproofing is provided as on the lift balance by thin latex sheets cemented to the outside of the balance.

The balance was designed so that it is sufficiently rigid in the drag direction (i.e., its natural frequency is above 600 cps with a model attached) so that it could be calibrated statically and the same factor used at all frequencies.

3. Voltage Supplies and Amplifiers

Figure 11 will be helpful in showing how the electronic equipment is patched together. The excitation voltages for the strain gage bridges were provided by a Microdot Power and Balance Unit PB-200A for each. They have provision for patching resistors on a conditioning board to approximately balance the bridge. A potentiometer was also provided for balance which was useful for nulling the steady load. Each unit contained a potentiometer for setting the

excitation voltage. A Microdot Voltage and Balance Monitor VB-300 was used to monitor the excitation voltages and to null the bridge output during steady operation.

The output of the strain gage bridges was fed through a series of Burr-Brown Model 1685 amplifiers. In the lift-pitching moment balance the outputs were summed and differenced in the first two amplifiers to produce lift and pitching moment. These outputs went to a selector switch so that only the signal being analyzed would be fed to two other amplifiers connected in series. The total gain was then 1000.

4. Return Signal Analyzer

The force signals and heaving velocity signals were analyzed in Boonshaft and Fuchs Model 711A Return Signal Analyzer (RSA). The signal being analyzed is compared internally to a signal of the same frequency as the command signal. A Fourier analysis is performed electronically and the components can be read out on meters or on an auxiliary voltmeter.

5. Variable Phase Low Frequency Oscillator

The command signal which was fed to the servo controller was generated by a Boonshaft and Fuchs Model 711AP Variable Phase Low Frequency Oscillator (VPLFO). This has two outputs; one was fed into the servo controller, the other is also tied internally to the RSA. By varying the phase of the command signal while analyzing the output of the velocity transducer a velocity reference for the force signals can be obtained.

6. Digital Voltmeter

The output of the RSA was connected to a Non-linear Systems Series 2900 Digital Voltmeter. This is an integrating meter and the integrating times most frequently used were one and ten seconds, the latter used if the data were unsteady.

7. Position and Velocity Transducers

The position and velocity transducers were mentioned earlier. The primary functions of the position transducer were to aid in the calibration of the velocity transducer and to provide static height stability in the servo controller. The velocity transducer provided the phase reference for the force data and was also used in the normalization of the forces.

F. Support and Ventilation Struts

The support strut tying the model and force balance to the piston of the oscillator is a NACA 0010 section of 10 percent thickness and 4 inch chord. It was designed to minimize ventilation from the free surface. The force balances had similar contours to continue the strut profile to the model. The angle changing spacers were also contoured similarly.

For the ventilation tests a means was needed to provide a known quantity of air at the suction side of the foil without otherwise interfering with the flow. The method finally chosen was a hollow bi-convex strut fabricated from two sheets of aluminum 0.040 inch thick rolled into cylindrical sections which were subsequently heli-

arc welded at the leading and trailing edges. This was slipped over the support strut and attached to it above the balance. A means was provided to seal the upper end and air supply and pressure fittings were provided. The ventilation strut is shown in Figure 10.

G. Ventilation Measuring Apparatus

1. Air Supply Measurement

The air supplied to the cavity during the ventilating runs was measured by a Fischer-Porter flowmeter and the supply pressure was measured on a Heise Bordon tube pressure gage. The reduction of the data is discussed later.

2. Cavity Length Measurement

The cavity length was measured with a tape rule held against the working section side. This method probably is not accurate to less than an inch but considering the difficulty in defining the termination point for the cavity this accuracy was quite acceptable.

3. Cavity Pressure Measurement

The cavity pressure was measured by a water-filled U-tube manometer open to the atmosphere on one end and connected to the top of the ventilation strut on the other. There was a pressure drop from the point of measurement to the cavity which was accounted for by running tests with the tunnel dry. This allowed the pressure drop which is a function of the air supply rate to be subtracted out.

III. EXPERIMENTAL PROCEDURE

A. Calibrations

1. Position Transducer

The position transducer was calibrated using a microscope attached to a lead screw and counter. The lead screw and counter were geared together so that the counter read directly in thousandths of an inch. The microscope could be set with the cross hairs aligned to a mark on the oscillator shaft; a number of position and voltage readings would then be made and the data least squares fit with a cubic polynomial. The linear term is the only one which is used since over the range covered in the velocity transducer calibration only the linear term is important.

2. Velocity Transducer

The velocity transducer was calibrated using the position transducer since the motion was simple harmonic. At each of the frequencies used in the experiment the velocity and position signals were analyzed using the Return Signal Analyzer. Since for simple harmonic motion the velocity amplitude is just the angular frequency times the position amplitude, and since we know the position calibration factor, we can then infer the velocity calibration factor.

3. Lift and Pitching Moment Balance

The lift and pitching moment balance was calibrated both statically and dynamically. Static tests were run to determine the electrical position of each of the force links and the excitation

voltages were chosen so that both of the lift gages (N_1 and N_2) had the same output/unit force. This must be done, otherwise the balance will have a lift-pitching moment interaction.

The dynamic calibrations were done at each frequency because even though the balance's natural frequency was well above those used in the experiment this afforded an easy way to obviate errors due to dynamic response. A two piece calibration mass shown attached to the strut in Figure 10 was fabricated specifically for this task. The upper part, made of aluminum, was bolted to the strut at the model attachment holes. The bottom part, much heavier and fabricated of brass, was made so that it could be attached to the aluminum bar at any of six different positions to vary the longitudinal center of gravity of the total live mass. Using Newton's second law and the characteristics of simple harmonic motion the forces were inferred from knowing the mass and the velocity transducer output. By oscillating the mass at two different longitudinal positions (generally the end ones) the pitching moment calibration coefficients and the longitudinal electrical center were determined. This also allowed a check on the sensitivity of lift to pitching moment changes.

4. Drag Balance

The drag balance presented a much easier calibration problem. Because of its designed-in constant response over the test frequency range the calibration could be and was done statically. This consisted of bolting a fixture to the bottom of the balance and running a line from this fixture over a pulley to a hook on which shot-

bags could be hung. The problem of assuring that the line was pulling in the drag direction was handled by levels on both the fixture and the line. Having only one load-carrying element in the drag direction no matching of outputs was required as in the "lift" balance, therefore the excitation voltage was changed to maintain a fixed calibration coefficient over the period of drag testing.

As a check for whipping of the strut the balance was oscillated with the tunnel dry and no sensible drag output was noted.

5. Return Signal Analyzer

The manner in which the force coefficients were normalized meant that the Return Signal Analyzer processed a signal in the denominator as well as the numerator. This means that an absolute calibration was not required (in fact, it was checked against an rms voltmeter and appeared to be within two percent of scale) but only variations from scale to scale. These relative coefficients were obtained using a signal from the Velocity Phase Low Frequency Oscillator and leap-frogging from scale to scale. Except for the two lowest scales they were within one percent of the ratio of scales so even had they not been accounted for, and they were, the effect would hardly have been noticed.

6. Air Supply Apparatus

The ventilation tests required that three additional pieces of apparatus be calibrated. They are a flow meter, a supply pressure gage and in this case we also had to account for the pressure drop in the ventilation strut.

The flow meter was a Fischer-Porter product with tube No. FP-3/4-27-G-10/80 for which a calibration curve was provided by the manufacturer. It was double-checked against another flow meter which had been previously calibrated and was within the five percent tolerance, over the working range, that these instruments are good for.

The supply pressure, which never exceeded 70 psi at the flow meter, was measured by a Heise gage No. H1665. This gage was checked with a dead weight tester and found to be within 0.1 psi from zero to ninety-five psi. This was the accuracy to which the gage could be read.

The cavity pressure was given by a water manometer less the pressure drop in the ventilation strut. This pressure drop was accounted for by running various air supply rates through the strut with the tunnel dry and calculating the relationship between pressure drop and mass flow rate. This drop was then subtracted from the apparent cavity pressure in the final data reduction.

B. Parameters Investigated

There are basically six parameters whose influence on the force coefficients was investigated. They are angle of attack, aspect ratio, reduced frequency, submergence, oscillation amplitude and air supply rate. Not all combinations of the parameters were run due to the time involved, however representative checks were made where it was felt appropriate.

The basic angles of attack which were investigated varied

depending on the type of flow. For instance, in the fully wetted runs angles of zero, six and twelve degrees were run for each of the submergences. The planing runs, however, were done only at six and twelve degrees since proper planing cannot be established at zero degrees. The ventilated runs were performed at twenty degrees angle of attack because this is near the lowest angle that the model could be fully ventilated under the test conditions.

In addition to the basic data runs, tests were done at minus six and minus twelve degrees with the model fully wetted and at the deepest submergence. This was done to give some justification to the assumptions that the camber and strut effects were small.

Two different models were used. They were both fabricated from 0.250 inch aluminum plate and have sharp edges all around to insure flow separation. Both models were approximately one foot in length and had apex angles of 15 and 30 degrees. The aspect ratio of these two models is 0.526 and 1.071 respectively.

One of the most varied parameters in the tests was the reduced frequency. In all of the runs except the ventilation tests the reduced frequency was the one varied, by means of the frequency, having fixed the other variables. In addition to the fundamental influence of the reduced frequency on the force coefficients, various tunnel velocities were run to determine the effect of obtaining the reduced frequency by different frequency-velocity combinations. This was done only at an angle of attack of twelve degrees, 30° model and at maximum submergence since this was thought to provide the severest test.

The effect of the free surface was investigated in the fully wetted tests by running the models at approximately two, six and ten inches submergence. These large submergence changes were accomplished by inserting spacers between the box holding the hydraulic oscillator and the tunnel.

For the data reduction it was desirable to normalize the force coefficients with the heaving velocity but to do this it was necessary to establish that the effect on these coefficients of changing the amplitude was negligible. Since it was impractical to do this at every combination of parameters the case of the 30° delta wing, 12° angle of attack, 0.83 chord submergence and 16.5 ft/sec tunnel velocity was chosen as at least representative if not a worst case. In the planing runs the oscillation amplitude was more constrained by other things to small values, consequently the effect was that it was not practical to measure but was thought to be very slight.

In the ventilation runs a whole new group of parameters was introduced. They are the air supply rate, the cavity length and the cavity pressure. These parameters are all directly related to each other so the situation is not quite as complicated as it sounds. The basic variable chosen was the air supply rate but the other data were also computed.

C. Data Runs

In this section we will be concerned with the actual steps of data gathering. For the most part the steps are the same for both fully wetted and planing tests. The basic parameter varied for these

two in any particular run was the frequency whereas in the ventilation runs the air supply rate was varied.

Before the start of a run we must select and fix the following "variables":

1. Model
2. Angle of attack
3. Submergence
4. Oscillation amplitude (fully wetted)
5. Tunnel velocity

At some time during the testing each combination of model and attachment fixtures must have its mass determined because the force due to the "live" mass and the acceleration must be accounted for to determine the fluid mechanical forces. This was accomplished by assembling the model and fixtures as for a test and then with the tunnel dry the model would be oscillated and the live mass tare determined.

Having fixed the above parameters and with the tunnel full and operating at the chosen velocity but with the model stationary, the bridge excitation voltages are checked and the bridges balanced to limit the DC input to the RSA. With the static bridge outputs zeroed the amplifiers are balanced. Now the model can be oscillated.

The frequency is chosen on the VPLFO and the voltage for the desired oscillation amplitude is dialed in. With the input shorted each output channel of the RSA is zeroed to limit the tare. Now the signal from the velocity transducer on the oscillator is applied at the input of the RSA and the phase of the command signal varied so that the RSA output appears only on one channel. By varying the phase in

this way a velocity reference is obtained. The force is applied to the RSA. That part of the force signal observed on the channel previously containing the velocity has the same phase as the velocity. The second output channel gives the quadrature component of force.

In a typical data block zeros are taken for each channel with the input shorted. The heaving velocity is applied to the RSA and read. The force signal is applied and each channel read. The input is again shorted and zeros again taken. When using the "lift" balance, the first force taken is the lift. After the second set of zeros another velocity is taken and then the pitching moment. This routine is repeated again at constant frequency so that redundant lift and pitching moment readings are obtained with sets of zeros before and after each force reading. The data taking is similar for the drag balance except that only one force is being read. This process is repeated at each of the frequencies investigated.

The ventilation runs are similar in that the bridges and amplifiers are balanced with the model stationary and the RSA outputs are zeroed with shorted input. The primary difference lies in that the frequency is fixed not just for a "block" of data but for an entire "run". The parameter varied within the run is the air supply rate.

D. Data Reduction

The data reduction was accomplished for the most part with the aid of an electronic digital computer. The repetition makes the job boring which encourages errors when done by hand. The computer is ideal for this type of work. The data were reduced on the Institute's

IBM 7094 computer which is something like killing flies with a steam shovel but it was the only one of convenient accessibility.

The calibrations and data reduction are intimately tied together, consequently some overlap with the previous section on calibrations must be expected. The equations defining the calibration coefficients and their use in the data reduction are presented here.

1. Force Coefficients

We will assume that the hydrofoil is performing a simple harmonic heaving motion. The vertical displacement transducer output is then given by a relation of the form

$$y = F_1 A' \sin \omega t \tag{1}$$

where y is the vertical displacement transducer output, F_1 the displacement calibration coefficient obtained as described previously and A' is the amplitude. Feeding this displacement signal into the RSA we get (all RSA output signals will be denoted by tildes)

$$\tilde{y} = C A' F_1 \tag{2}$$

where C is some constant associated with the Fourier analysis performed by the RSA.

Because the motion is simple harmonic the velocity transducer output can be written in the form

$$\dot{y} = F_2 A' \omega \cos \omega t \, . \tag{3}$$

This can also be thought of as the defining relation for the velocity

calibration factor, F_2. The signal becomes, after processing by the RSA,

$$\tilde{\dot{y}} = F_2 C A' \omega \tag{4}$$

or substituting equation (2) into equation (4) we get

$$\tilde{\dot{y}} = F_2 \frac{\tilde{y}}{F_1} \omega \ . \tag{5}$$

Solving equation (5) for F_2 shows us explicitly how we may obtain this calibration factor.

$$F_2 = \frac{F_1}{\omega} \frac{\tilde{\dot{y}}}{\tilde{y}} \tag{6}$$

The acceleration is also directly related to the velocity and since we know the value of the calibration mass we can use Newton's Second Law to infer the force output.

$$F = - m F_3 A' \omega^2 \sin \omega t \tag{7}$$

This equation defines the lift force calibration factor F_3 and m is the calibration mass (total). The signal as processed by the RSA is

$$\tilde{F} = - m F_3 C A' \omega^2 \ . \tag{8}$$

Substituting equation (4) into equation (8) the RSA output becomes

$$\tilde{F} = - m F_3 \omega \frac{\tilde{\dot{y}}}{F_2} \tag{9}$$

and solving this expression for F_3 we get equation (10).

$$F_3 = - \frac{F_2}{m\omega} \frac{\tilde{F}}{\tilde{\dot{y}}} \tag{10}$$

The rms dynamic lift is then related to the RSA output signal through the factor F_3.

$$\tilde{L}_{r,i} = L_{r,i} \cdot F_5 \tag{11}$$

The subscripts r and i have been used to denote the force components in-phase with the apparent change of angle of attack and 90^o out of phase.

The apparent change of angle of attack is given by

$$\bar{\alpha} = \frac{-\tilde{\dot{y}}}{U F_2} \cdot \tag{12}$$

The in-phase lift coefficient is then defined by and calculated using equation (13).

$$C_{L_{\bar{\alpha}_r}} = \frac{L_r}{\frac{1}{2}\rho U^2 A \bar{\alpha}} = \frac{2 F_2}{\rho U A F_3} \frac{\tilde{L}_r}{\tilde{\dot{y}}} \tag{13}$$

The quadrature lift coefficient is then defined by and calculated using equation (14).

$$C_{L_{\bar{\alpha}_i}} = \frac{L_i}{\frac{1}{2}\rho U A \bar{\alpha}} = \frac{2 F_2}{\rho U A F_3} \left(\frac{\tilde{L}_i}{\tilde{\dot{y}}} - \frac{m' F_3 \omega}{F_2} \right) \tag{14}$$

The second term in parentheses in equation (14) represents the force due to the acceleration of the model's mass and the live mass of the balance. The total live mass is m' .

The pitching moment calibration is similar. The calibration mass m has its center of gravity at a distance ℓ from the electrical center of the balance. This offset causes a moment as the mass is accelerated vertically. The moment signal can be expressed in the form

$$M = m \ell F_4 A' \omega^2 \sin \omega t \ . \tag{15}$$

This equation defines the pitching moment calibration factor F_4 and the processed signal can be expressed as

$$\tilde{M} = m \ell F_4 C A' \omega^2 \ . \tag{16}$$

Substituting equation (4) into equation (16) and solving for the calibration factor F_4 we get

$$F_4 = \frac{F_2}{m \ell \omega} \frac{\tilde{M}}{\tilde{\dot{y}}} \ . \tag{17}$$

The rms dynamic pitching moment is related to the RSA output signal through the factor F_4 .

$$\tilde{M}_{r,i} = M_{r,i} \cdot F_4 \tag{18}$$

The in-phase pitching moment coefficient is then defined by and calculated using equation (19).

$$C_{M_{\bar{\alpha}_r}} \qquad \frac{M_r}{\frac{1}{2}\rho U^2 A c \bar{\alpha}} = \frac{2 F_2}{\rho U A F_4 c} \quad \frac{\tilde{M}_r}{\tilde{\dot{y}}} \tag{19}$$

The quadrature pitching moment coefficient is defined by and calculated using equation (20).

$$C_{M_{\bar{\alpha}_i}} = \frac{M_i}{\frac{1}{2}\rho U^2 A c \bar{\alpha}} = \frac{2F_2}{\rho U A F_4 c} \left(\frac{\tilde{M}_i}{\tilde{\dot{y}}} - \frac{m' \ell' F_4 \omega}{F_2} \right) \tag{20}$$

The distance of the total live mass from the electrical center of the balance is ℓ' and m' is as for the lift. The pitching moments as given above are for moments about the electrical center of the balance. To obtain moments about a parallel axis through the model planform's centroid we must have drag data.

The drag is reduced in much the same way. The drag calibration factor is obtained statically and is the same for all frequencies. Also, because the motion is perpendicular to the direction that the force is being measured there is no live mass tare. The drag force is related to the RSA output by

$$\tilde{D}_{r,i} = D_{r,i} \cdot F_5 \tag{21}$$

and the drag coefficients are given by

$$C_{D_{\bar{\alpha}_{r,i}}} = \frac{D_{r,i}}{\frac{1}{2}\rho U^2 A \bar{\alpha}} = \frac{2 F_2}{\rho U A F_5} \quad \frac{\tilde{D}_{r,i}}{\tilde{\dot{y}}} \quad . \tag{22}$$

2. Ventilation Parameters

The additional data taken during the ventilation runs were reduced to dimensionless parameters as follows.

The cavity length was measured with an ordinary rule and the number divided by the model chord length to produce a dimensionless cavity length.

The air supply rate was measured with a Fischer-Porter flow meter and the supply rate reduced to standard cubic feet per second using calibration information provided by the manufacturer. An air supply coefficient was defined as

$$C_Q = \frac{Q}{U A \sin \alpha} \quad .$$

This has the meaning of a column of air of cross-sectional area equal to the projected frontal area of the foil and moving at free stream velocity.

The ventilation number is analogous to the cavitation number and is defined by

$$\sigma_v = \frac{p_\infty - p_c}{\frac{1}{2} \rho U^2} \quad .$$

The cavity pressure was measured by a manometer connected to the ventilation strut. The pressure drop in the strut was calibrated as a function of the air flow rate so that the cavity pressure reading could be adjusted accordingly.

IV. A THEORY OF UNSTEADY PLANING OF SLENDER BODIES AT SMALL ANGLES OF ATTACK

A. Preliminary Remarks

We digress somewhat here to develop some theoretical results so that they can be referenced in the course of discussing the experimental data. As was mentioned in Section I Tulin (30) has previously presented a theory for steady planing of slender bodies at small angles of attack. It is unfortunate that the paper containing Tulin's efforts has quite a few errors. Some of these are algebraic; others are perhaps conceptual. The paper nevertheless contains an interesting approach to the problem and the method used is basically correct.

The purpose of this section is two-fold. It is intended that Tulin's original problem be corrected. It is also intended that the problem be extended to unsteady planing and it is shown how the unsteadiness affects the validity of the approach. The specific cases of uncambered delta wings at rest and oscillating in heave are treated in detail.

B. The Coordinate System and Bernoulli Equation

The coordinate system used for the solution of this problem is shown in Figure 12. It is fixed to the foil with its origin at the foil's apex. The x-axis passes through the mid-point of the trailing edge. The y-axis is normal to the plane containing the apex and the trailing edge and the z-axis completes the right handed set. The foil

may have a small amount of camber but is assumed to be unyawed.

Neglecting the effect of gravity the equation of motion of the fluid in this frame of reference is given by:

$$\frac{D\vec{q}}{Dt} + \dot{\vec{v}}_b = -\frac{1}{\rho}\nabla p \tag{23}$$

The term $\dot{\vec{v}}_b$, not usually encountered in steady problems, is required because Newton's Second Law must be applied in an inertial reference frame. This term represents the acceleration of the previously defined coordinate system with respect to an inertial one.

The velocity of any fluid particle with respect to the coordinate system of Figure 12 is $\vec{q}$. This velocity is expressed in terms of a potential such that the gradient of the potential yields the velocity.

$$\nabla\Phi = \vec{q} \tag{24}$$

Using this definition of Φ we can re-write equation (23).

$$\nabla\left[\Phi_t + \frac{1}{2}(\nabla\Phi)^2 + \frac{p}{\rho} + \dot{v}_b\,(y\cos\alpha - x\sin\alpha)\right] = 0 \tag{25}$$

It should be noted that in the above equation motions normal to the free stream have been assumed. We can integrate equation (25) to get

$$\Phi_t + \frac{1}{2}(\nabla\Phi)^2 + \frac{p}{\rho} + \dot{v}_b\,(y\cos\alpha - x\sin\alpha) = B(t)\ . \tag{26}$$

The function $B(t)$ is often called the Bernoulli constant since in steady problems it is a constant. Here it may be a function of time.

At infinity the velocity potential Φ is given by

$$\Phi_\infty = (U\cos\alpha + v_b \sin\alpha)x + (U\sin\alpha - v_b\cos\alpha)y \qquad (27)$$

From this condition on the potential at infinity we get upon substitution into equation (26) the value of $B(t)$.

$$B(t) = \frac{p_\infty}{\rho} + \frac{1}{2}(U\cos\alpha + v_b\sin\alpha)^2 + \frac{1}{2}(U\sin\alpha - v_b\cos\alpha)^2 \qquad (28)$$

By subtracting the potential at infinity we can define a new "perturbation" potential as in equation (29).

$$\varphi = \Phi - \Phi_\infty \qquad (29)$$

Re-writing equation (26) in terms of the new potential φ we get the exact unsteady Bernoulli equation for this problem.

$$\varphi_t + \frac{1}{2}(\varphi_x + U\cos\alpha + v_b\sin\alpha)^2 + \frac{1}{2}(\varphi_y + U\sin\alpha - v_b\cos\alpha)^2$$

$$+ \frac{1}{2}(\varphi_z)^2 + \frac{p}{\rho} = \frac{1}{2}(U\cos\alpha + v_b\sin\alpha)^2$$

$$+ \frac{1}{2}(U\sin\alpha - v_b\cos\alpha)^2 + \frac{p_\infty}{\rho} \qquad (30)$$

C. Laplace's Equation and The Boundary Conditions

Although it has not been stated we are taking the fluid to be incompressible and inviscid. The condition of incompressibility simplifies the continuity equation and the irrotationality following from the inviscid assumption allows us to write the velocity as the gradient of a scalar potential. The equation then that the velocity potential must satisfy is the well known Laplace's equation (31).

$$\nabla^2 \Phi(x,\ y,\ z;\ t) \ =\ 0 \tag{31}$$

It is easily shown that the perturbation potential also satisfies the same equation.

The boundary conditions on the perturbation potential will now be constructed. From its definition the perturbation potential is seen to vanish at infinity. On the foil we have the condition that the flow must be tangent to the boundary, which gives:

$$\Phi_y \ / \ \Phi_x \ = \ y_o' \tag{32}$$

where $y_o(x)$ is the camber function and the prime denotes differentiation with respect to its spatial argument. Equation (32) can be re-written as shown below.

$$\begin{aligned} \Phi_y \ &= \ \Phi_x \, y_o' \\ &= \ (\ \varphi_x \ + \ U \cos\alpha \ + \ v_b \sin\alpha \ ) \, y_o' \end{aligned} \tag{33}$$

This boundary condition on the foil is exact. The boundary conditions on the free surface require some approximations. They will be discussed in the next section.

D. Approximations

From this point on we will assume that we are treating a "slender" body. What we mean by slender will become clear as the approximations are made. If we can assume as a result of this slenderness that $\varphi_{xx} \ll \varphi_{yy}, \varphi_{zz}$, it can then be neglected in Laplace's equation and x becomes a parameter entering the problem only through the boundary conditions and the potential is not affected by conditions upstream. Laplace's equation can now be written as

$$\nabla^2 \varphi(y, z; x, t) = 0 . \tag{34}$$

The problem has been reduced to a two dimensional boundary value problem in the so-called "cross-flow" plane.

We can also simplify the boundary condition on the foil under the assumptions:

1) $\alpha << 1$ so that $\sin\alpha \doteq \alpha$ and $\cos\alpha \doteq 1$

2) $\varphi_x << U$ and 3) $\alpha v_b << U$.

Equation (33) then becomes

$$\Phi_y \doteq \varphi_y + U\alpha - v_b \doteq U y_o'$$

or we can re-write this as

$$\varphi_y \doteq v_b + U y_o' - U\alpha . \tag{35}$$

We have still to satisfy boundary conditions on the free surface. The nature of the problem dictates that we should have free stream pressure everywhere on the free surface. The position of the free surface, not known a priori, will be taken to lie along the z-axis. In the actual case, sketched in Figure 15, the free surface boundary is at $y = \alpha x$ at infinite distances from the foil and acquires a complicated shape near the foil. The approximation that the boundary conditions can be applied to the z-axis is necessary to keep the problem tractable. Figure 14 presents a photograph of a 30^{o} apex angle delta wing planing at a small angle of attack. The spray can be seen. Because of the difficulty of determining the shape of the spray and the flow in the spray region, the spray will be represented as a singularity. The separation of the tips of the spray depends on the static height of the apex above the free surface, a slight amount of which will exist in any real situation.

As is shown in Figure 13 the spray singularity is taken at $z = b_1$ (i.e., $\xi = b$). Outside of this point the flow is assumed to be undisturbed or rather that $\varphi_z = 0$ for $|z| > b_1$ and since $\varphi = 0$ at infinity, $\varphi = 0$ for $|z| > b_1$ also.

In the region between the leading edge, $z = a(x)$ and $z = b_1$ we must determine a velocity boundary condition which at least approximates the pressure condition. This will be our next concern.

Let us define a new velocity potential in terms of coordinates normalized on the local semi-span, $a(x)$, since the flow will be approximately conical.

$$\varphi(y,\ z;\ x,\ t) = a(x)\, f(\eta, \xi\ ;\ t) \tag{36}$$

The coordinates are given by:

$$\eta = \frac{y}{a} \quad \text{and} \quad \xi = \frac{z}{a} \ . \tag{37}$$

The derivatives of φ expressed in terms of f and appropriate coordinates are given below.

$$\begin{aligned} \varphi_x &= a_x (f - \eta f_\eta - \xi f_\xi) \\ \varphi_y &= f_\eta \\ \varphi_z &= f_\xi \\ \varphi_t &= a(x)\, f_t \end{aligned} \tag{38}$$

On the foil and in the region near the leading edge the pressure equation becomes

$$\begin{aligned} \frac{p - p_\infty}{\rho} \doteq & - U\varphi_x - \frac{1}{2}(U y_o')^2 - \frac{1}{2}(\varphi_z)^2 \\ & + \frac{1}{2}(U\alpha - v_b)^2 - \varphi_t \end{aligned} \tag{39}$$

where the $(\varphi_x)^2$ term has been neglected along with the assumptions following from the smallness of α. Replacing derivatives of φ by the appropriate functions of f and setting $p = p_\infty$ we get that at the free surface near the leading edge the following relation holds.

$$- 2U a_x (f - \xi f_\xi) - (U y_o')^2 - (f_\xi)^2$$

$$+ (U\alpha - v_b)^2 - 2a(x) f_t = 0 \qquad (40)$$

We will now estimate the value of each term in this equation so that some of them can be dispensed with. Near the leading edge $\xi \doteq 1$. Taking the distance from the leading edge to b to be ϵ and assuming f_ξ is approximately constant in that region we get that $f(1) \doteq - \epsilon f_\xi(1)$ near the leading edge. Taking $U a_x \sim \mathcal{O}(1)$, $U y_o' \sim \mathcal{O}(\delta)$, $U\alpha \sim \mathcal{O}(\delta)$ and $v_b \sim \mathcal{O}(\delta)$ where $\delta << 1$ we re-write equation (40) where the order of each term is noted.

$$\begin{matrix} & 1 + \delta^2 & & \delta^2 & & 1 \\ 0 = & 2U a_x (1 + \epsilon) f_\xi & - & (U y_o')^2 & - & (f_\xi)^2 \end{matrix}$$

$$\begin{matrix} & \delta^2 & & k\delta^2 \\ + & (U\alpha - v_b)^2 & + & 2a(x) f_t \end{matrix} \qquad (41)$$

The reduced frequency has been denoted by k. The order of the last term in the above equation has not been shown yet. It will be shown later when ϵ is calculated. Since we will seek a quasi-steady solution of this problem we can reasonably neglect this term until a time when the proper restrictions on its importance can be shown. Keeping only terms of $\mathcal{O}(1)$ equation (41) yields the following condition.

$$f_\xi = 2U a_x \, \mathrm{Sgn}(\xi) \quad \text{for} \quad 1 \leq |\xi| < b \qquad (42)$$

Conditions on f have now been specified along the entire ξ-axis. They are shown on Figure 13.

E. The Solution of the Boundary Value Problem

The boundary value problem is seen to be, except for the unsteady parts, identical with Tulin's. The method of solution proposed by him and indeed part of his solution are used more or less directly. It is intended that the confusion in his paper has been removed in this solution.

The specified boundary conditions may be satisfied by a distribution of vorticity of strength $\gamma(\xi, t)$ along the ξ-axis between $-b(x, t)$ and $+b(x, t)$.

$$f_\eta(\xi) = \frac{1}{2\pi} \int_{-b}^{+b} \frac{\gamma(\zeta, t)}{(\xi - \zeta)} \, d\zeta \tag{43}$$

We can also re-write equation (43) below since $\gamma(\xi, t) = 2f_\xi(-0, \xi; t)$.

$$\pi f_\eta(\xi) = \int_{-b}^{-1} \frac{f_\xi(\zeta)}{(\xi - \zeta)} \, d\zeta + \int_{-1}^{1} \frac{f_\xi(\zeta)}{(\xi - \zeta)} \, d\zeta$$

$$+ \int_{1}^{b} \frac{f_\xi(\zeta)}{(\xi - \zeta)} \, d\zeta \tag{44}$$

We can apply the known conditions on f_η and f_ξ, namely

$$f_\eta(\xi) = v_b + Uy_o' - U\alpha = \nu \quad \text{for} \quad |\xi| \leq 1$$

$$f_\xi(\xi) = 2Ua_x \,\mathrm{Sgn}(\xi) \qquad \text{for } 1 < |\xi| < b .$$

Equation (44) then becomes the following where the only unknown is f_ξ for $|\xi| < 1$.

$$\pi\nu = -2Ua_x \int_{-b}^{-1} \frac{d\zeta}{(\xi - \zeta)} + 2Ua_x \int_{1}^{b} \frac{d\zeta}{(\xi - \zeta)}$$

$$+ \int_{-1}^{1} \frac{f_\xi(\zeta)}{(\xi - \zeta)}\, d\zeta \qquad (45)$$

Re-writing this in the form of the conventional airfoil equation we have the following:

$$\int_{-1}^{1} \frac{f_\xi(\zeta)}{(\xi - \zeta)}\, d\zeta =$$

$$\left[\pi\nu - 2Ua_x \int_{1}^{b} \frac{d\zeta}{(\xi - \zeta)} + 2Ua_x \int_{-b}^{-1} \frac{d\zeta}{(\xi - \zeta)}\right]$$

$$\text{for } |\xi| < 1$$

The formal solution of this equation can be found in Tricomi (32) and is taken from Tulin's work in the form given below.

$$\frac{f_\xi(\xi)}{U} = -\frac{1}{\pi^2\sqrt{1-\xi^2}}\left\{\int_{-1}^{1}\frac{\sqrt{1-\zeta^2}}{(\xi-\zeta)}\left[\pi\frac{\nu}{U}\right.\right.$$

$$\left.\left. - 2a_x\int_{1}^{b}\frac{d\tau}{(\zeta-\tau)} + 2a_x\int_{-1}^{-b}\frac{d\tau}{(\zeta-\tau)}\right]d\zeta\right\} \qquad (46)$$

The vortex sheet limit b is determined later to make $f_\xi(1)$ bounded.

If we combine integrations equation (46) becomes

$$\frac{f_\xi(\xi)}{U} = -\frac{1}{\pi^2\sqrt{1-\xi^2}}\left\{\pi^2\frac{\nu}{U}\xi - 2a_x\int_{1}^{b}d\tau\int_{-1}^{1}\frac{\sqrt{1-\zeta^2}}{(\xi-\zeta)(\zeta-\tau)}d\zeta\right.$$

$$\left. + 2a_x\int_{-b}^{-1}d\tau\int_{-1}^{1}\frac{\sqrt{1-\zeta^2}}{(\xi-\zeta)(\zeta-\tau)}d\zeta\right\}. \qquad (47)$$

Using the following identities:

$$\frac{1}{(\xi-\zeta)(\zeta-\tau)} = \frac{1}{(\xi-\tau)}\left[\frac{1}{(\xi-\zeta)} + \frac{1}{(\zeta-\tau)}\right]$$

$$\int_{-1}^{1}\frac{\sqrt{1-\zeta^2}}{(\xi-\zeta)}d\zeta = \pi\xi \qquad \text{for} \quad |\xi| < 1$$

$$\int_{-1}^{1}\frac{\sqrt{1-\zeta^2}}{(\xi-\tau)}d\zeta = \begin{cases}\pi\left(-\tau-\sqrt{\tau^2-1}\right) & \tau < -1\\ \pi\left(-\tau+\sqrt{\tau^2-1}\right) & \tau > 1\end{cases}$$

the following equations can be shown to be true:

$$\frac{f_\xi(\xi)}{U} = -\frac{1}{\pi^2\sqrt{1-\xi^2}}\left\{\pi^2\frac{\nu}{U}\xi - \pi 2a_x\int_1^b \frac{\left[\xi-\tau+\sqrt{\tau^2-1}\right]}{(\xi-\tau)}\,d\tau\right.$$

$$\left. + \pi 2a_x\int_{-b}^{-1}\frac{\left[\xi-\tau-\sqrt{\tau^2-1}\right]}{(\xi-\tau)}\,d\tau\right\} \qquad (48)$$

$$\frac{f_\xi(\xi)}{U} = -\frac{1}{\sqrt{1-\xi^2}}\left\{\frac{\nu}{U}\xi + \frac{4}{\pi}a_x\xi\int_1^b\frac{\sqrt{\tau^2-1}}{(\tau^2-\xi^2)}\,d\tau\right\} \qquad (49)$$

With the substitution $\sqrt{1-\xi^2}\tan\theta = \sqrt{\tau^2-1}$ it can be shown for $b^2 \doteq 1$ (i.e., $\epsilon << 1$) that the integral in equation (49) can be evaluated approximately.

$$\frac{f_\xi(\xi)}{U} \doteq -\frac{1}{\sqrt{1-\xi^2}}\left\{\frac{\nu}{U}\xi + \frac{4}{\pi}a_x\xi\left(\sqrt{b^2-1}\right.\right.$$

$$\left.\left. - \sqrt{1-\xi^2}\,\tan^{-1}\sqrt{\frac{b^2-1}{1-\xi^2}}\right)\right\} \qquad |\xi| < 1 \qquad (50)$$

To keep $f_\xi(1)$ bounded b must have a particular value; namely,

$$\frac{\nu}{U} + \frac{4}{\pi}a_x\sqrt{b^2-1} = 0 \qquad (51)$$

If we write b as $1 + \epsilon$ and take $\epsilon << 1$ we get the following relation for ϵ .

$$\epsilon = \frac{\pi^2}{32} \left(\frac{\nu}{U a_x} \right)^2 \tag{52}$$

$$= \frac{\pi^2}{32} \left(\frac{v_b + U y_o' - U\alpha}{U a_x} \right)^2 \tag{53}$$

Previously we have assumed that $Ua_x \sim \mathcal{O}(1)$, $v_b \sim \mathcal{O}(\delta)$, $Uy_o' \sim \mathcal{O}(\delta)$ and $U\alpha \sim \mathcal{O}(\delta)$ where $\delta << 1$. From equation (53) then we get directly that $\epsilon \sim \mathcal{O}(\delta^2)$ which certainly justifies taking $b \doteq 1$ for the solution of equation (49) and it also justifies neglecting ϵ compared to 1 in the first term of equation (41).

It was stated without proof in equation (41) that the last term of the equation was $\mathcal{O}(k\delta^2)$. This will now be shown. The term is given below. It has been assumed f_ξ is constant in the region $1 < |\xi| < b$ thereby neglecting any waves, therefore:

$$-2a(x)\, f_t = 2a(x)\, f_\xi \dot{\epsilon} \tag{54}$$

We can evaluate $\dot{\epsilon}$ from equation (53).

$$\dot{\epsilon} = \frac{\pi^2}{16} \frac{(v_b + U y_o' - U\alpha)}{(U a_x)^2} \dot{v}_b$$

Assuming simple harmonic motion for v_b we get $|\dot{v}_b| = \omega |v_b|$ and $a(x)$ is limited to $c\, a_x$ where c is the root chord of the foil.

Substituting this into equation (54) we get the following estimate for the order of that term.

$$-2a(x)\, f_t \sim 2(ca_x)(2Ua_x)\frac{\pi^2}{16}\frac{(v_b + Uy_o' - U\alpha)}{(Ua_x)^2}\,\omega v_b$$

$$\sim \mathcal{O}(k\delta^2) \tag{55}$$

We may conclude then that for $k \sim \mathcal{O}(1)$ we are certainly justified in neglecting the contribution of this term to the boundary condition.

Substituting in the required value of b we get the final solution for f_ξ .

$$\frac{f_\xi(\xi)}{U} = \frac{4}{\pi} a_x \xi \tan^{-1}\frac{\left[-\frac{\pi}{4}\frac{\nu}{Ua_x}\right]}{\sqrt{1-\xi^2}} \quad \text{for } |\xi| < 1 \tag{56}$$

We can also express this in unreduced coordinates.

$$\frac{\varphi_z}{U} = \frac{4}{\pi} a_x \frac{z}{a} \tan^{-1}\frac{\left[-\frac{\pi}{4}\frac{\nu}{Ua_x}\right]}{\sqrt{1-(z/a)^2}} \quad \text{for } |z| < a \tag{57}$$

This is the solution for φ_z as given by Tulin.

F. The Calculation of Forces

The normal force on each incremental section will be found by integrating the pressure across the span.

$$\frac{dN}{dx} = \int_{-a}^{a} \left[p\,(0,\ z;\ x,\ t) - p_{\infty} \right] dz \qquad (58)$$

Using equation (39) this can be re-written as shown below.

$$\frac{dN}{dx} = -\rho \int_{-a}^{a} \left[U\varphi_x + \frac{1}{2}(\varphi_z)^2 + \varphi_t + \frac{1}{2}(U y_o')^2 \right.$$

$$\left. - \frac{1}{2}(U\alpha - v_b)^2 \right] dz \qquad (59)$$

The first term of the above integral is evaluated using the relation:

$$\varphi\,(0,\ z;\ x,\ t) = \int_{a(1+\epsilon)}^{z} \frac{\partial}{\partial \zeta}\ \varphi(0,\ \zeta;\ x,\ t)\, d\zeta$$

$$= -2\,a\epsilon U a_x + \int_{a}^{z} \varphi_{\zeta}\,(0,\ \zeta;\ x,\ t)\, d\zeta\ . \qquad (60)$$

And by an application of Leibnitz' rule we get

$$\int_{-a}^{a} \varphi_x\,(0,\ z;\ x,\ t)\, dz = \frac{\partial}{\partial x} \int_{-a}^{a} \varphi(0,\ z;\ x,\ t)\, dz$$

$$+ 4\,a\,\epsilon U a_x^{\,2}\ . \qquad (61)$$

To use this we will need to integrate φ over the span.

$$\int_{-a}^{a} \varphi(0,\ z;\ x,\ t)\, dz \ = \ -4a^2 \epsilon U a_x \ - \ 2 \int_0^a dz \int_z^a \varphi_\zeta(0,\ \zeta;\ x,\ t)\, d\zeta$$

$$= \ - \ 4a^2 \epsilon U a_x \ - \ 2 \int_0^a \varphi_z(0,\ z;\ x,\ t)\, dz \int_0^z d\zeta$$

$$= \ - \ 4a^2 \epsilon U a_x \ - \ 2 \int_0^a z\ \varphi_z(0,\ z;\ x,\ t)\, dz \qquad (62)$$

Now substituting equation (62) into equation (61) we get

$$- \rho \int_{-a}^{a} U \varphi_x dz \ = \ - \rho\ U \left\{ \frac{\partial}{\partial x} \left[- 4a^2 \epsilon U a_x \right.\right.$$

$$\left.\left. - \ 2 \int_0^a z\, \varphi_z(0,\ z;\ x,\ t)\, dz \right] \ + \ 4a \epsilon U a_x^{\,2} \right\}$$

$$= \ \rho U^2 4a \frac{\partial}{\partial x} (a \epsilon a_x) \ + \ 2 \rho U \frac{\partial}{\partial x} \int_0^a z\, \varphi_z(0,\ z;\ x,\ t)\, dz$$

(63)

The remaining integral can be evaluated by reduction to known form. The solution given in reference (30) is repeated here.

$$\int_0^a z\,\varphi_z\,(0,\ z;\ x,\ t)\,dz \;=\; \frac{4U}{\pi}\,\frac{a_x}{a}\int_0^a z^2 \tan^{-1}\frac{\left[-\frac{\pi}{4}\,\frac{\nu}{Ua_x}\right]}{\sqrt{1-(z/a)^2}}\,dz \qquad (64)$$

Let us substitute $k = k(x,\ t) = -\frac{\pi}{4}\,\frac{\nu}{Ua_x}$ and $\tau = \frac{z}{a}$. Equation (64) is then equal to

$$= \frac{4U}{\pi}\,a^2 a_x \int_0^1 \tau^2 \tan^{-1}\frac{k}{\sqrt{1-\tau^2}}\,d\tau\ . \qquad (65)$$

The integral from zero to one is then solved where the last step is from reference (33), p. 246.

$$\int_0^1 \tau^2 \tan^{-1}\frac{k}{\sqrt{1-\tau^2}}\,d\tau \;=\; \int_0^k dk \int_0^1 \frac{\tau^2\sqrt{1-\tau^2}}{\left[(1+k^2)-\tau^2\right]}\,d\tau \qquad (66)$$

$$= \frac{1}{2}\int_0^k dk \int_{-1/2}^{1/2} \frac{\sqrt{(\tau+1/2)(\tau-1/2)}}{\left[(1/2+k^2)-\tau\right]}\,d\tau$$

$$= \frac{\pi}{2}\int_0^k \left[\frac{1}{2} + \frac{k^2}{2} - k\sqrt{1+k^2}\right] dk \qquad (67)$$

This can be easily integrated to give the following approximation.

$$\int_0^1 \tau^2 \tan^{-1}\frac{k}{\sqrt{1-\tau^2}}\,d\tau \;=\; \frac{\pi}{4}\,(k-k^2) + \mathcal{O}(k^3) \qquad (68)$$

Then to $\mathcal{O}(k^2)$ we have

$$\int_0^a z\,\varphi_z(0,\ z;\ x,\ t)\,dz = -\left(\frac{\pi}{4}\,\nu a^2 + \frac{\pi^2}{16}\,\frac{\nu^2 a^2}{U a_x}\right) . \tag{69}$$

Gathering terms equation (63) becomes finally

$$-\rho \int_{-a}^{a} U\varphi_x\,dz = \rho U^2 4a \frac{\partial}{\partial x}\,(a\epsilon a_x)$$

$$- 2\rho U^2 \frac{\partial}{\partial x}\left(\frac{\pi}{4}\,\frac{a^2\nu}{U} + \frac{\pi^2}{16}\,\frac{\nu^2 a^2}{U^2 a_x}\right)$$

$$= -\frac{\pi}{2}\,\rho U \frac{\partial}{\partial x}\,(a^2\nu) - \frac{\pi^2}{8}\,\rho a \nu^2 \tag{70}$$

The next term in equation (59) is evaluated approximately. Now,

$$\int_0^a \varphi_z^2\,dz = \left(\frac{4U a_x}{\pi}\right)^2 \int_0^a \left(\frac{z}{a}\right)^2 \left[\tan^{-1}\frac{\left(-\frac{\pi}{4}\,\frac{\nu}{U a_x}\right)}{\sqrt{1-\left(\frac{z}{a}\right)^2}}\right]^2 dz \tag{71}$$

If we again let $k = -\frac{\pi}{4}\,\frac{\nu}{U a_x}$ and let $p = \sqrt{1-(z/a)^2}$, equation (71) becomes

$$= \left(\frac{4U a_x}{\pi}\right)^2 a \int_0^1 p\sqrt{1-p^2}\left[\tan^{-1}\frac{k}{p}\right]^2 dp \tag{72}$$

The inverse tangent can be expanded in the two regions as shown below.

$$\tan^{-1}\frac{k}{p} = \frac{\pi}{2} - \sum_{n=0}^{\infty} \frac{(-1)^n}{(2n+1)} \left(\frac{p}{k}\right)^{2n+1} \qquad \text{for } p < k$$

$$= \sum_{n=0}^{\infty} \frac{(-1)^n}{(2n+1)} \left(\frac{k}{p}\right)^{2n+1} \qquad \text{for } p > k$$

The integral can then be split into two parts.

$$\int_0^1 p\sqrt{1-p^2}\left[\tan^{-1}\frac{k}{p}\right]^2 dp$$

$$= \int_0^k p\sqrt{1-p^2}\left[\frac{\pi}{2} - \sum_{n=0}^{\infty}\frac{(-1)^n}{2n+1}\left(\frac{p}{k}\right)^{2n+1}\right]^2 dp$$

$$+ \int_k^1 p\sqrt{1-p^2}\left[\sum_{n=0}^{\infty}\frac{(-1)^n}{2n+1}\left(\frac{k}{p}\right)^{2n+1}\right]^2 dp \qquad (73)$$

We will first treat the integral from zero to k. In this region $\sqrt{1-p^2}$ will be replaced by 1 since the next contribution is $\mathcal{O}(k^2)$ compared to the part retained. Expanding this integral we get the following expression.

$$\int_0^k p\left[\frac{\pi}{2} - \sum_{n=0}^{\infty}\frac{(-1)^n}{2n+1}\left(\frac{p}{k}\right)^{2n+1}\right]^2 dp$$

$$= \int_0^k \left[\frac{\pi^2}{4} p - \pi \sum_{n=0}^{\infty} \frac{(-1)^n}{2n+1} \frac{p^{2n+2}}{k^{2n+1}} + \sum_{n=0}^{\infty} A_n \frac{p^{2n+3}}{k^{2n+2}} \right] dp \tag{74}$$

The value of A_n is given by

$$A_n = (-1)^n \sum_{m=0}^{n} \frac{1}{(2m+1)(2n-2m+1)} \quad . \tag{75}$$

Equation (74) can now be easily integrated term by term.

$$= \left[\frac{\pi^2}{8} - \pi \sum_{n=0}^{\infty} \frac{(-1)^n}{(2n+1)(2n+3)} + \sum_{n=0}^{\infty} \frac{A_n}{2n+4} \right] k^2 \tag{76}$$

The region from k to 1 is treated in a similar manner.

$$\int_k^1 p \sqrt{1-p^2} \left[\sum_{n=0}^{\infty} \frac{(-1)^n}{2n+1} \left(\frac{k}{p} \right)^{2n+1} \right]^2 dp$$

$$= \int_k^1 p \sqrt{1-p^2} \sum_{n=0}^{\infty} A_n \left(\frac{k}{p} \right)^{2n+2} dp \tag{77}$$

Interchanging integration and summation we get

$$= \sum_{n=0}^{\infty} A_n k^{2n+2} \int_k^1 \frac{\sqrt{1-p^2}}{p^{2n+1}} dp \quad . \tag{78}$$

For the case $n = 0$ we have

$$k^2 \int_k^1 \frac{\sqrt{1 - p^2}}{p}\, dp = - k^2\sqrt{1 - k^2} + k^2 \log\left(\frac{1 + \sqrt{1 - k^2}}{k}\right)$$

and for general $n > 0$ the leading term of the solution is

$$k^{2n+2} \int_k^1 \frac{\sqrt{1 - p^2}}{p^{2n+2}}\, dp = \frac{k^2}{2n} + \mathcal{O}(k^4) \quad .$$

Then to $\mathcal{O}(k^2)$ we have

$$\int_k^1 p\sqrt{1 - p^2}\left[\tan^{-1}\frac{k}{p}\right]^2 dp = - A_o k^2 - A_o k^2 \log k$$

$$+ k^2 \sum_{n=1}^{\infty} \frac{A_n}{2n} \quad . \tag{79}$$

The integral over the whole region from zero to one is then finally

$$\int_0^1 p\sqrt{1 - p^2}\left[\tan^{-1}\frac{k}{p}\right]^2 dp = \left[\frac{\pi^2}{8} - 1 + \log 2\right.$$

$$- \pi \sum_{n=0}^{\infty} \frac{(-1)^n}{(2n + 1)(2n + 3)}$$

$$+ \sum_{n=0}^{\infty} \sum_{m=0}^{n} \frac{(-1)^n}{(2n+4)(2m+1)(2n-2m+1)}$$

$$+ \frac{1}{2} \sum_{n=1}^{\infty} \sum_{m=0}^{n} \frac{(-1)^n}{n(2m+1)(2n-2m+1)} - \log k \Bigg] k^2 + \mathcal{O}(k^4) \tag{80}$$

The two double sums do not converge particularly rapidly so we set them up on a computer (an application it is eminently suited for). With an execution time of less than one second we are given the following result.

$$\int_0^1 p\sqrt{1-p^2} \left[\tan^{-1}\left(\frac{k}{p}\right)\right]^2 dp \doteq -\left[0.04 + \log k\right] k^2 \tag{81}$$

After substituting for k we have the solution for equation (71).

$$-\rho \int_0^a \varphi_z^2 \, dz = \rho a \nu^2 \left[0.04 + \log\left(-\frac{\pi}{4} \frac{\nu}{U a_x}\right)\right] \tag{82}$$

The third term in equation (59) is evaluated as follows.

$$-\rho \int_{-a}^{a} \varphi_t \, dz = -\rho \frac{\partial}{\partial t} \int_{-a}^{a} \varphi \, dz \tag{83}$$

This can be expressed using equations (62) and (69) in the following

form.

$$-\rho \frac{\partial}{\partial t} \int_{-a}^{a} \varphi \, dz = -\rho \frac{\partial}{\partial t} \left[-4 a^2 \epsilon U a_x + \frac{\pi}{2} a^2 \nu + \frac{\pi^2}{8} \frac{\nu^2 a^2}{U a_x} \right]$$

$$= -\frac{\pi}{2} \rho a^2 \dot{\nu} \qquad (84)$$

The other terms in equation (59), being constant across the span, are easily integrated. Equation (59) can then be written finally as

$$\frac{dN}{dx} = -\frac{\pi}{2} \rho U \frac{\partial}{\partial x} (a^2 \nu) - \frac{\pi^2}{8} \rho a \nu^2$$

$$+ \rho a \nu^2 \left[0.04 + \log \left(-\frac{\pi}{4} \frac{\nu}{U a_x} \right) \right] - \frac{\pi}{2} \rho a^2 \dot{\nu}$$

$$- \rho a (U y_o')^2 + \rho a (U \alpha - v_b)^2 . \qquad (85)$$

G. Specific Cases

For the case of a stationary ($v_b = 0$), flat ($y_o' = 0$) delta wing of apex angle β ($a_x = \beta/2$) equation (85) is

$$\frac{2}{\rho U^2} \frac{dN}{dx} = \frac{\pi}{2} \alpha \beta^2 x - \frac{\pi^2}{8} \alpha^2 \beta x$$

$$+ \alpha^2 \beta x \left[0.04 + \log \frac{\pi}{2} - \log \frac{\beta}{\alpha} \right] + \alpha^2 \beta x . \qquad (86)$$

The normal force is obtained by integrating equation (86) from the apex to the trailing edge. The normal force is reduced to a coefficient by dividing by the dynamic pressure and the foil planform area. The normal force coefficient is then given to be

$$C_N = \frac{\pi}{2}\beta\alpha + \left[0.26 - \log \frac{\beta}{\alpha}\right] \alpha^2 \quad . \tag{87}$$

The lift and drag coefficients can be obtained by projecting the normal force vector since there are no tangential forces from this theory. The normal force coefficient curve slope is given by

$$\frac{\partial C_N}{\partial \alpha} = \frac{\pi}{2}\beta + \left[1.52 - 2 \log \frac{\beta}{\alpha}\right] \alpha \quad . \tag{88}$$

If we oscillate the hydrofoil such that

$$v_b = \tilde{v} \sin \omega t \tag{89}$$

the sectional lift given by equation (85) becomes

$$\frac{2}{\rho U^2}\frac{dN}{dx} = \frac{\pi}{2}\beta^2 x \left(\alpha - \frac{\tilde{v}}{U}\sin\omega t\right) - \frac{\pi^2}{8}\beta x \left(\frac{\tilde{v}}{U}\sin\omega t - \alpha\right)^2$$

$$+ \beta x \left(\frac{\tilde{v}}{U}\sin\omega t - \alpha\right)^2 \left[0.04 + \log\left(-\frac{\pi}{2}\,\frac{\frac{\tilde{v}}{U}\sin\omega t - \alpha}{\beta}\right)\right]$$

$$+ \beta x \left(\frac{\tilde{v}}{U}\sin\omega t - \alpha\right)^2 - \frac{\pi}{4}\beta^2 x^2 \omega \frac{\tilde{v}}{U^2}\cos\omega t \tag{90}$$

If in the last term we write the reduced frequency as k, the time dependent normal force coefficient is given by

$$C_N(t) = \frac{\pi}{2}\beta\left(\alpha - \frac{\tilde{v}}{U}\sin\omega t\right) - \frac{\pi^2}{8}\left(\alpha - \frac{\tilde{v}}{U}\sin\omega t\right)^2$$

$$+ \left(\alpha - \frac{\tilde{v}}{U}\sin\omega t\right)^2\left[0.04 + \log\frac{\pi}{2} - \log\frac{\beta}{\alpha} + \log\left(1 - \frac{\tilde{v}}{U\alpha}\sin\omega t\right)\right]$$

$$+ \left(\alpha - \frac{\tilde{v}}{U}\sin\omega t\right)^2 - \frac{\pi}{3}\beta k\frac{\tilde{v}}{U}\cos\omega t \quad . \tag{91}$$

We might note that previously we have restricted the size of $U\alpha$ and v_b compared to Ua_x. More specifically, in terms of delta wing parameters, we have said that $\left(\frac{\alpha}{\beta}\right)^2 << 1$ and $\left(\frac{v_b}{U\beta}\right)^2 << 1$. We have not said anything about the ratio $(v_b/U\alpha)$. Because of the time dependent argument of the log term in equation (91) it will prove useful to take $(v_b/U\alpha) < 1$ so that we can expand the argument about one. The first term is clearly the dominant one of frequency ω. Let us consider only that part of $C_N(t)$ which is changing at the angular frequency ω and normalize the unsteady force coefficient components by dividing by the apparent change in angle of attack which is

$$\bar{\alpha} = -\frac{v_b}{U} \quad . \tag{92}$$

The unsteady coefficients then become

$$C_{N_{\bar{\alpha}_r}} = \frac{\pi}{2}\beta + 2\alpha\left[0.76 - \log\frac{\beta}{\alpha}\right]$$

and (93)

$$C_{N_{\bar{\alpha}_i}} = \frac{\pi}{3} \beta k \quad .$$

The subscripts r and i denote the component in-phase with the apparent angle of attack and the quadrature component respectively.

Figure 16 presents the theoretical value of $C_{N_{\bar{\alpha}_r}}/\beta$ as a function of α/β. It should be noted that $C_{N_{\bar{\alpha}_r}}$ and $\left.\frac{\partial C_N}{\partial \alpha}\right|_{\text{stationary}}$ have the same value. This is not entirely unexpected for a quasi-steady theory. A comparison of the theoretical and experimental values is given in the next section.

H. Conclusion

It is useful to recapitulate the differences in the assumed flow model and that observed in practice. Referring again to Figure 15 which is a sketch of the "actual" cross-flow, the free surface lies above the foil not in the plane of the foil. The spray extends over the foil but does not form a closed cavity. It should also be mentioned that the flow is not conical near the trailing edge. This effect is similar to the ventilated cases shown by Kiceniuk in reference (29). A slight lift loss over the aft portion of the foil results and this produces a pitch up moment compared to the theory.

The unsteadiness of the flow is represented in two alterations of the boundary conditions, one explicit, the other implicit. The explicit change is the addition of the heaving velocity at the foil. The

implicit change is in the spray position which is allowed to change with time. The unsteady behavior shows up in the "Bernoulli" equation but since the fluid is incompressible, time enters Laplace's equation only as a parameter.

The theory is limited because of the slender body assumption to values of $\beta << 1$. It is further limited by other assumptions, particularly the spray position, to values of $\left(\frac{\alpha}{\beta}\right)^2 << 1$. The model may have a small amount of camber and the heaving velocity must be small $v_b < U\alpha$.

It is interesting to note that the second term on the right hand side of equations (70) or (85) expresses the effect of the spray on the φ_x term. It yields a decreased force perhaps due to the momentum transferred to the upper half plane which is not recovered by the top side of the foil in the planing case. Tulin had suggested that the spray yielded an effective widening of the foil. His answer has an incorrect sign on this term. In view of this his conclusion seems in error.

V. DISCUSSION OF THE EXPERIMENTAL DATA AND THEORETICAL CALCULATIONS

A. Fully Wetted Flow

The experimental results are separated into three parts: fully wetted, ventilated and planing. The division is a natural one due to the quite different flow around the foil in each case. The fully wetted data and theories are considered first.

The fully wetted data constitute the largest portion of both the experimental data and the theoretical studies of previous authors. The effect of submergence has not been dealt with in these theoretical studies as they were motivated by aeronautical considerations, but they are otherwise applicable due to the small influence of the Reynolds number as was discussed by Smith (4).

The fully wetted data are broken down into that for the 15^{o} delta wing and that for the 30^{o} delta wing. Figures 17, 18 and 19 present the unsteady lift, drag and pitching moment about the model's planform centroid for the 15^{o} delta wing at 0.83 chords submergence. Figures 20, 21 and 22 present the same data at 0.50 chords submergence and Figures 23, 24 and 25 are for a submergence of 0.17 chords.

Also shown on Figure 17 is the effect of reduced frequency on the unsteady lift as calculated by Lawrence and Gerber (24). Because they did not present data for the aspect ratios tested, the results used here are interpolated from their tabular values. Their results agree quite well, as can be seen from the figure, with the data

for zero angle of attack.

There is a sizable non-linear angle of attack effect on the in-phase lift but almost no effect on the quadrature lift. The non-linear effect is presumably due to leading edge separation since the foils have sharp edges. The quadrature lift seems to be an apparent mass effect since it is linear in reduced frequency but the slope is somewhat smaller than that calculated using the "linear" model.

The in-phase drag data also exhibit a non-linear effect greater than the projection of a linear value of normal force. One expects the lift and drag forces to be related by the angle of attack since due to the separated edges the loading should be mostly normal to the foil. The in-phase drag exhibits a fairly large reduced frequency effect at non-zero angles of attack. This is believed to be a real effect, not an experimental problem. The quadrature drag is about as expected except for reduced frequencies less than one where the data are independent of angle of attack.

The in-phase pitching moment is very small for the 15^{o} delta wing. A slight pitch-up moment is noted probably due to the lack of conicality near the trailing edge. The reason for the unusual behavior of the quadrature pitching moment with angle of attack is not known.

Figures 20, 21 and 22 illustrate that the free surface effect is negligible at 0.50 chords submergence. At 0.17 chords submergence, illustrated in Figures 23, 24 and 25, there is a noticeable free surface effect. All of the values are reduced slightly. What is particularly noticeable, however, is that the quadrature lift and drag are negative at low reduced frequency, particularly at the largest

angle of attack. It might be expected that since this is a surface effect it might be Froude number dependent but no investigations of this were undertaken.

Recent theoretical treatments of delta wings have been primarily concerned with the description of the flow resulting from the leading edge separation. This separation produces a sizable non-linear effect as was noted in the data. Figure 26 presents a summary of the major steady theories calculated for the 15^{o} delta wing at each of the angles of attack tested. Also presented for comparison is the mean of the experimental data at different reduced frequencies for each of the angles of attack.

The zero angle of attack value is fairly well predicted by Jones' method. The agreement with the Brown-Michael theory is not good and appears to get worse with increasing angle of attack. The Mangler-Smith theory also does not show good agreement but it may be better at even higher angles of attack. The theory which is by far the best is that of Gersten. The symbols actually overlap at six degrees. The Gersten result lies under the experiment at twelve degrees. This might indicate that Gersten's theory is better for small angles of attack, say $\alpha < \beta$. It would be interesting to compare the Mangler-Smith theory for $\alpha > \beta$; unfortunately no data were taken for that range of angles of attack.

Figures 27, 28 and 29 present the unsteady lift, drag and pitching moment coefficients for the 30^{o} delta wing at 0.83 chords submergence. Figures 30, 31 and 32 present the same data at 0.50 chords submergence and Figures 33, 34 and 35 at 0.17 chords

submergence.

Figure 27 also shows the effect of reduced frequency as calculated by Lawrence and Gerber. As for the 15° foil the agreement with the zero angle of attack data is quite good for both in-phase and quadrature lift.

There is a significant non-linear angle of attack effect on the in-phase experimental data. As for the more slender model the quadrature lift is almost independent of angle of attack.

The in-phase drag exhibits marked angle of attack and reduced frequency effects. The reason for the negative in-phase drag at zero angle of attack is not known. The nearness of the quadrature drag to zero at zero angle of attack seems to indicate that the foil is perpendicular to the oscillation. The effect, or lack thereof, of angle of attack on the quadrature drag for reduced frequencies less than one is much the same as for the 15° foil.

The pitching moment exhibits a larger value for the 30° foil presumably because the model is not really a slender body and the reduced loading on the aft of the foil increases the moment.

Figures 30, 31 and 32 present the data for 0.50 chords submergence. The submergence effect is very small but the data serve as a useful check on the data at 0.83 chords submergence.

The effect of the free surface is quite noticeable in Figures 33, 34 and 35 which are for a submergence of 0.17 chords. The effect is most noticeable at the largest angle of attack for which the free surface is quite distorted. These three figures illustrate the facts that the effect of the free surface is small unless the foil is quite

close and also that if the foil is close the effect can be large.

Figures 36, 37 and 38 present the effect of oscillation amplitude. The oscillation amplitude is labeled with a voltage since it is that which is fed into the force servo controller. The nominal voltage was 4 v. and this series of runs was accomplished at 2 v. and 3 v. to establish the linearity of the effect so that the coefficients could be normalized by the apparent angle of attack change. The validity of this assumption is well substantiated by the data with only a few spurious points not collapsing together.

Figures 39, 40 and 41 present the effect of using different frequency-velocity combinations to obtain various reduced frequencies ($k = \frac{\omega c}{2U}$). As can be seen from the agreement of the data at the same reduced frequencies and the smooth behavior with reduced frequency, this is the proper reduction parameter.

Data were also taken at negative six and twelve degrees angle of attack. These data are presented in Figures 42, 43 and 44. Little effect of reversing the sign of the angle on the quadrature lift is noted. The in-phase lift changed more particularly at the intermediate angle of attack. In fact all three coefficients showed the greatest change for six degrees angle of attack.

The reason for the negative angle effects is obscured by the parameters involved. It could be due to the support strut, the camber or not quite having zero lift at the defined zero angle of attack or even the tunnel boundary effects, though that seems highly unlikely. It seems more likely that at this relatively small angle of attack the camber is affecting the separated flow slightly but that is just a guess.

Figure 45 presents a summary of the major steady theories calculated for the 30^{o} delta wing at each of the angles of attack tested. Also presented for comparison is the mean of the experimental data at different reduced frequencies for each of the angles of attack.

The zero angle of attack value is not as accurately predicted by Jones' theory, presumably because the 30^{o} wing is not really "slender". Both the Brown-Michael and Mangler-Smith theories give poor agreement with the experimental data. As for the 15^{o} model Gersten's theory is by far the best. His theory overpredicts the coefficient at six degrees but is almost exact at twelve degrees angle of attack. Even though his model does not depict the actual flow field, it would be useful to develop an unsteady counterpart of Gersten's theory since it predicts the forces fairly well.

B. Ventilated Flow

It was originally intended to test both models with ventilated cavities but only the 30^{o} apex angle delta wing was tested for reasons described in Section I. Also due to the additional parameter cavity length, and associated parameters cavity pressure and air supply rate, the tests were limited to one submergence and one angle of attack. These investigations were not intended to be as extensive as the other measurements but were intended as a first look into an uninvestigated area.

Figures 46 and 47 present the unsteady lift and drag coefficients at various cavity lengths and reduced frequencies. The behavior of the coefficients with cavity length is odd but not entirely

unexpected in view of the findings of Klose (2). Projections of the steady values of C_{N_α} calculated by Kaplan, et al (26) using the Cumberbatch-Wu theory at a cavitation number of zero are also presented on the figures. It can be seen from the figures that this underpredicts the experimental data at the lowest reduced frequency and largest cavity length (i.e., lowest ventilation number).

Although it was not possible in this series of investigations it would be very interesting to have measurements of the unsteady cavity pressure during the oscillation cycle. Before a valid model can be established to attempt the calculation of the unsteady forces, more investigation needs to be done to find the proper boundary conditions.

Also presented are the measured average ventilation number and average air supply coefficient. These are presented as functions of cavity length in Figures 48 and 49. There is a direct correlation of ventilation number with cavity length independent of reduced frequency. The same situation seems to exist for air supply coefficient at least at the lower cavity lengths. At the higher cavity lengths the correlation appears to be non-existent. This may be due to the relatively small working section area compared to the cavity area at long cavity lengths. It may also be due in part to the difficulty in determining the cavity termination point especially when the cavity is long.

High speed flash photographs of four ventilated flows are presented in Figure 20. Photograph a) shows a low reduced frequency and fairly short cavity. The bursts of bubbles entrained

in the wake are due to the basic flow, not the forced oscillation. The frequency of the heaving oscillation is much lower than the shedding frequency.

Photograph b) presents a higher reduced frequency and slightly shorter cavity length. The oscillation may be seen in the sinusoidal mean position of the wake. As can be seen in all the photographs the entrainment in the region of cavity closure makes determination of the cavity length difficult.

Photograph c) shows a higher reduced frequency still and a cavity length about the same as in the first case. The bubbles entrained into the shed vorticity are clearly seen.

Photograph d) shows the same reduced frequency as c) but with a longer cavity length. The waves on the cavity wall are easily seen. The large quantity of air in the wake illustrates why this case has the largest air supply coefficient.

It might be noted that all the cavities are smooth along the first half chord and not over the aft part. The reason for this is that the septum (see the illustration in Kiceniuk's report) sprays onto the cavity wall providing this effect.

C. Planing Flow

Measurements for planing flow presented their own unique problems. The contents of the section after this are a result of one of these problems. The effort taken to make sure that the data are meaningful is discussed in the section on experimental procedure and will not be repeated here, but it will be emphasized that where

the theory and data do not agree the theory must be inadequate.

Both the 15^{o} and 30^{o} delta wing models were tested in planing. Angles of attack of six and twelve degrees were run for each of the models. Only one free stream velocity was run (U = 22 ft/sec) since this was as high as practical and the heaving amplitude was kept as small as practical to lessen the wetted area change.

Figures 51, 52 and 53 present the unsteady lift, drag and pitching moment coefficients for the 15^{o} delta wing. Also shown on the figures are the theoretical calculations of Section IV. The agreement of the theory and the in-phase lift is poor which is not too surprising for this foil since the theory was developed for small angle of attack to apex angle ratios. The logarithmic behavior of the theory is too strong compared to the other non-linear term. The coefficient is underpredicted. The quadrature lift, on the other hand, is quite accurately predicted with the experimental points lying along the predicted line.

The drag is slightly better predicted by the theory although the smallness of the values makes the agreement seem better than it really is. The quadrature drag is negative below a reduced frequency of one-half for the experimental data. It is unknown if this is a real planing effect. The pitching moment data exhibit much the same behavior as for the fully wetted flow.

High speed flash photographs of the 15^{o} delta wing planing at three reduced frequencies are presented in Figure 54. The disturbance of the cavity shape due to the oscillation is seen in the bottom two photographs.

Figures 55, 56 and 57 present the unsteady lift, drag and pitching moment data for the planing 30^{o} delta wing. Also presented are the results of Section IV calculated for these cases. It would be expected that since the angle of attack to apex angle ratio is substantially less than one here the theory would predict accurately the experimental values. Unfortunately such is not the case.

It is seen from Figure 55 that the in-phase lift is also underpredicted for this foil. Again the logarithmic behavior causes the coefficient to be too small. The quadrature lift is predicted quite accurately as for the other foil.

The in-phase drag seems again to be predicted more accurately than the lift but the gain is more apparent than real. The quadrature drag is somewhat overpredicted by the theory, perhaps because the 30^{o} foil is not really a very slender body. The pitching moment data are for the most part as expected.

Figure 58 presents high speed flash photographs of the 30^{o} delta wing planing at three reduced frequencies. The angle of attack is only six degrees in this case, consequently the cavity is shallower than for the other case where the angle of attack was twelve degrees. The distortions in the cavity due to the oscillation are evident in the bottom picture, especially the one of higher reduced frequency.

The failure of the theory of Section IV to accurately predict the forces seems probably due to the inadequacy of the cross-flow model. Representation of the spray by singularities of this form may be satisfactory as a limiting case but it does not stand the test of experimentation. A new cross-flow model needs to be developed

which does not have this logarithmic term or at least a stronger term quadratic in angle of attack.

D. Part-Cycle-Planing

In the course of the planing experiments it was discovered that if the foil was oscillated such that it was planing during the upper part of the cycle and fully wetted during the lower part of the cycle, the phase of the lift force would change drastically. This effect was so striking that it was decided it should be reported and for convenience it was named part-cycle-planing.

During this part-cycle-planing operation the in-phase lift coefficient becomes negative which means that an oscillation could start for an elastically mounted foil. It was obvious that the oscillation amplitude could not grow too large so a series of runs was made at different free stream velocities and frequencies to determine the amplitude at which no net energy was received by the foil from the fluid. The results of this survey are presented in Figure 59.

The data presented in Figure 59 are not intended to be an accurate representation of the boundary but only a cursory look at the effect. It is difficult to make measurements in this case due to the basic instability of the flow. Even though reduced frequency is used to plot the data in Figure 59 it is clear that this is not the proper reduction parameter. There is undoubtedly a Froude number effect.

Two high speed flash photographs of the 30^{o} delta wing

operating in the part-cycle-planing mode are presented in Figure 60. In the upper photograph the foil has just ceased to plane. The cavity is almost unchanged except at the front of the foil. In the lower picture the cavity has collapsed and only the ventilated leading edge vortices remain.

The point of this section is that unless they are designed to operate with sufficient static apex height, planing delta wings could lead to a very rough riding hydrofoil craft even if nothing catastrophic happened.

VI. SUMMARY AND CONCLUDING REMARKS

In this thesis we have traced the history of previous theoretical studies of the separated flow about delta wings. We have discussed the development of the Legendre model, the Brown-Michael model and the Mangler-Smith model and we have noted the Gersten model which is a separate type of theory. In addition to discussing these fully wetted flow models we have seen that flow models for fully ventilated and planing delta wings exist (i.e., the Cumberbatch-Wu and Tulin models respectively) but have received less attention presumably because they do not have aeronautical application (barring landing gear use).

In the current experimental investigations the unsteady lift, drag and pitching moment were measured for the two delta wings oscillating in heave while fully wetted, ventilated and planing, and the data are presented as a function of reduced frequency. For the ventilated flow, measurements were also made of the cavity pressure and air supply rate and these effects have been presented. The experimental apparatus is discussed, though only in detail for non-standard items.

A theoretical investigation of the forces on a planing delta wing was accomplished using Tulin's model. The problem was extended to unsteady motions by neglecting waves on the free surface. The unsteady motions were represented in the flow model through time dependence of the boundary conditions on the foil and through time dependence in the spray position.

The poor agreement of the Brown-Michael and Mangler-Smith models with the fully wetted data leads to the conclusion that little is to be gained by extending them to unsteady motions. By far the best agreement in the fully wetted case was obtained with the Gersten model. An extension of this theory to unsteady motions could be useful even though the dissimilarity between the theoretical flow field and that actually observed seems to indicate that little would be learned about the basic fluid mechanics.

An extension of the Cumberbatch-Wu theory able to produce the loop-shaped curves presented for the ventilated case seems doubtful. Additional investigations of the cavity pressure are needed to determine the appropriate boundary conditions before a realistic modeling of the flow could be attempted, if then.

The flow model of the planing delta wing produces logarithmic dependence of the force coefficients which is too large compared to the quadratic effect of angle of attack. Another cross-flow model, perhaps one which appears more like the actual flow described herein, is needed before accurate predictions can be made.

REFERENCES

1. H. N. Abramson, W.-H. Chu and J. T. Irick, "Hydroelasticity with Special Reference to Hydrofoil Craft", Naval Ship Research and Development Center, Report 2557, September 1967.

2. G. J. Klose, "Unsteady Forces on Oscillating Hydrofoils", Ph.D. Thesis, California Institute of Technology, 1966.

3. G. J. Klose and A. J. Acosta, "Unsteady Force Measurements on Fully Wetted Hydrofoils in Heaving Motion", J. Ship Res. 12, pp. 69-80, March 1968.

4. J. H. B. Smith, "Improved Calculations of Leading-edge Separation from Slender Delta Wings", R.A.E. Tech. Rept. No. 66070, March 1966.

5. R. T. Jones, "Properties of Low-Aspect-Ratio Pointed Wings at Speeds Below and Above the Speed of Sound", NACA Report 835, 1946.

6. M. Roy, "Caractères de l'Écoulement autour d'une Aile en Fleche Accentuée", C. R. Acad. Sci., Paris, 234, 2501, 1952.

7. R. Legendre, "Écoulement au Voisinage de le Point Avant d'une Aile a Forte Fleche aux Incidences Moyennes", 8th Int. Cong. Th. Appl. Mech., Istanbul, 1952, Rech. Aero., No. 30, 1952 and Rech. Aero., No. 31, 1953.

8. M. C. Adams, "Leading-edge Separation from Delta Wings at Supersonic Speeds", J. Aero. Sci., 20, p. 430, 1953.

9. C. E. Brown and W. H. Michael, "On Slender Delta Wings with Leading-edge Separation", NACA TN 3430, April 1955. Also J. Aero. Sci., 21, pp. 690-694 and 706, 1954.

10. R. H. Edwards, "Leading-edge Separation from Delta Wings", J. Aero. Sci., 21, pp. 134-135, 1954.

11. K. W. Mangler and J. H. B. Smith, "A Theory of the Flow Past a Slender Delta Wing with Leading Edge Separation", Proc. Roy. Soc. A, 251, pp. 200-217, 1959 (R.A.E. Rept. Aero 2593, 1957).

12. K. Gersten, "Calculation of Non-linear Aerodynamic Stability Derivatives of Aeroplanes", AGARD Rept. No. 342, April 1961.

13. D. J. Marsden, R. W. Simpson and W. J. Rainbird, "The Flow Over Delta Wings at Low Speeds with Leading-edge Separation", College of Aeronautics Rept. No. 114, ARC 20409, 1957.

14. D. Küchemann, "Report on the I.U.T.A.M. Symposium on Concentrated Vortex Motions in Fluids", J. Fluid Mech. 21, pp. 1-20, January 1965.

15. M. Roy, "On the Rolling-up of the Conical Vortex Sheet above a Delta Wing", Prog. in Aero. Sci., 7, pp. 1-5, 1966.

16. R. Legendre, "Vortex Sheets Rolling-up along Leading-edges of Delta Wings", Prog. in Aero. Sci., 7, pp. 7-33, 1966.

17. J. H. B. Smith, "Theoretical Work on the Formation of Vortex Sheets", Prog. in Aero. Sci., 7, pp. 35-51, 1966.

18. H. C. Garner and D. E. Lehrian, "Non-Linear Theory of Steady Forces on Wings with Leading-Edge Flow Separation", A. R. C. R&M No. 3375, 1964.

19. J. W. Miles, "On Non-Steady Motion of Slender Bodies", Aero. Quart. 2, pp. 183-194, 1950.

20. I. E. Garrick, "Some Research on High-Speed Flutter", Proc. Third Anglo-American Aero. Conf., 1951, pp. 419-446.

21. D. G. Randall, "Oscillating Slender Wings with Leading-edge Separation", Aero. Quart., Vol. 17, pp. 311-331, 1966.

22. M. V. Lowson, "The Separated Flow on Slender Wings in Unsteady Motion", A. R. C. R&M No. 3448, 1967.

23. R. R. Maltby, P. B. Engler and R. F. A. Keating with an Addendum by G. F. Moss, "Some Exploratory Measurements of Leading-edge Vortex Positions on a Delta Wing Oscillating in Heave", A. R. C. R&M No. 3410, 1965.

24. H. R. Lawrence and E. H. Gerber, "The Aerodynamic Forces on Low Aspect Ratio Wings Oscillating in an Incompressible Flow", J. Aero. Sci. 19, pp. 769-781, 1952; See also: Errata, J. Aero. Sci. 20, p. 296, 1953.

25. M. P. Tulin, "Supercavitating Flow Past Slender Delta Wings", J. Ship Res. 3, No. 3, 1959.

26. P. Kaplan, T. R. Goodman and C. C. Chen, "A Hydrodynamic Theory for Cavitating Delta Wing Hydrofoils", Oceanics Inc. Tech. Rept. No. 67-33, December 1966.

27. E. Cumberbatch and T. Y.-T. Wu, "Cavity Flow Past a Slender Pointed Hydrofoil", J. Fluid Mech. 11, Part 2, pp. 187-208, 1961.

28. H. Reichardt and W. Sattler, "Three-Component Measurements on Delta Wings with Cavitation", Max-Planck-Institut fur Stromungsforschung, Göttingen, July 1962.

29. T. Kiceniuk, "Superventilated Flow Past Delta Wings", California Institute of Technology Engineering Division Rept. No. E-101.5, July 1964.

30. M. P. Tulin, "The Theory of Slender Surfaces Planing at High Speeds", Forschungshefte fur Schiffstechnik, 4, 1956/57.

31. R. T. Knapp, J. Levy, J. P. O'Neill and F. B. Brown, "The Hydrodynamics Laboratory of the California Institute of Technology", Trans. ASME 70, July 1948, pp. 437-457.

32. G. Tricomi, "Integral Equations", Interscience Pub., Inc., New York, 1957, p. 173.

33. Bateman Manuscript Project, "Tables of Integral Transforms", Vol. II, McGraw-Hill Book Co., Inc., New York, 1954.

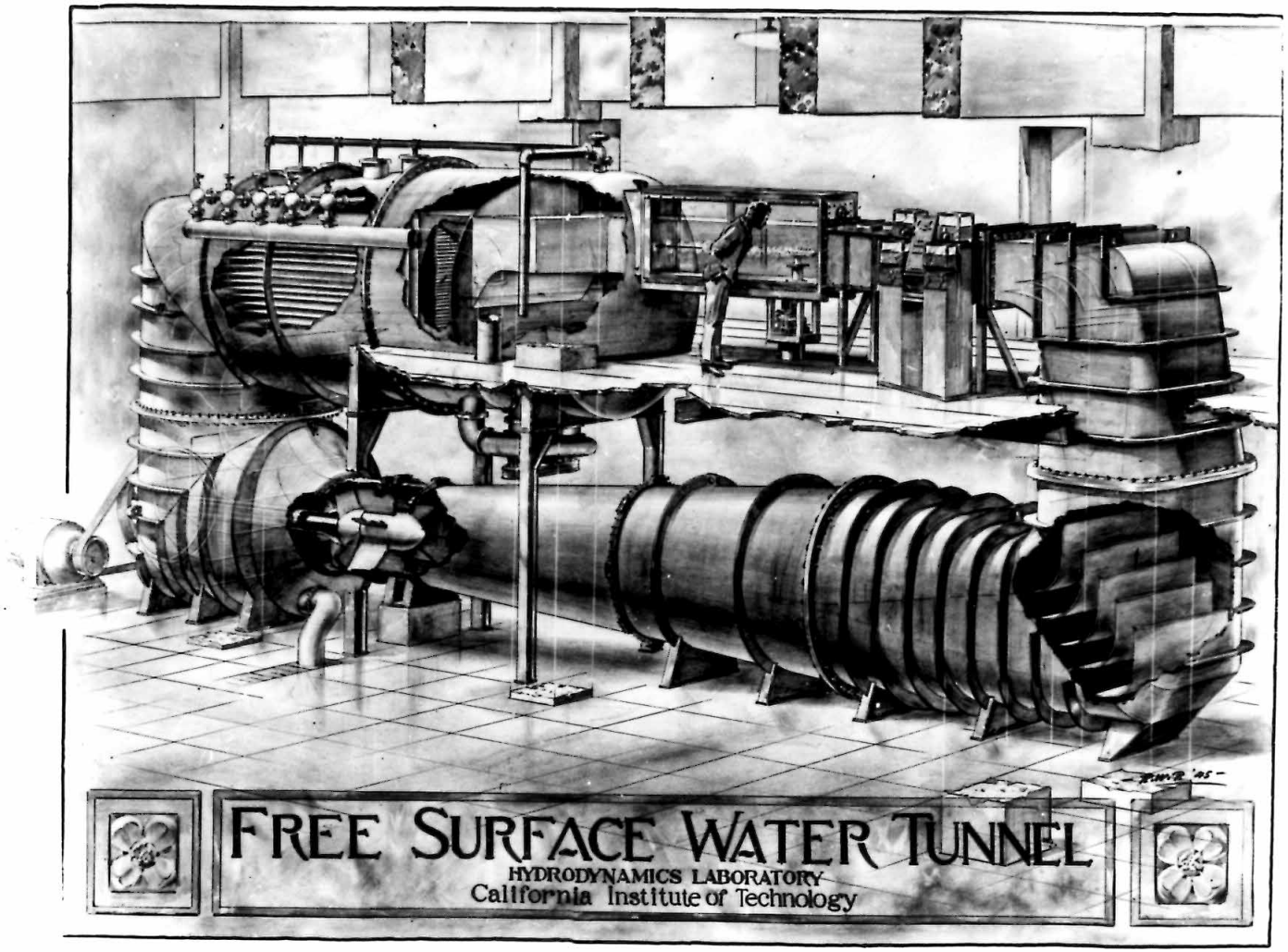
FREE SURFACE WATER TUNNEL
HYDRODYNAMICS LABORATORY
California Institute of Technology

Figure 1

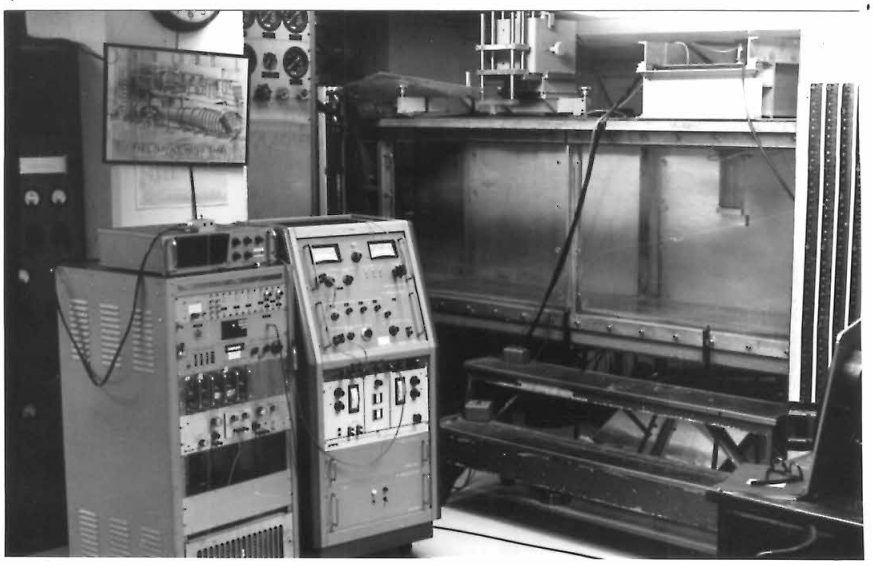

Figure 2 - View of the tunnel working section and the electronic apparatus.

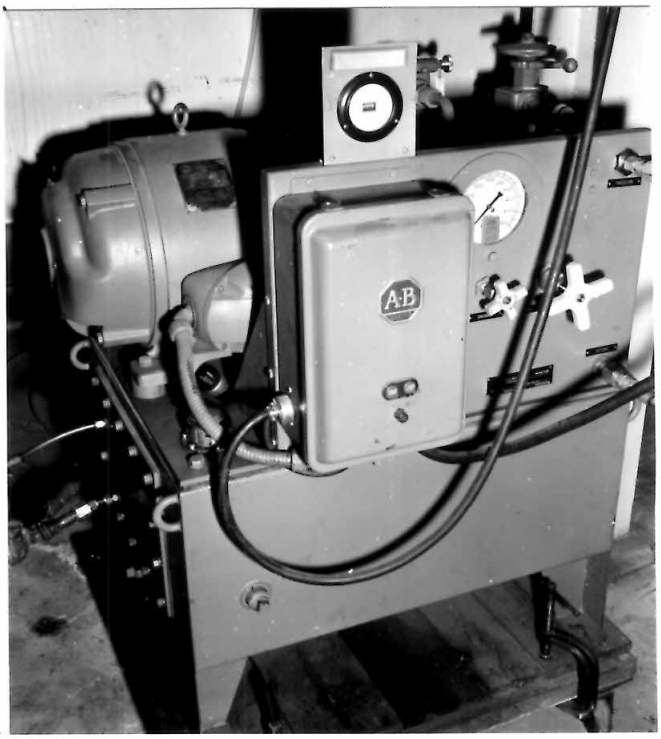

Figure 3 - The hydraulic pump and reservoir.

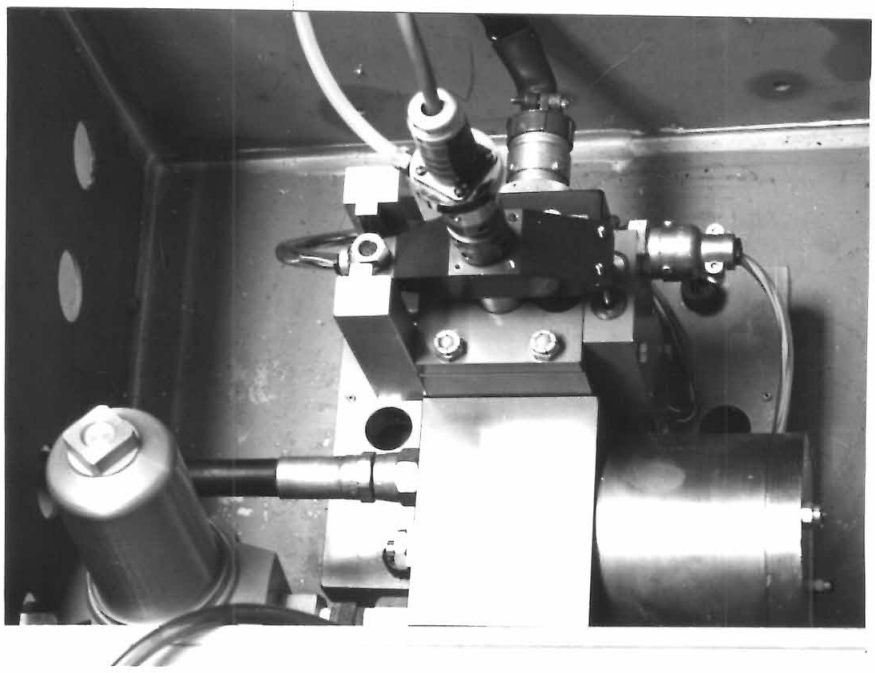

Figure 4 - Top view of the hydraulic oscillator.

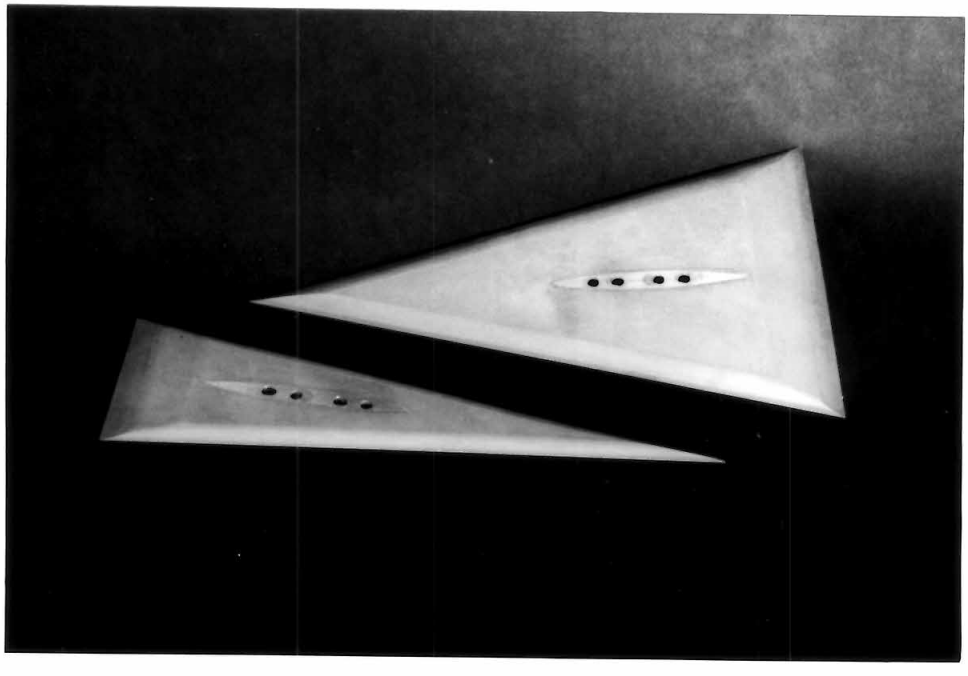

Figure 5 - The two delta wing models.

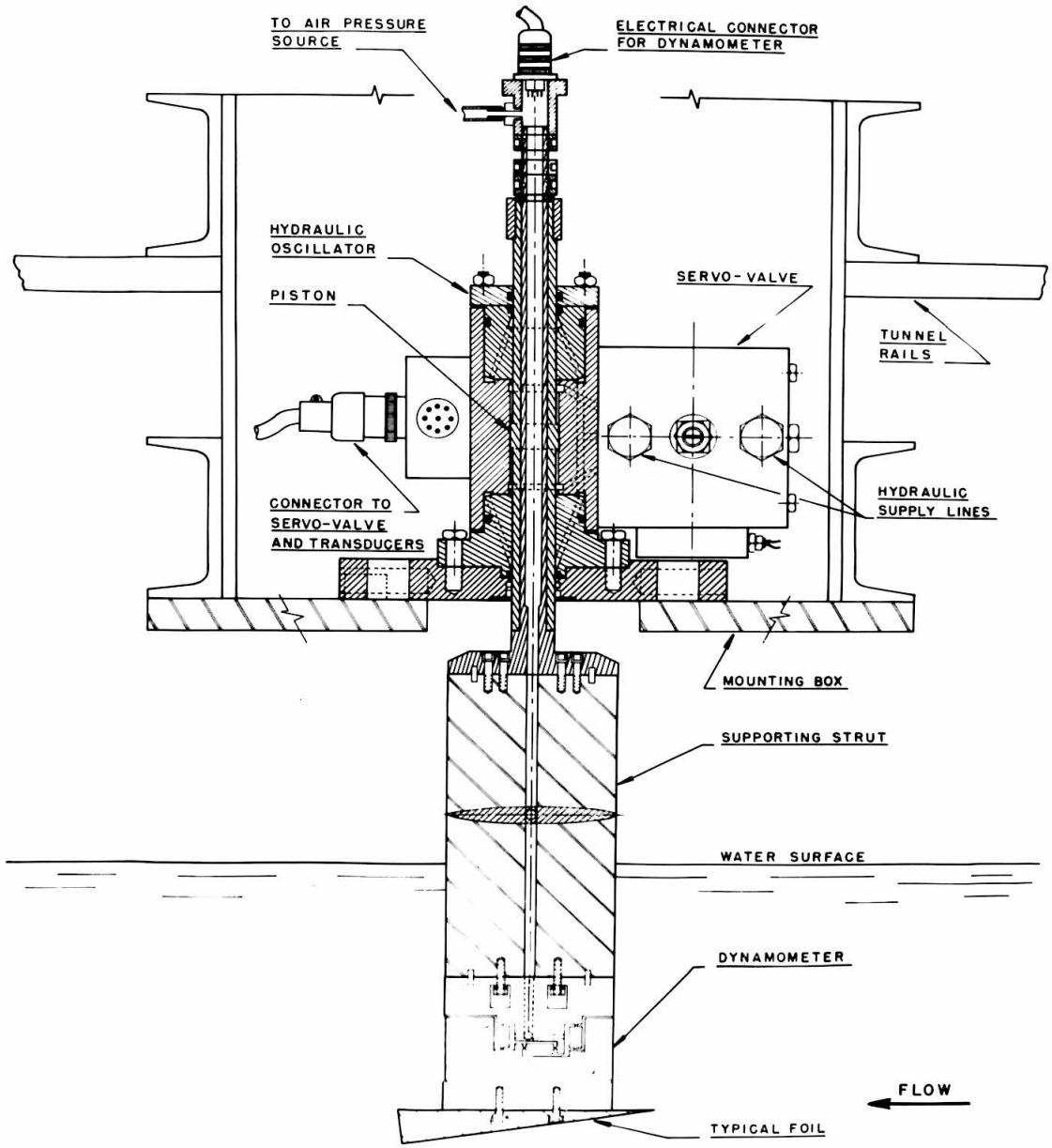

Figure 6 - Cross-section drawing of the hydraulic oscillator showing the tunnel mounting, balance (dynamometer) location and hydrofoil location.

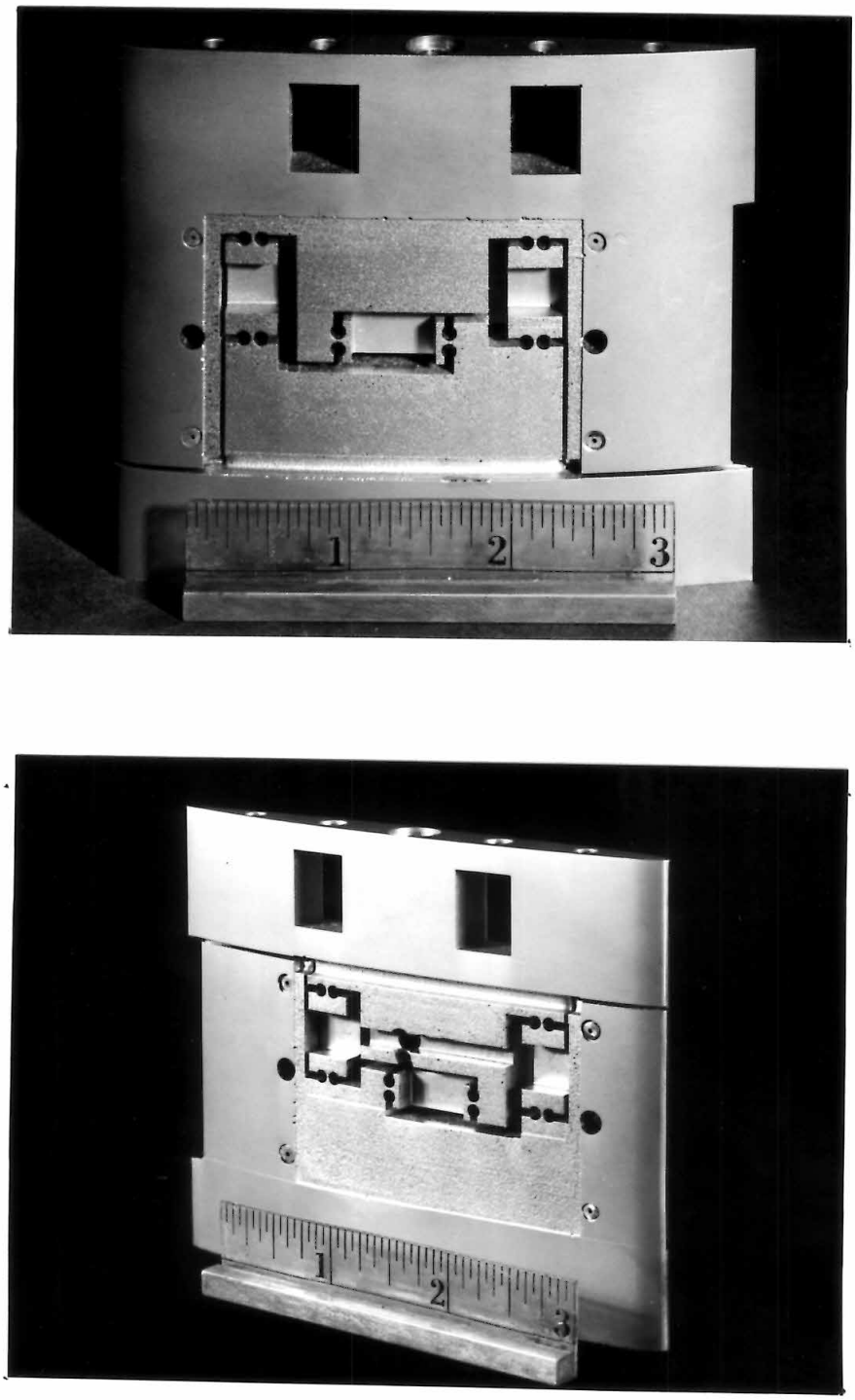

Figure 7 - The lift and pitching moment balance, seen from both sides, before affixing the strain gages.

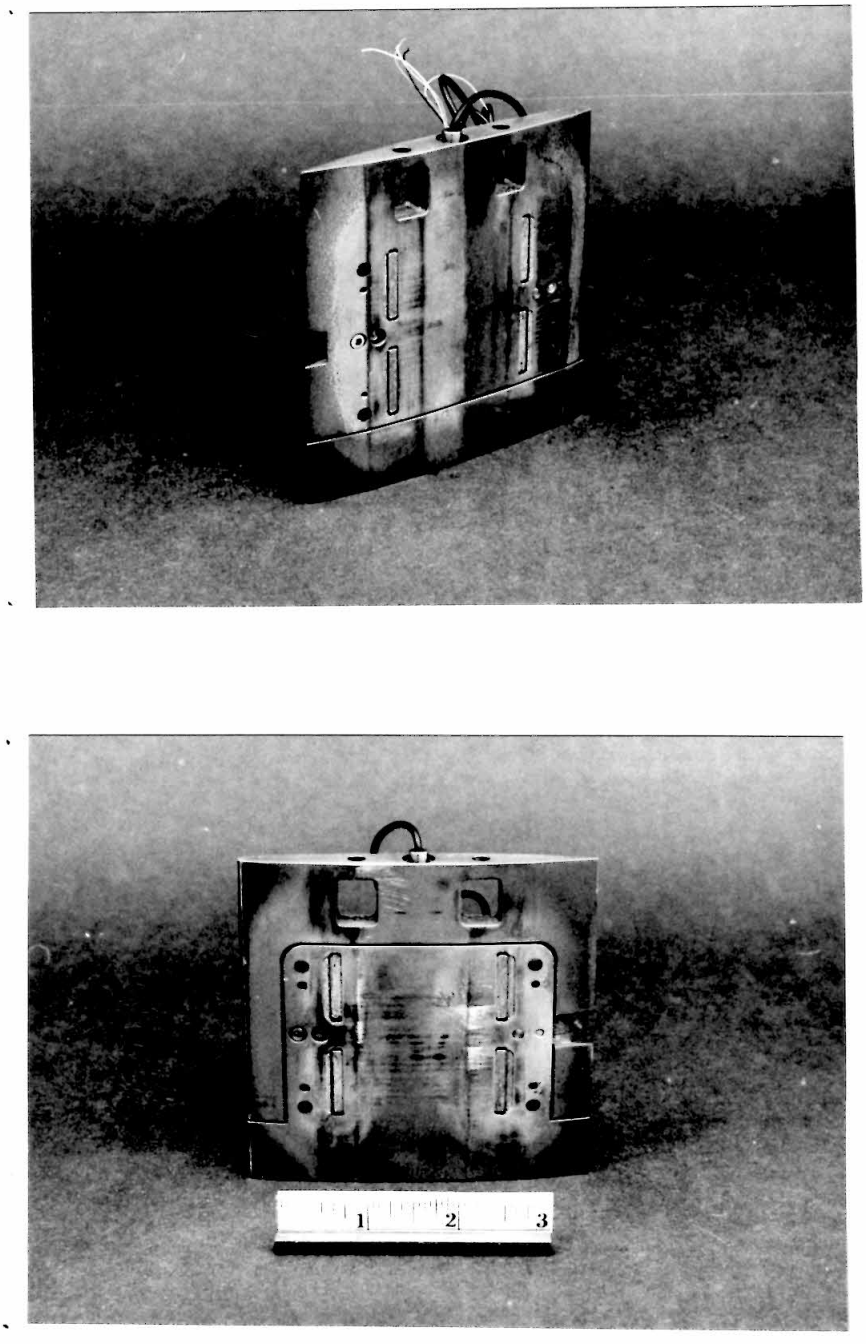

Figure 8 - The drag balance, seen from both sides, without waterproofing.

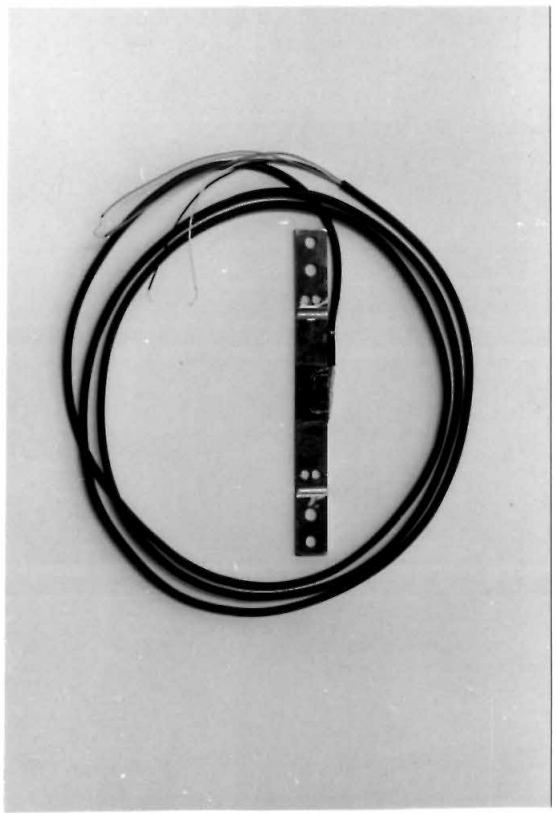

Figure 9 - The drag link showing the solid state strain gages.

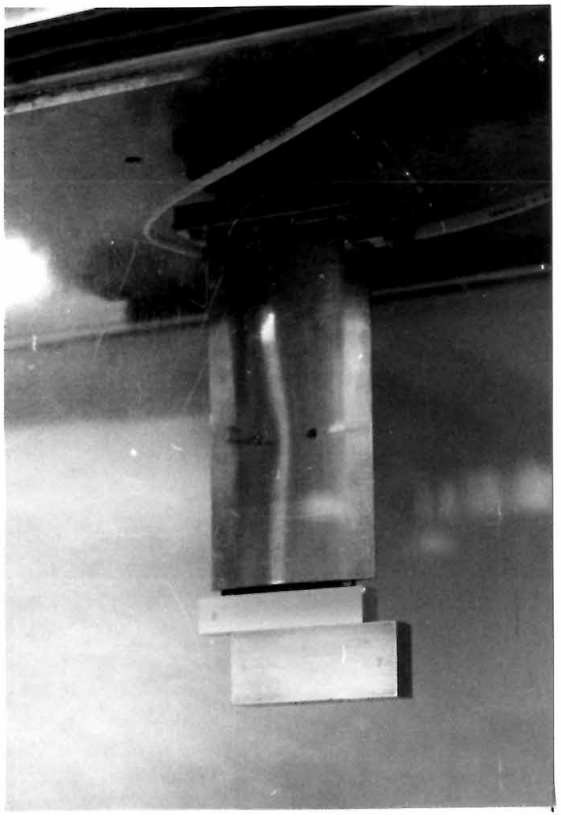

Figure 10 - The ventilation strut and balance calibration mass.

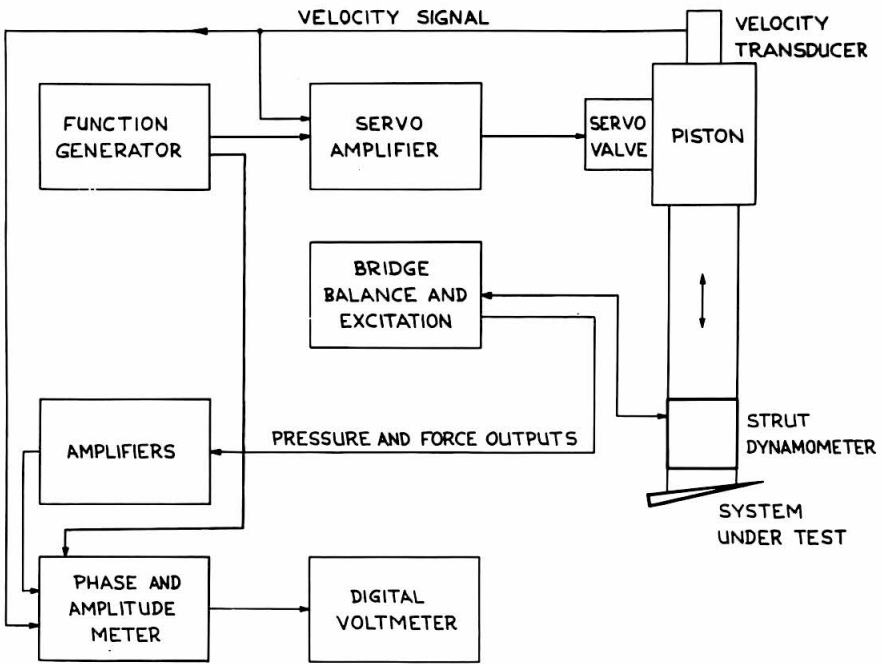

Figure 11 - Diagram of the electronic equipment for the hydraulic oscillator and data acquisition.

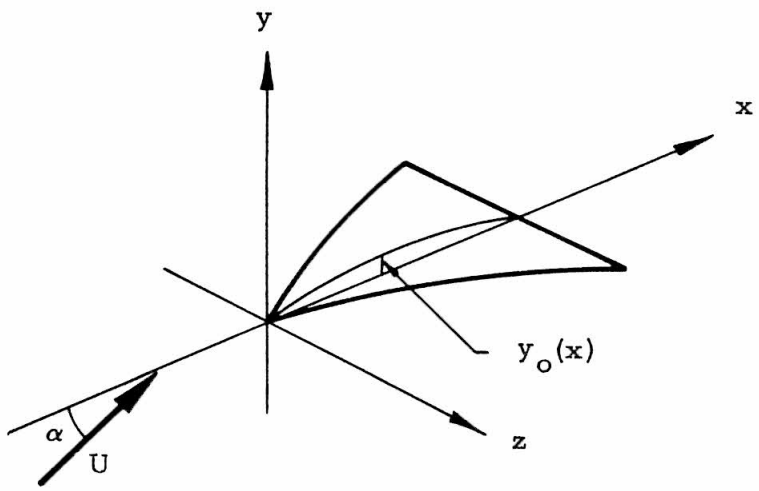

Figure 12 - The coordinate system used to calculate planing loads.

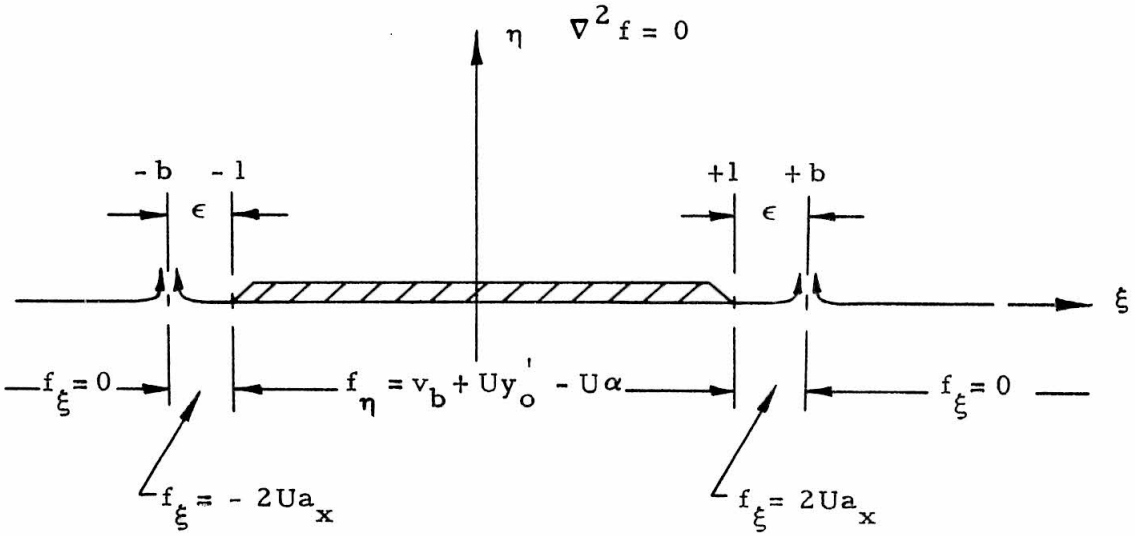

Figure 13 - The boundary value problem in the reduced cross-flow plane.

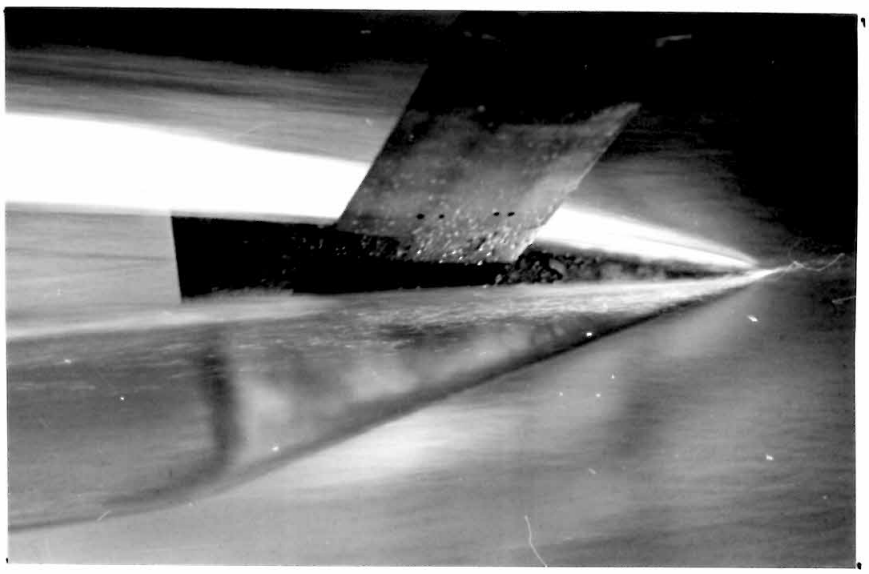

Figure 14 - Photograph of the 30° delta wing hydrofoil planing at a small angle of attack.

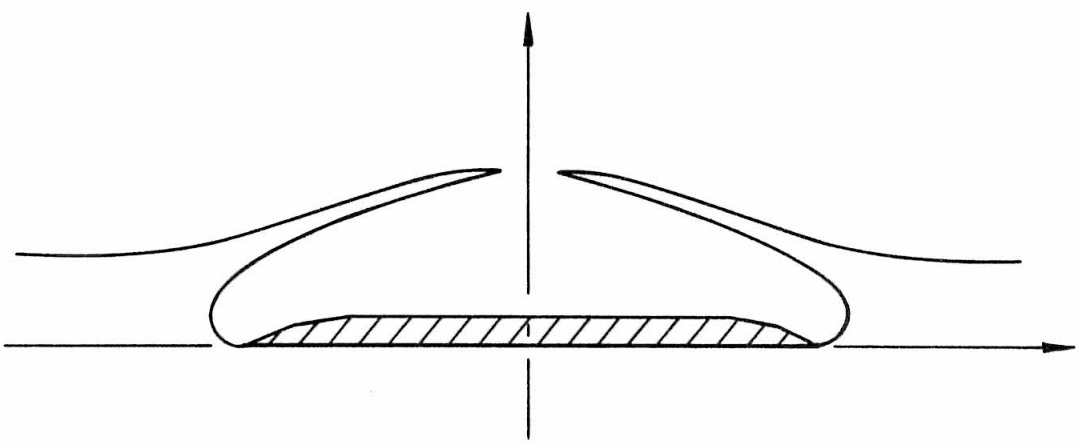

Figure 15 - Sketch of the actual cross-flow.

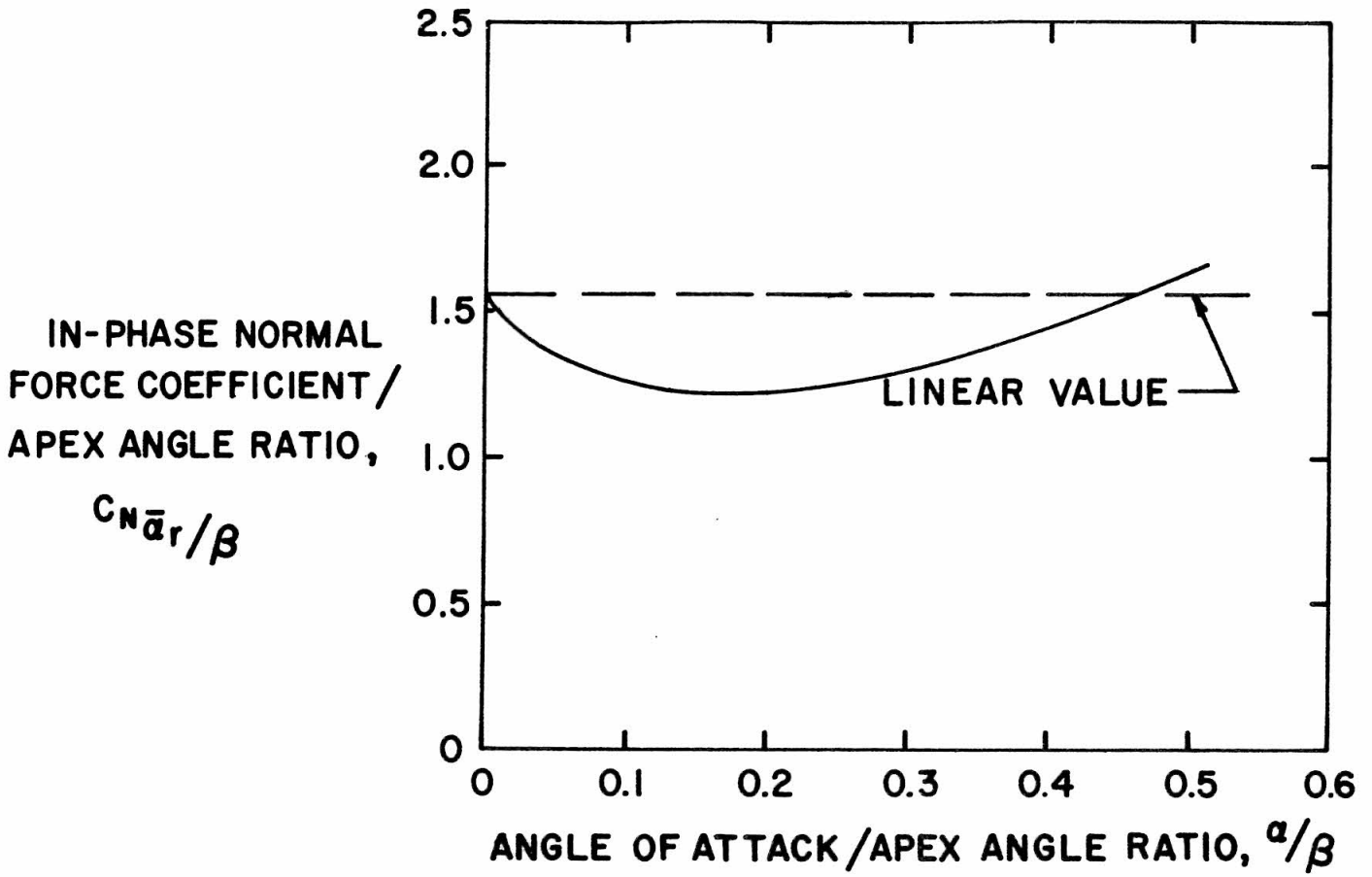

Figure 16 - Theoretical quasi-steady normal force curve slope.

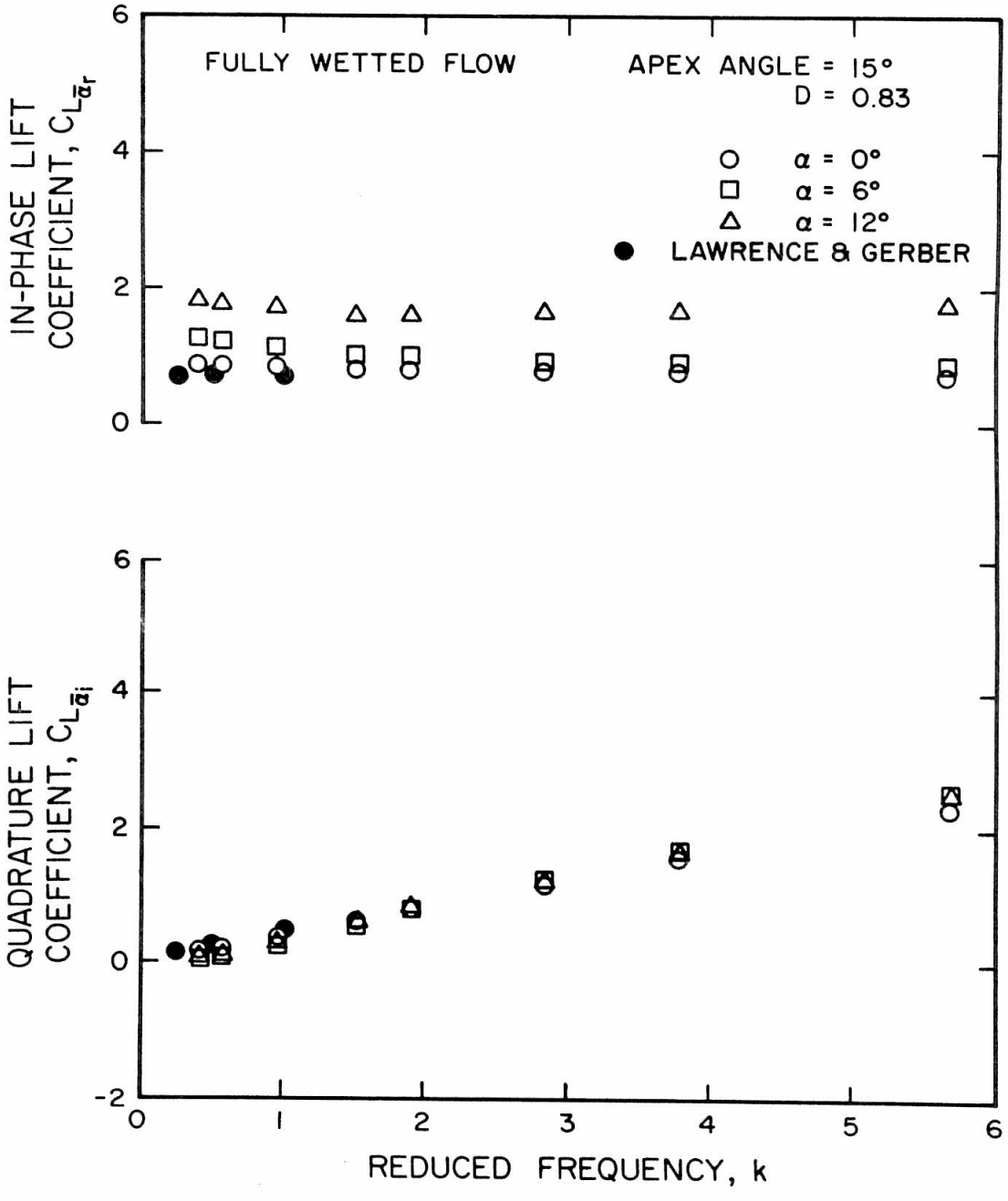

Figure 17 - Unsteady lift coefficients for the 15° delta wing at 0.83 chords submergence.

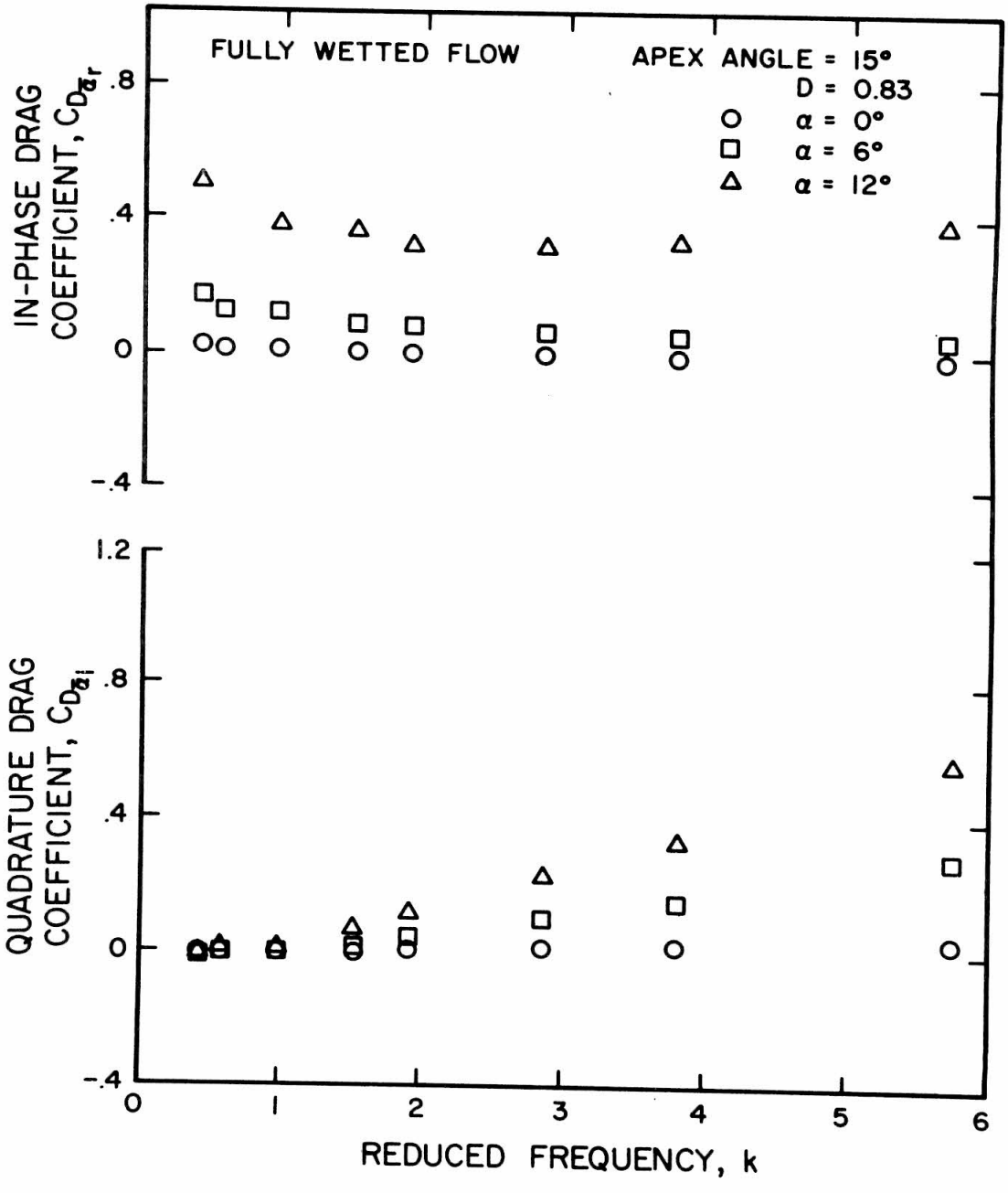

Figure 18 - Unsteady drag coefficients for the 15° delta wing at 0.83 chords submergence.

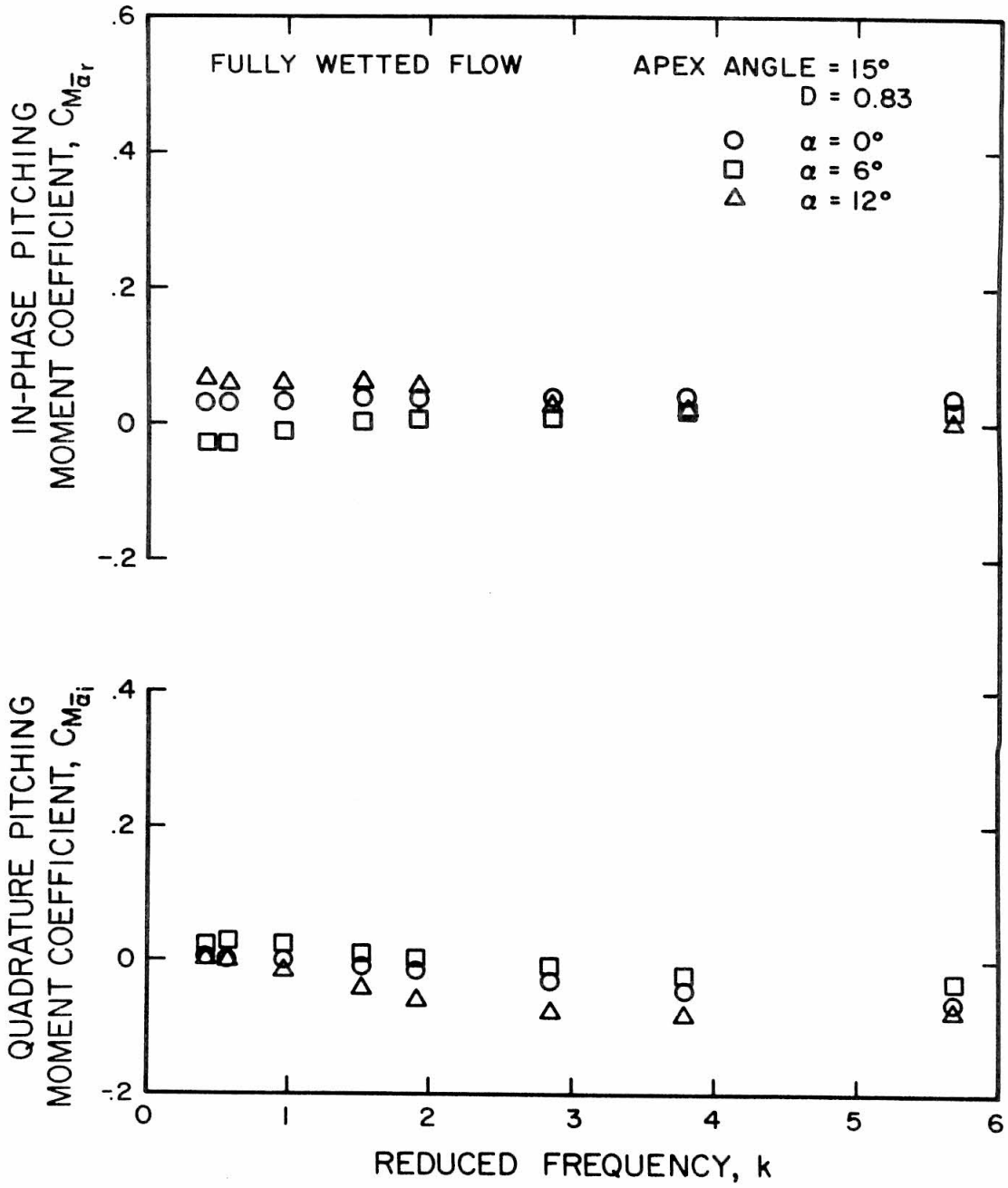

Figure 19 - Unsteady pitching moment coefficients for the 15° delta wing at 0.83 chords submergence.

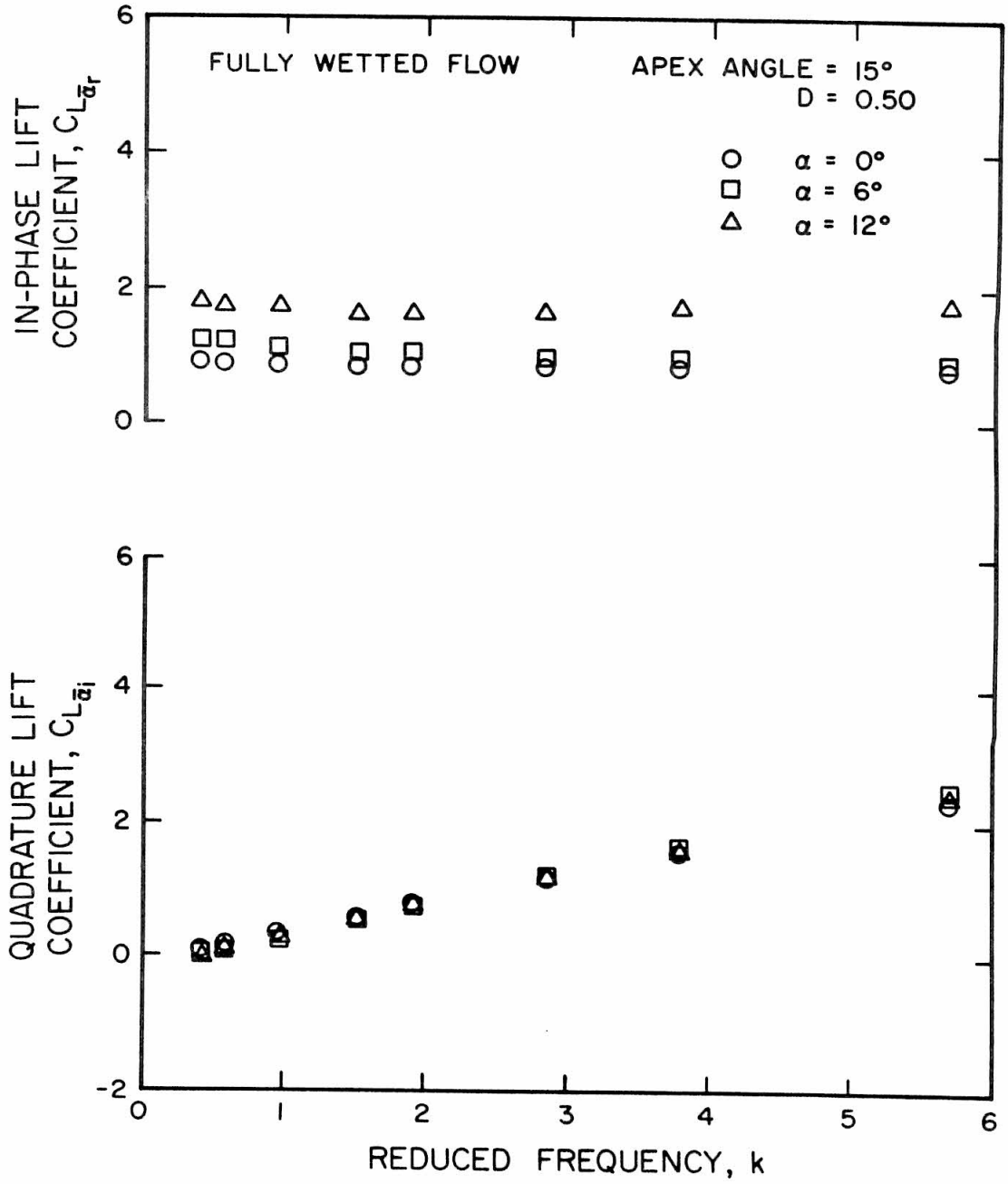

Figure 20 - Unsteady lift coefficients for the 15° delta wing at 0.50 chords submergence.

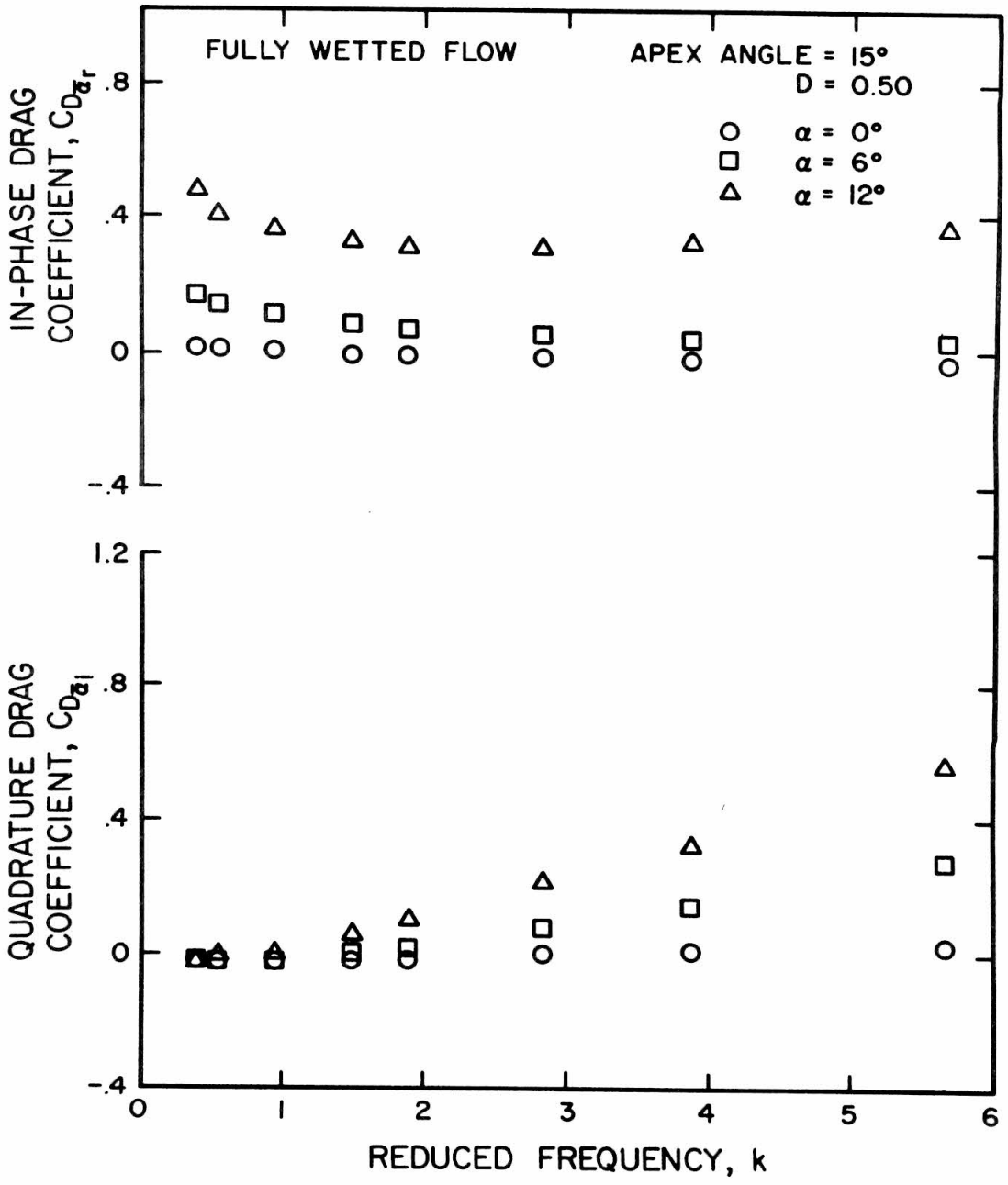

Figure 21 - Unsteady drag coefficients for the 15° delta wing at 0.50 chords submergence.

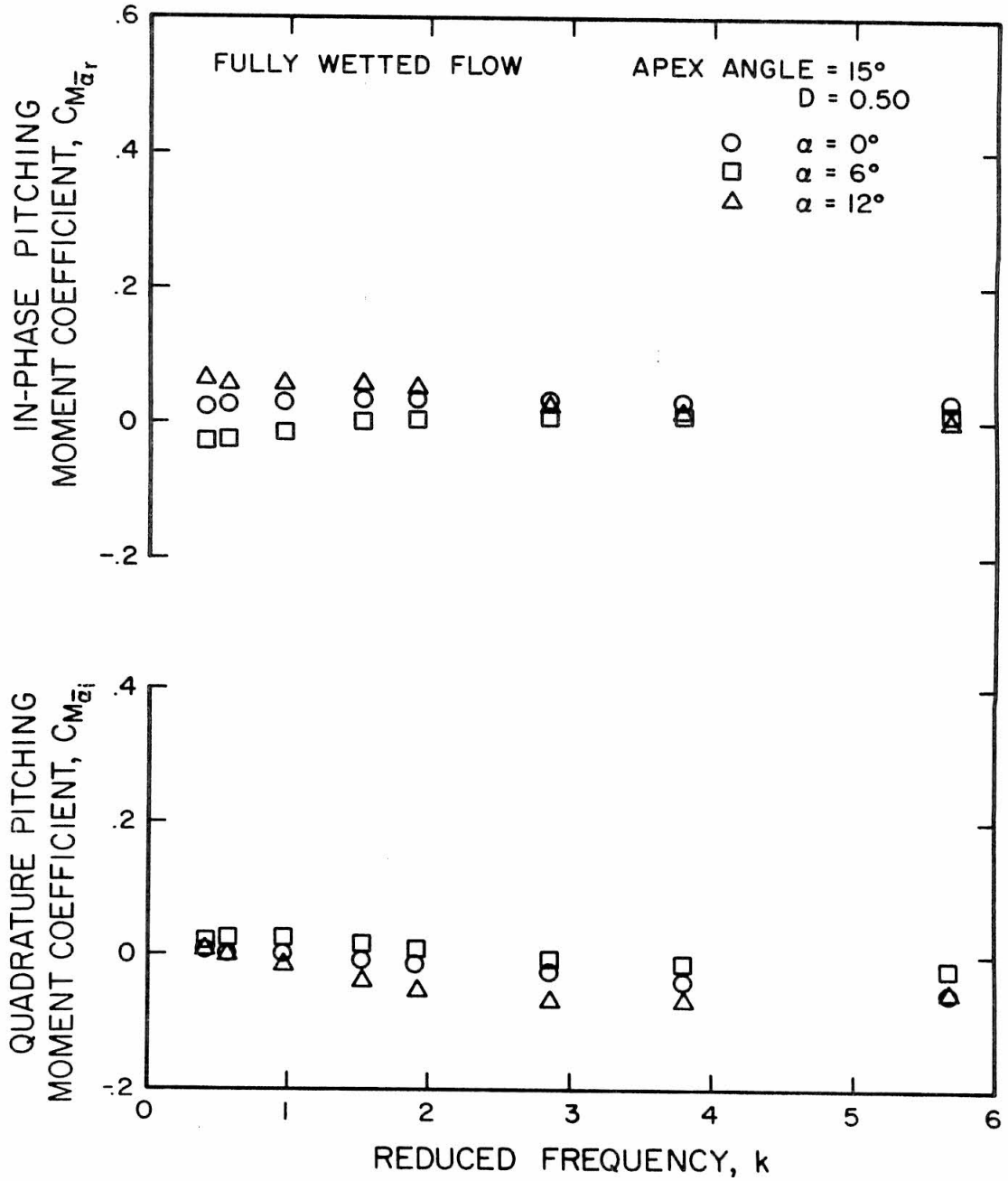

Figure 22 - Unsteady pitching moment coefficients for the 15° delta wing at 0.50 chords submergence.

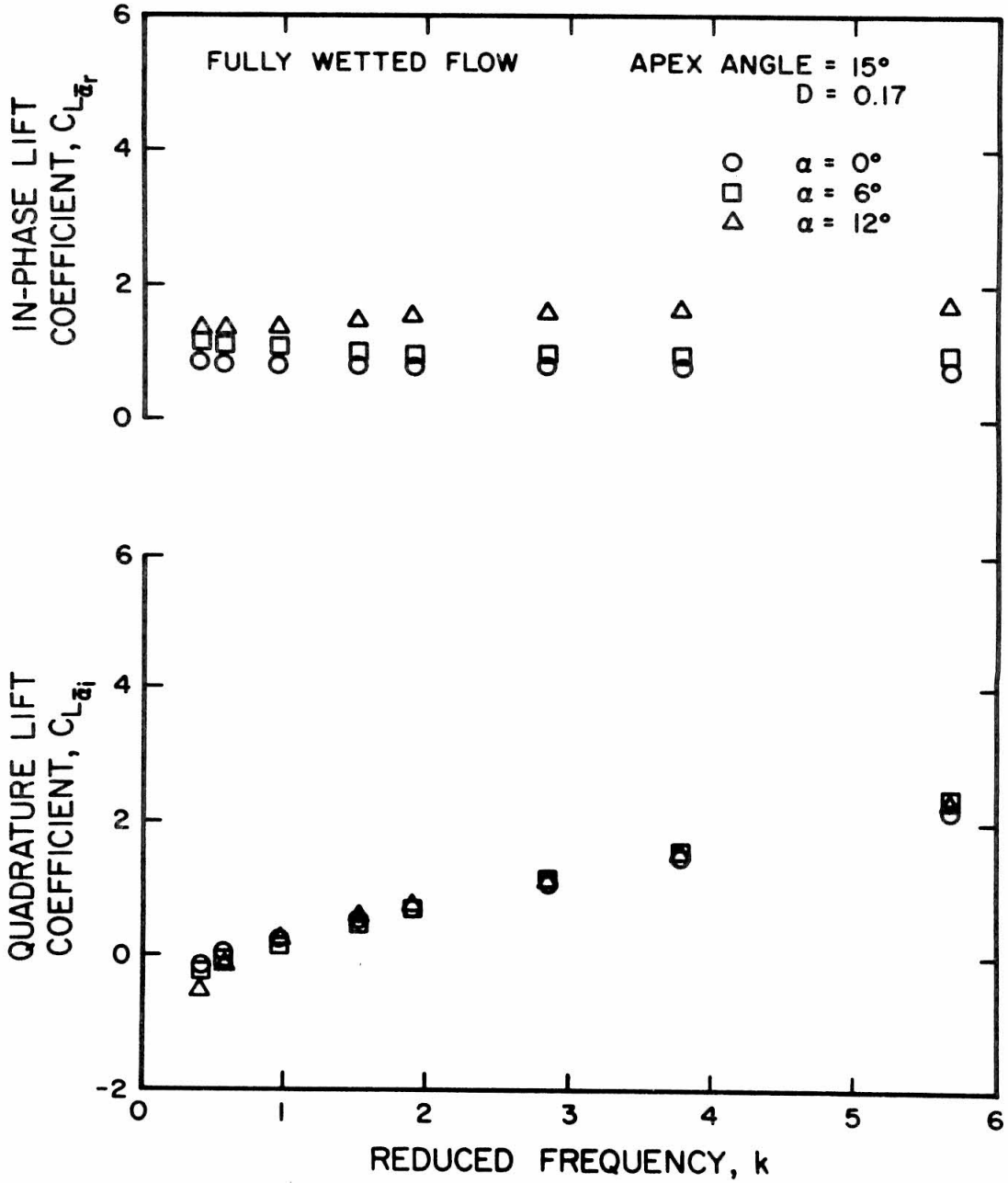

Figure 23 - Unsteady lift coefficients for the 15° delta wing at 0.17 chords submergence.

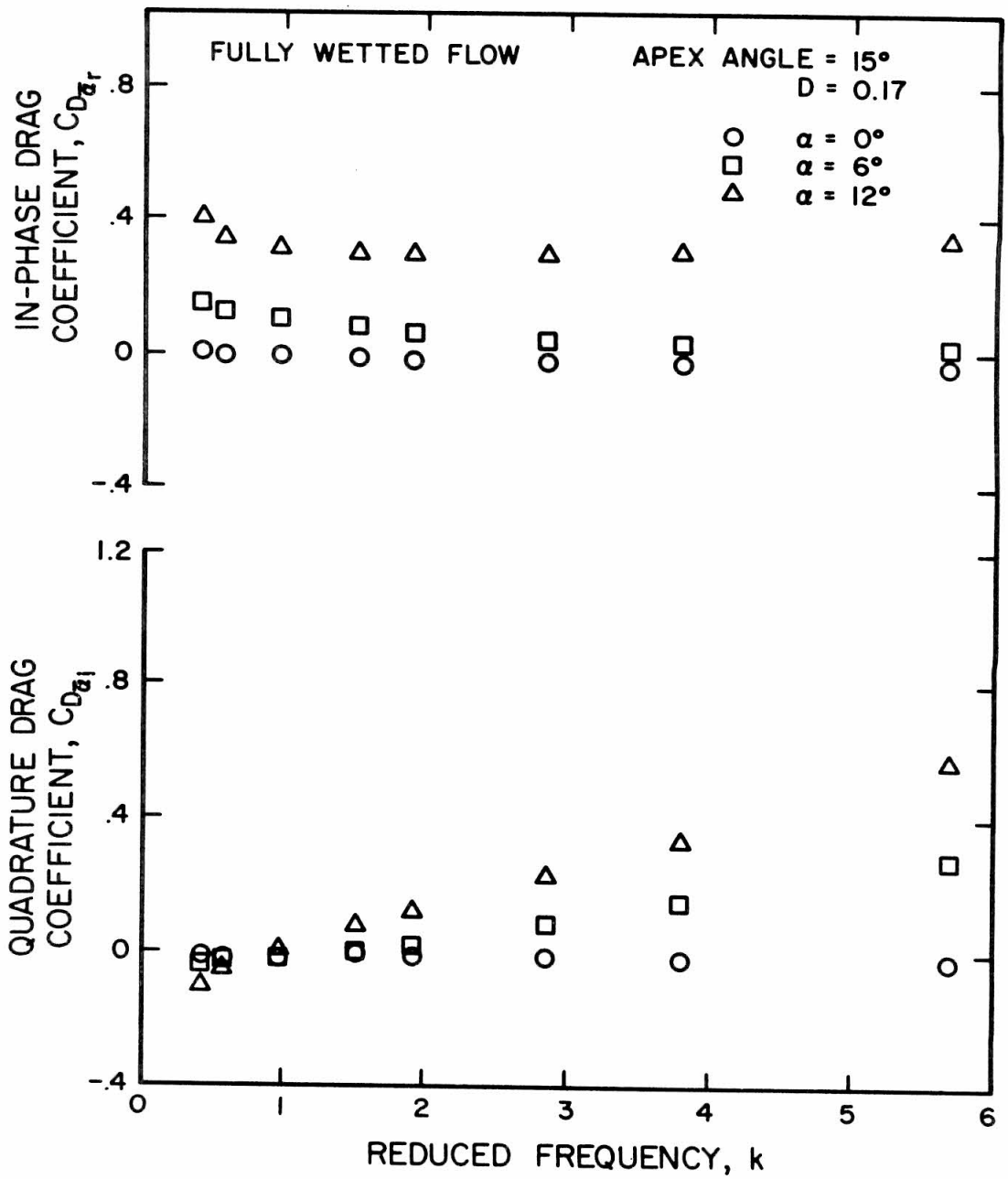

Figure 24 - Unsteady drag coefficients for the 15° delta wing at 0.17 chords submergence.

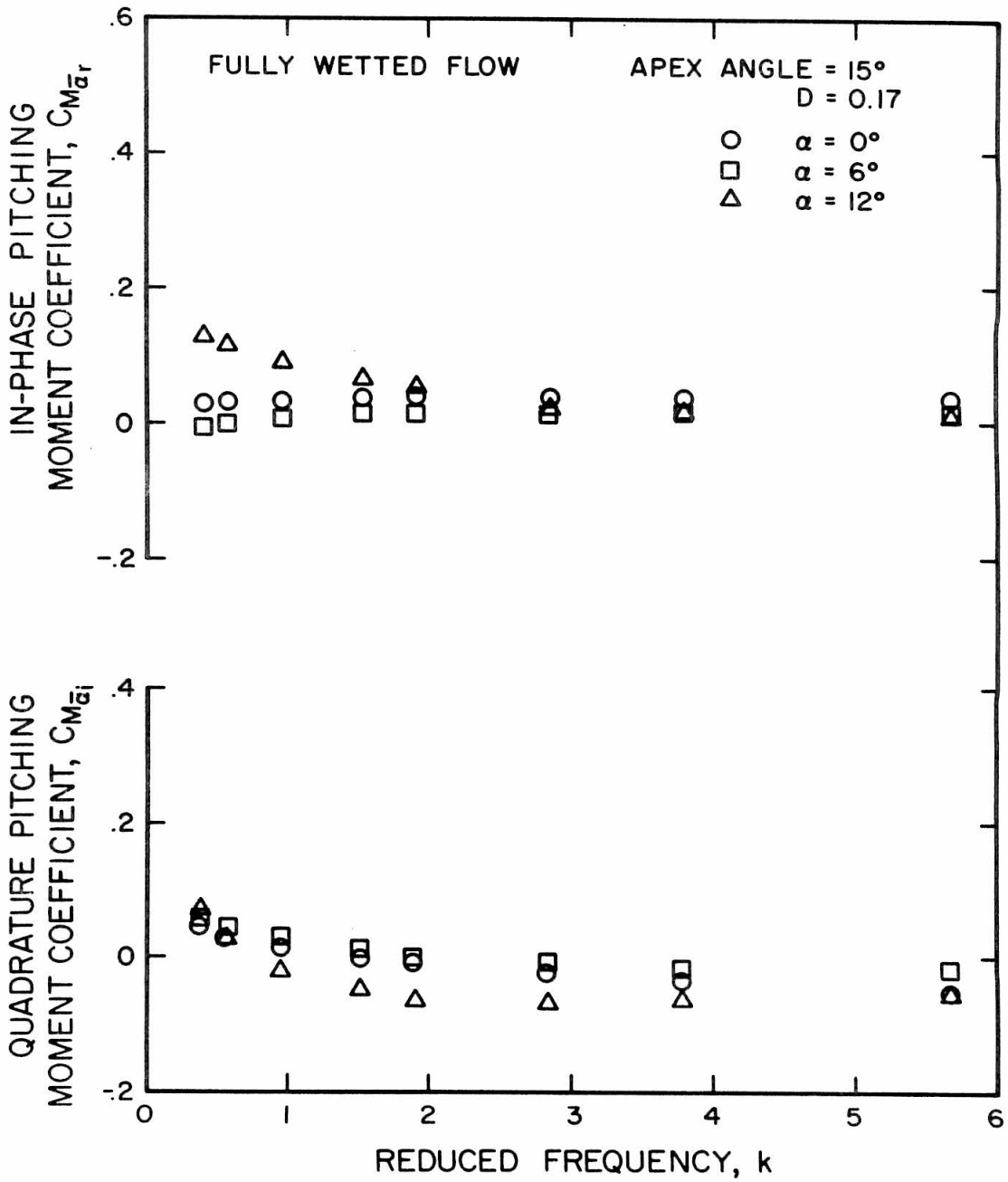

Figure 25 - Unsteady pitching moment coefficients for the 15° delta wing at 0.17 chords submergence.

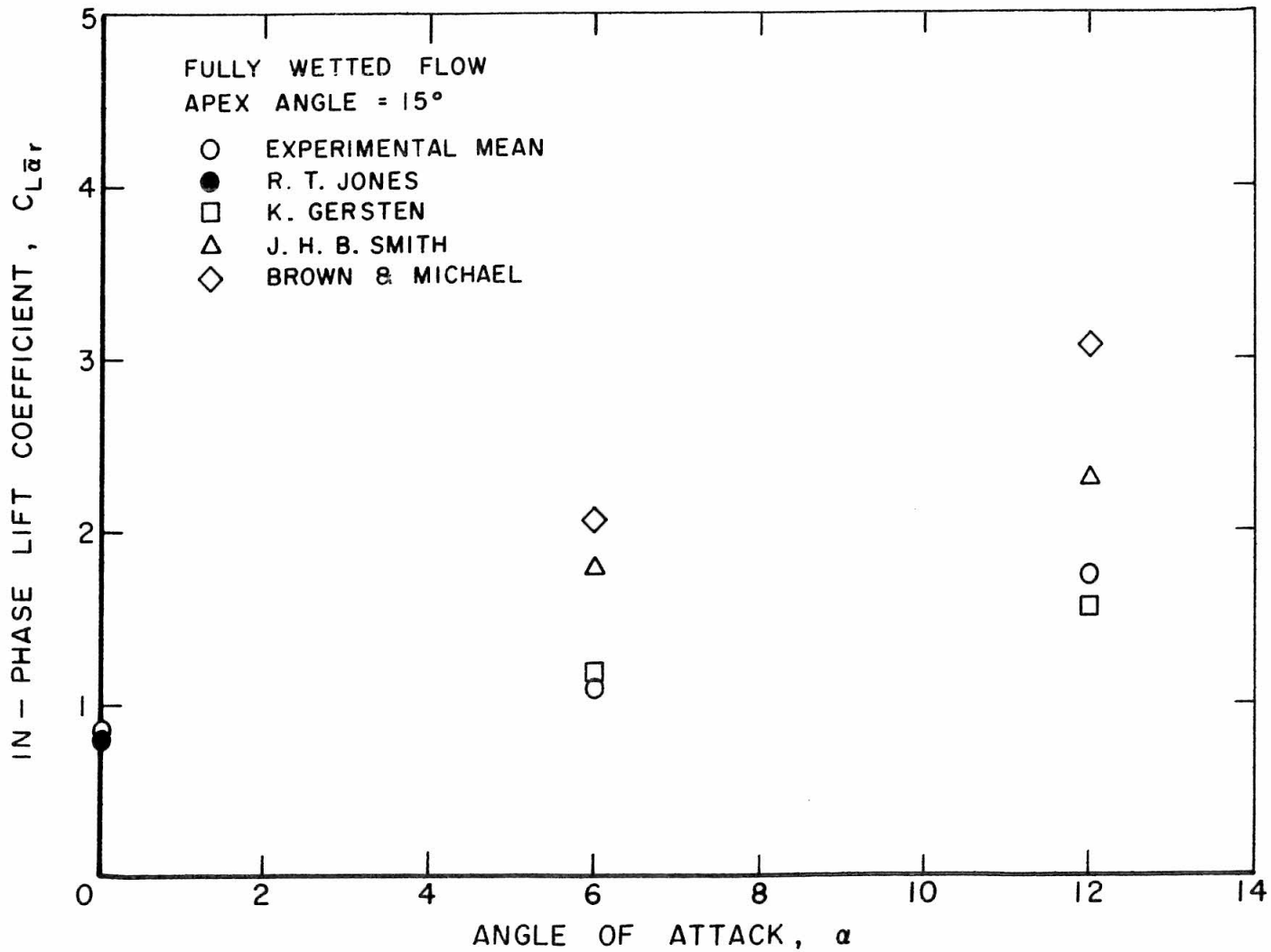

Figure 26 - Summary of steady theories calculated for the 15° delta wing and compared to the experimental in-phase lift coefficients.

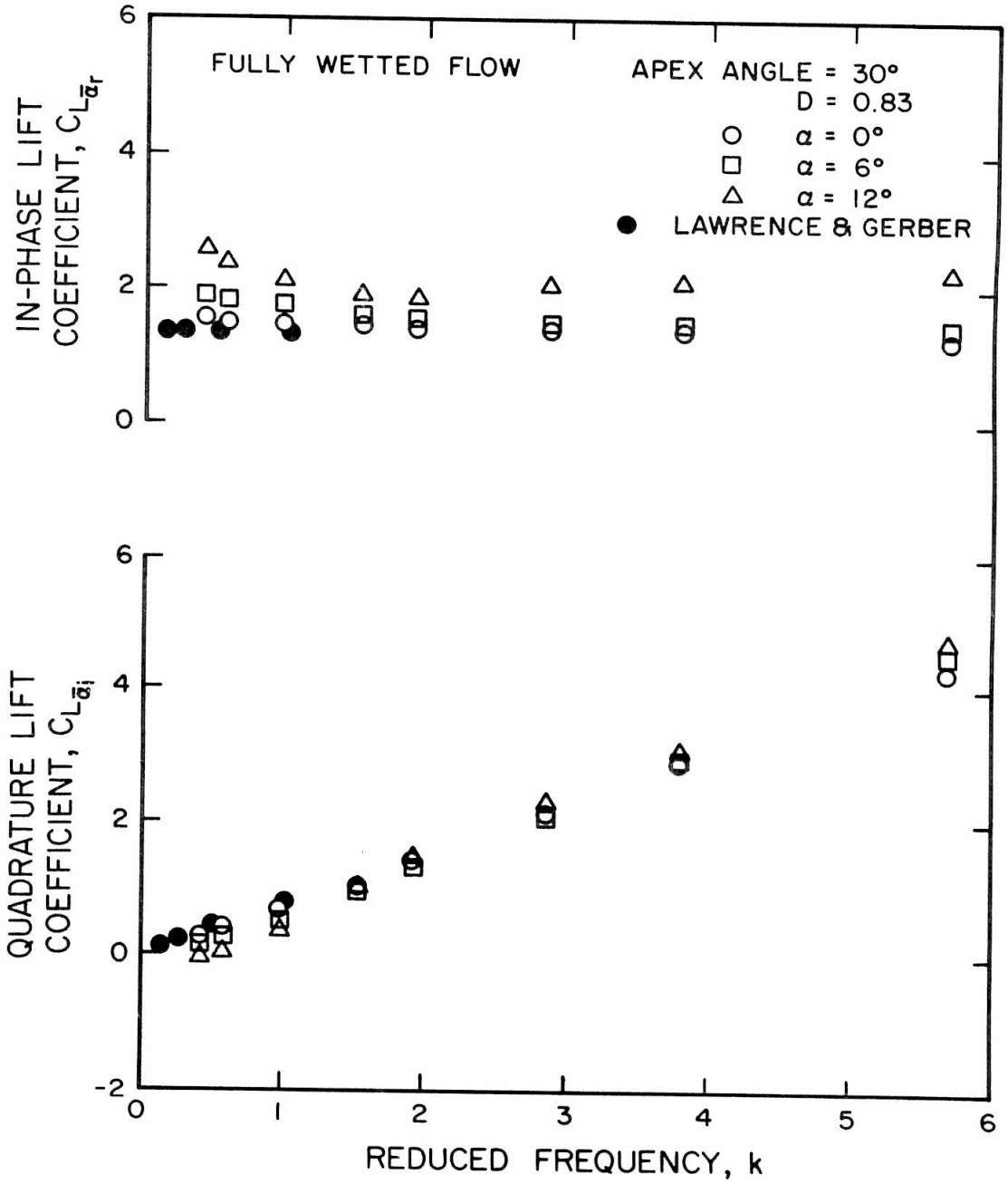

Figure 27 - Unsteady lift coefficients for the 30° delta wing at 0.83 chords submergence.

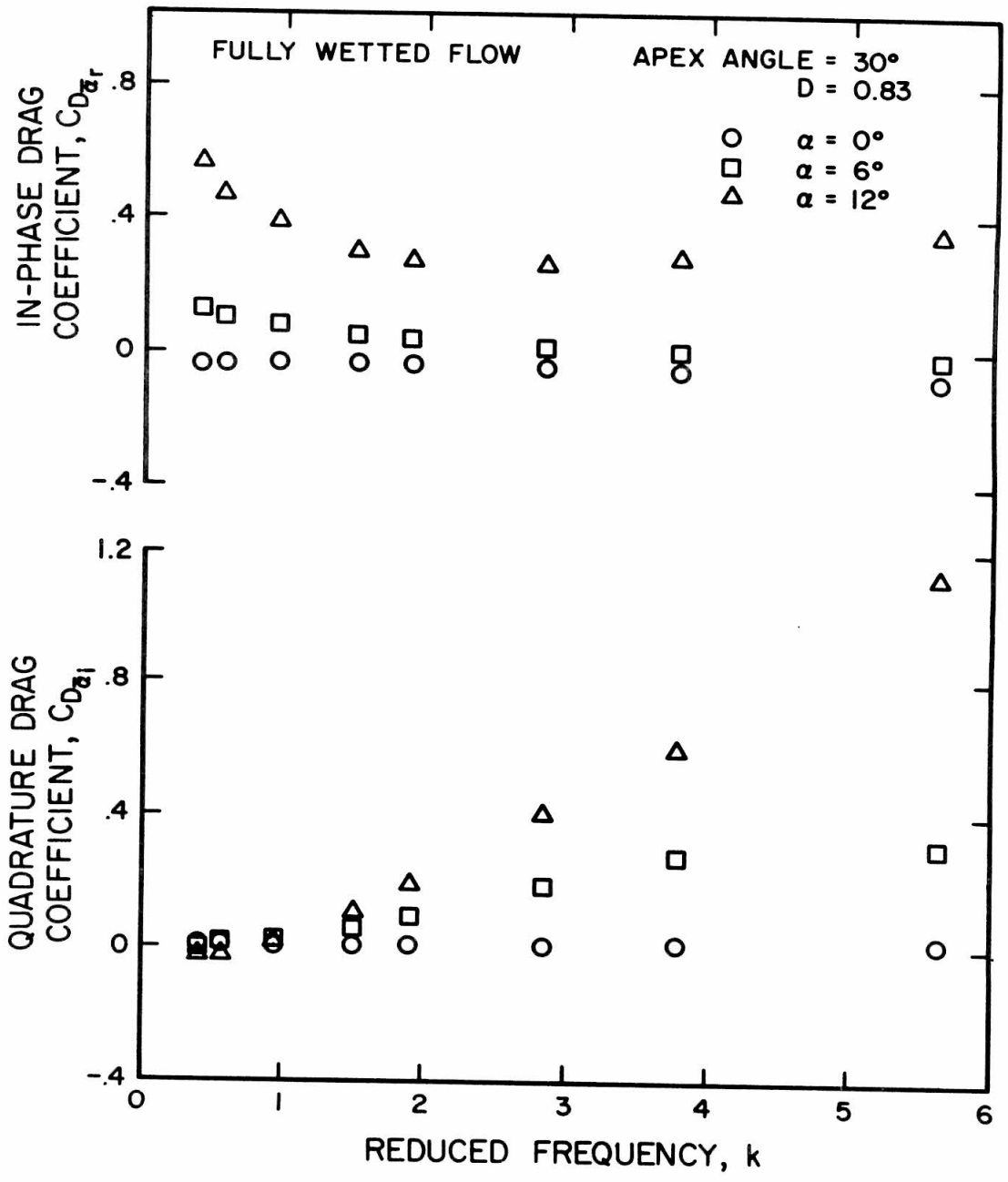

Figure 28 - Unsteady drag coefficients for the 30° delta wing at 0.83 chords submergence.

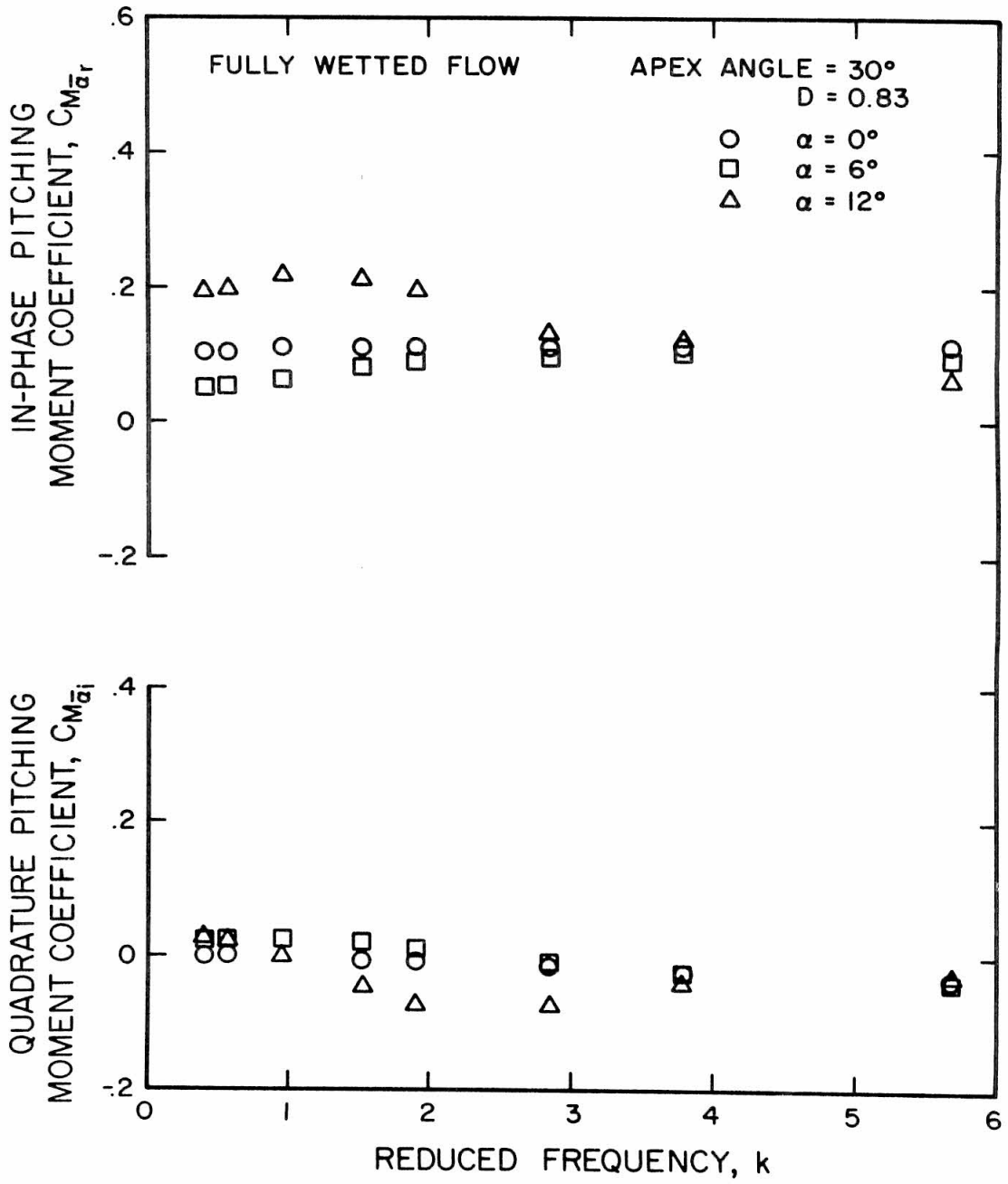

Figure 29 - Unsteady pitching moment coefficients for the 30° delta wing at 0.83 chords submergence.

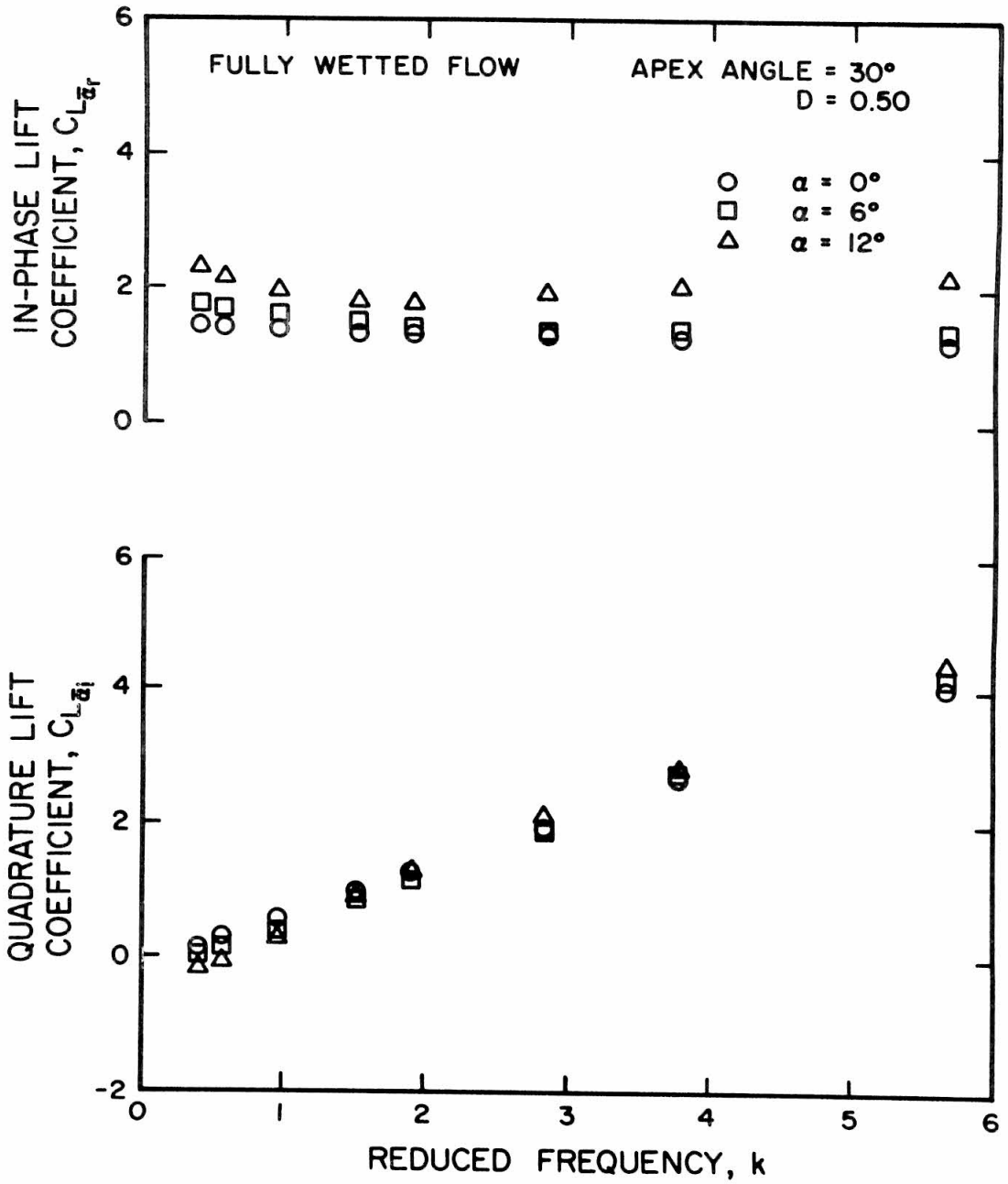

Figure 30 - Unsteady lift coefficients for the 30° delta wing at 0.50 chords submergence.

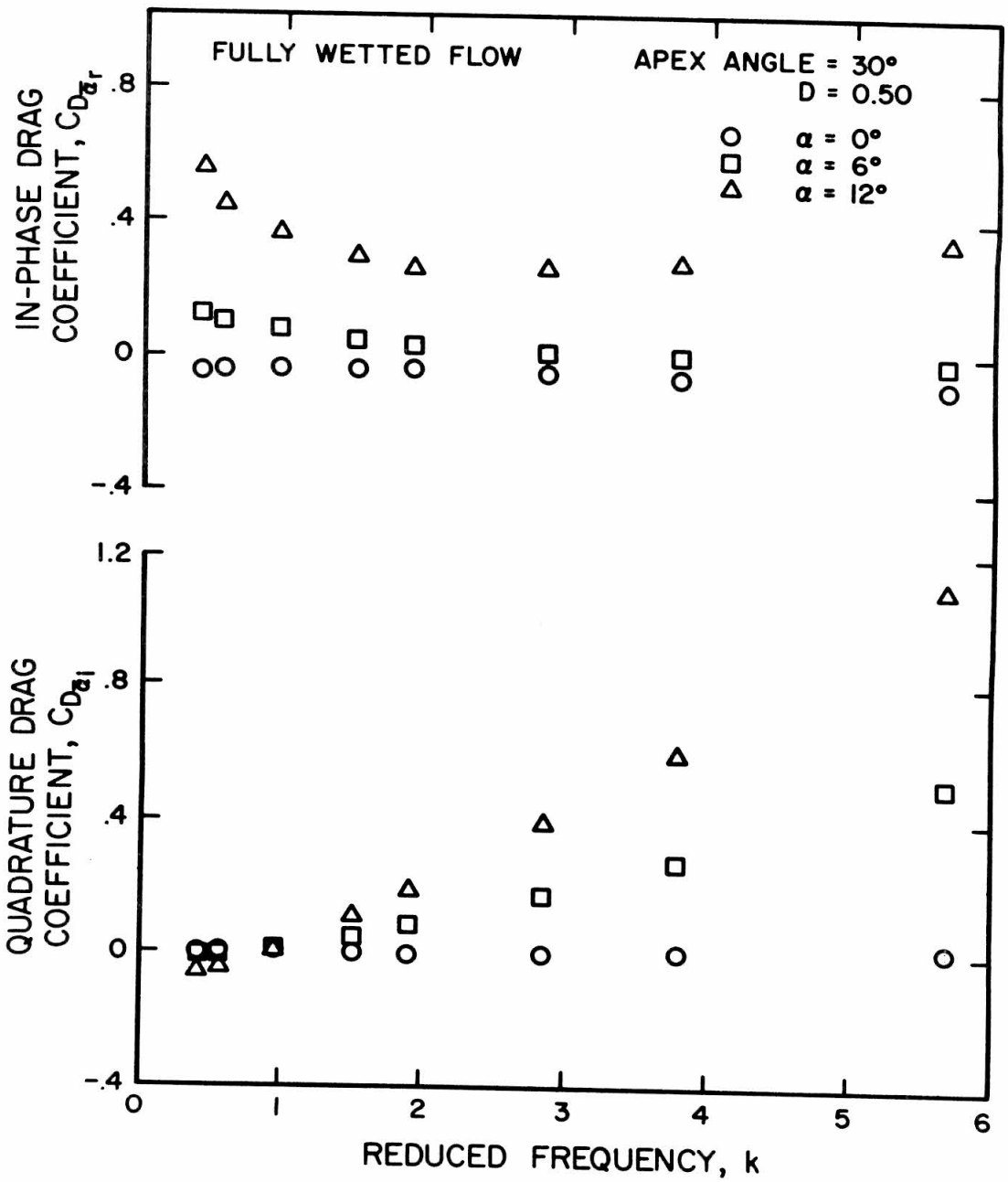

Figure 31 - Unsteady drag coefficients for the 30° delta wing at 0.50 chords submergence.

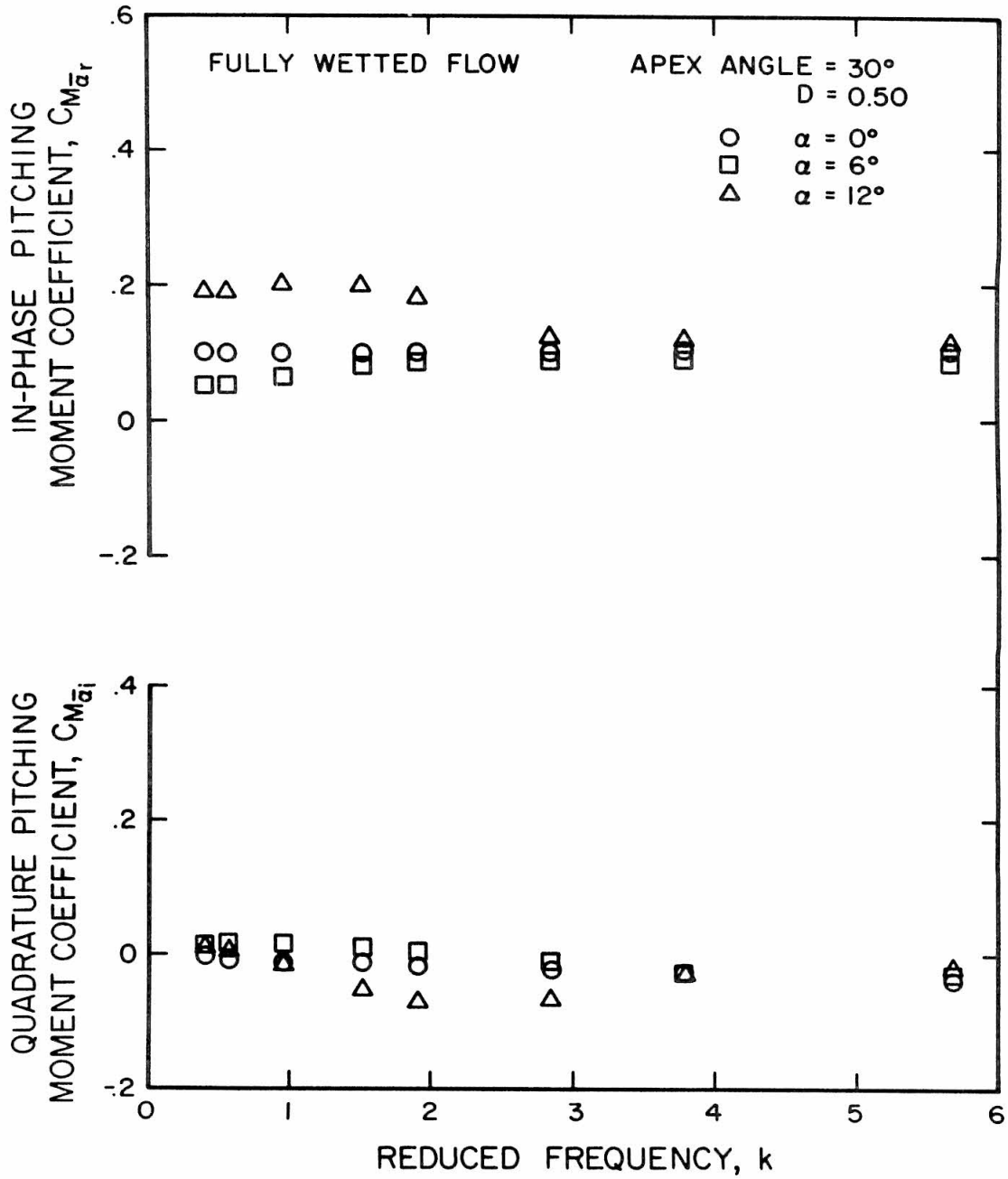

Figure 32 - Unsteady pitching moment coefficients for the 30° delta wing at 0.50 chords submergence.

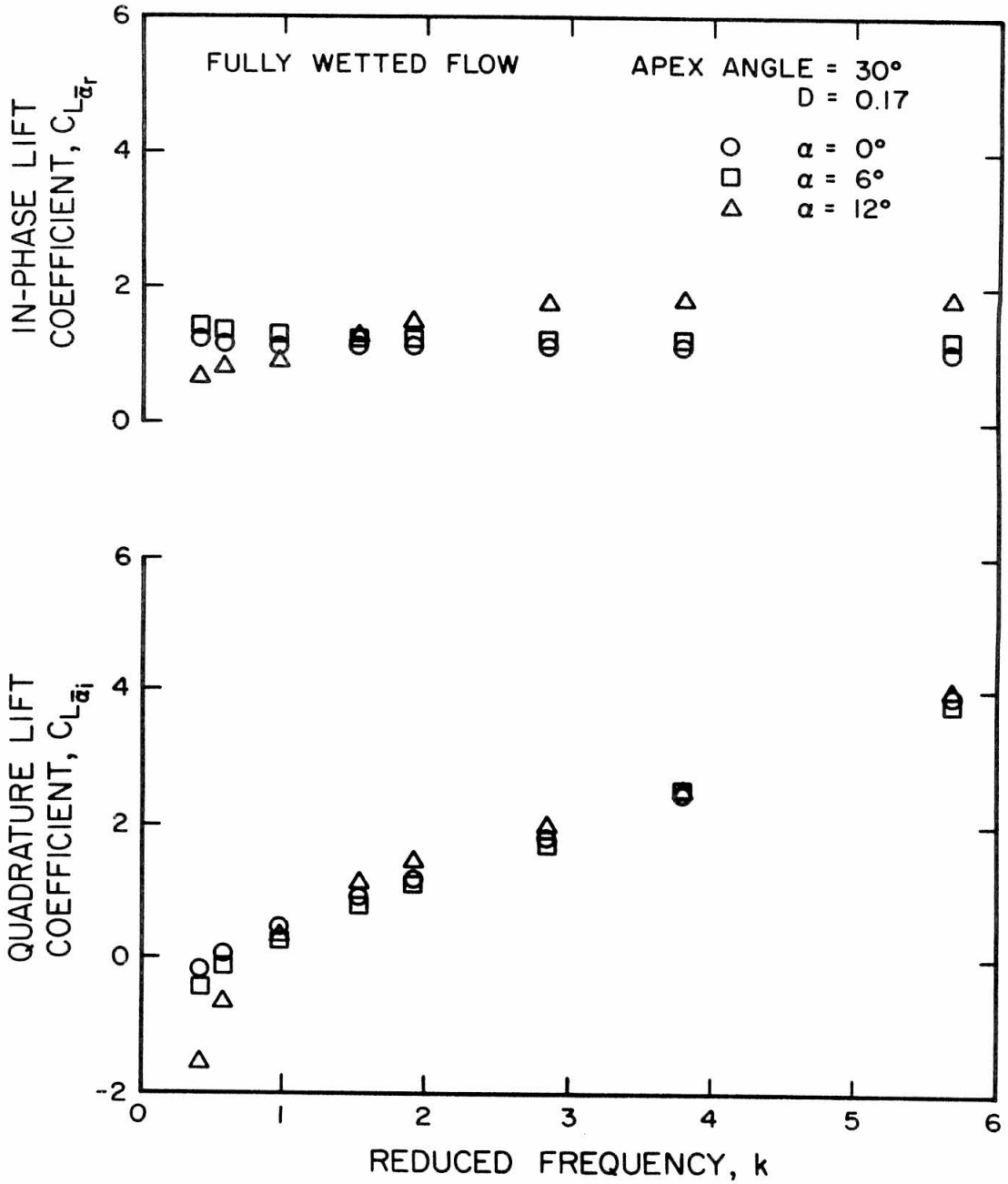

Figure 33 - Unsteady lift coefficients for the 30° delta wing at 0.17 chords submergence.

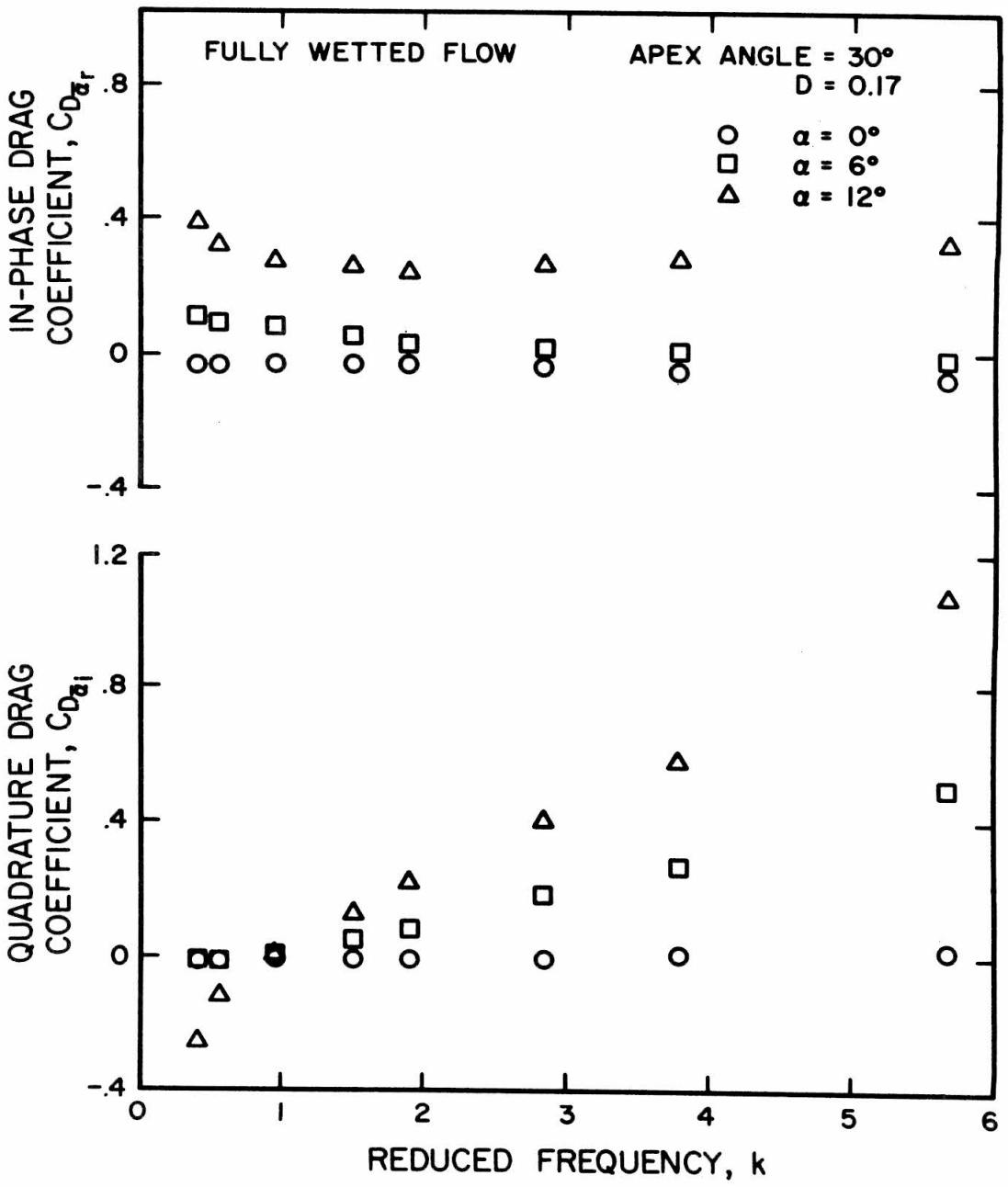

Figure 34 - Unsteady drag coefficients for the 30° delta wing at 0.17 chords submergence.

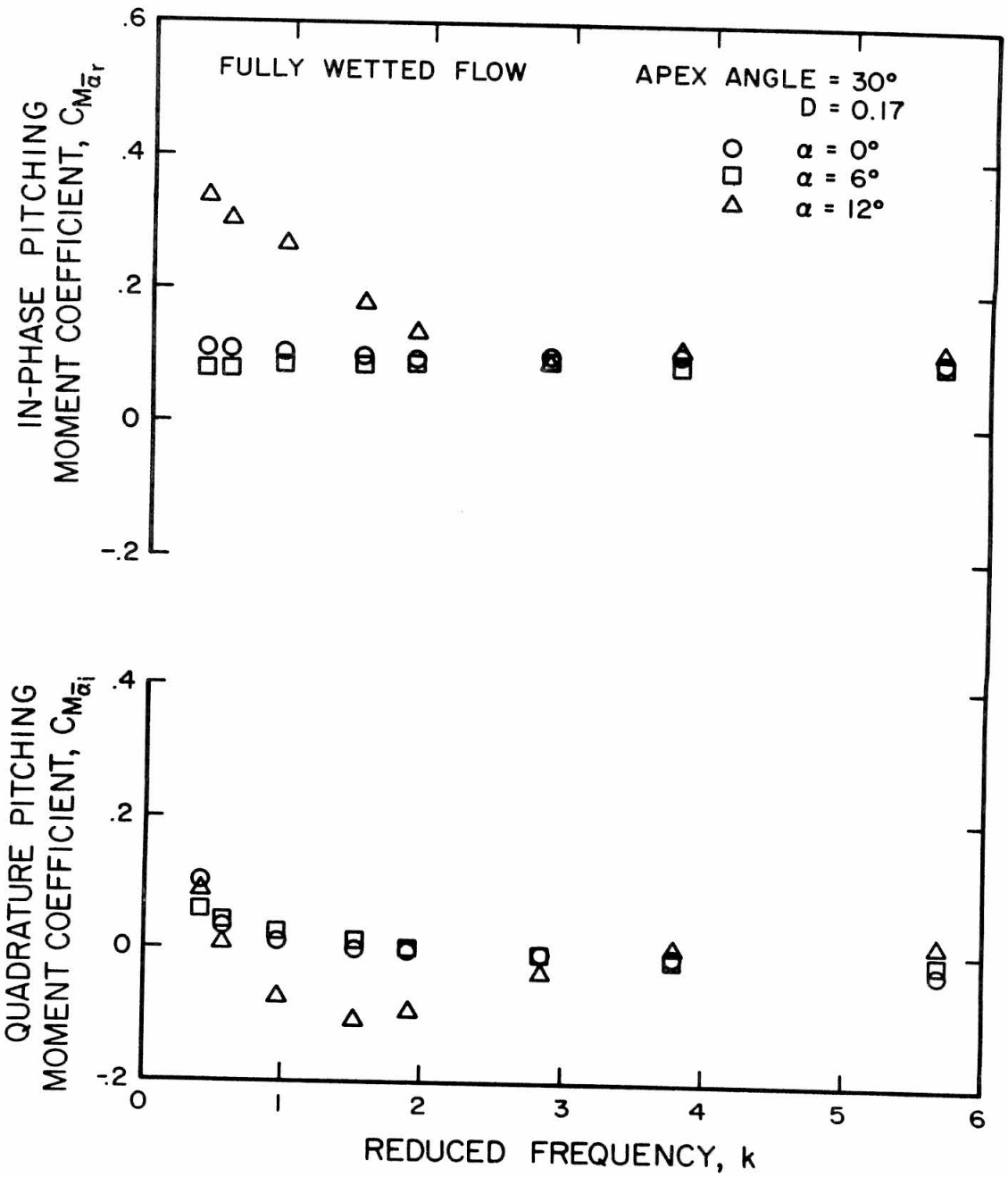

Figure 35 - Unsteady pitching moment coefficients for the 30° delta wing at 0.17 chords submergence.

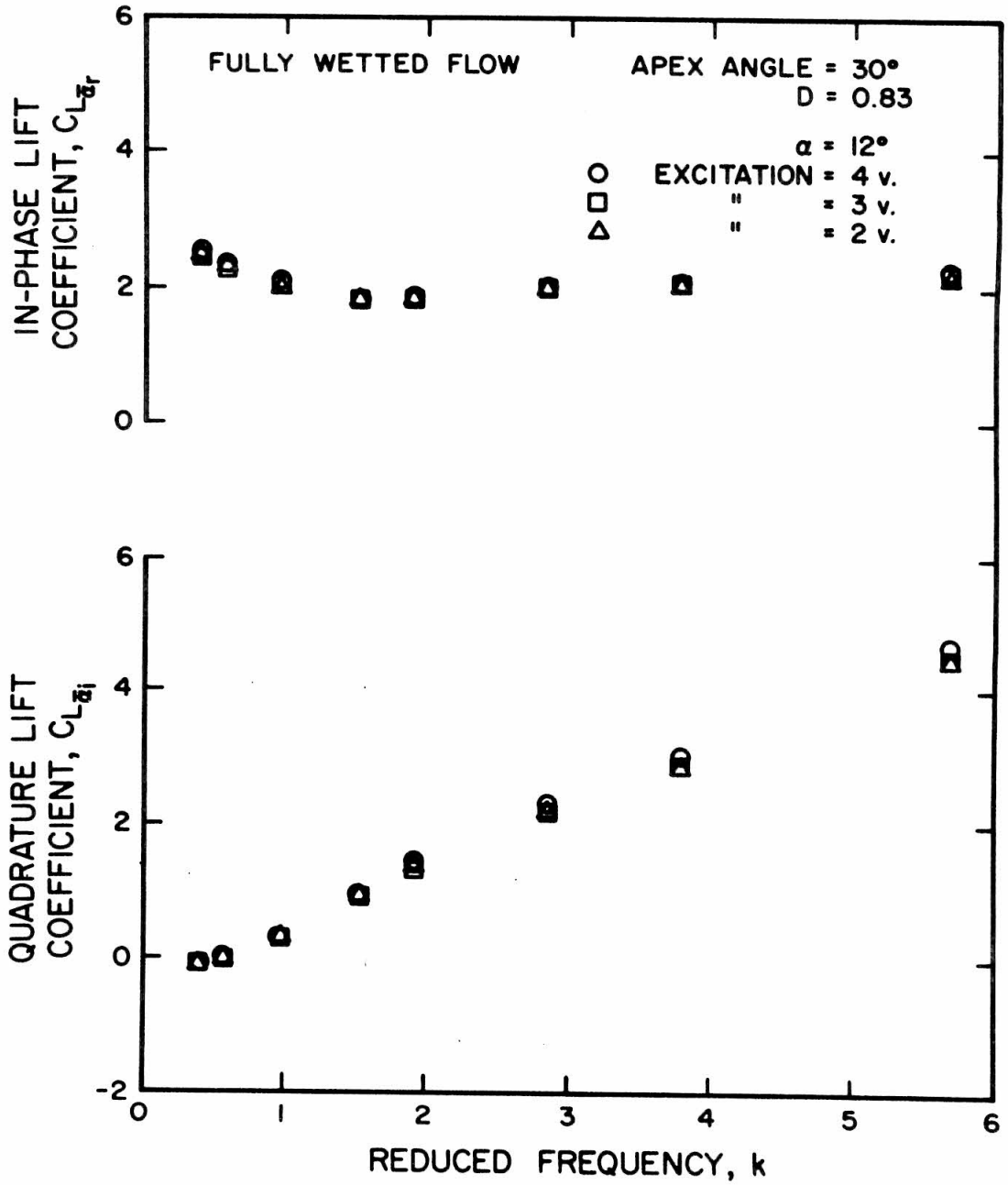

Figure 36 - Unsteady lift coefficients showing the effect of heaving amplitude.

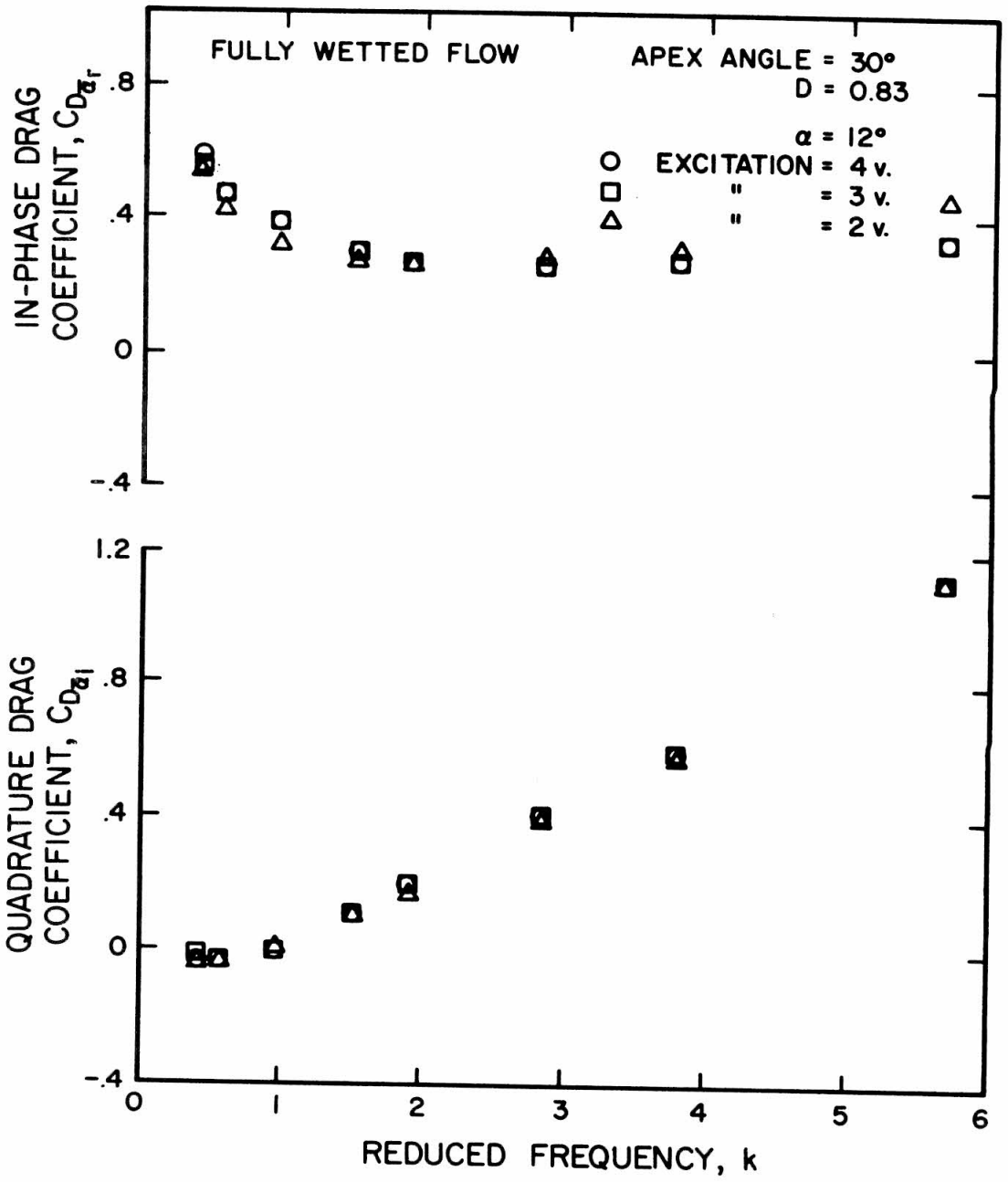

Figure 37 - Unsteady drag coefficients showing the effect of heaving amplitude.

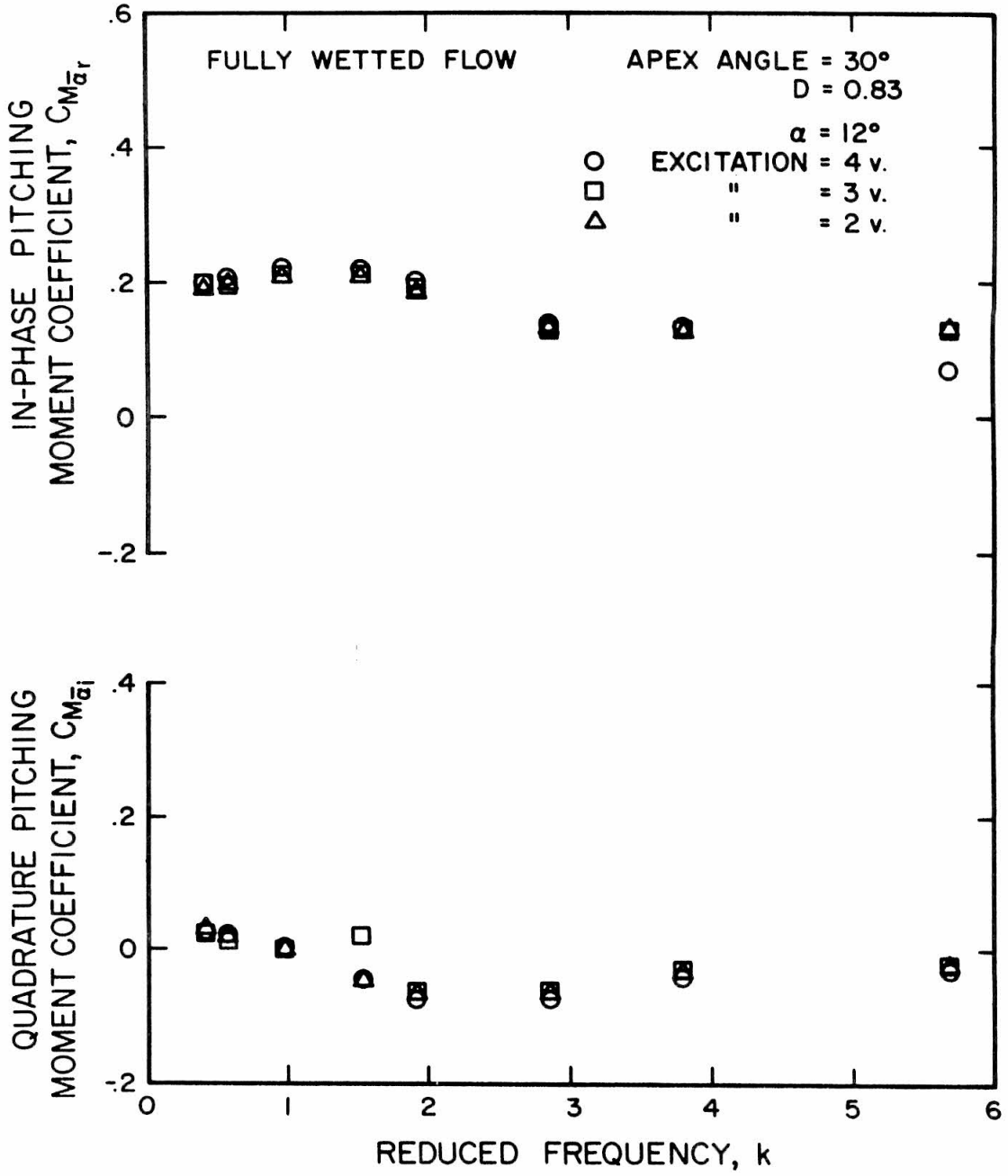

Figure 38 - Unsteady pitching moment coefficients showing the effect of heaving amplitude.

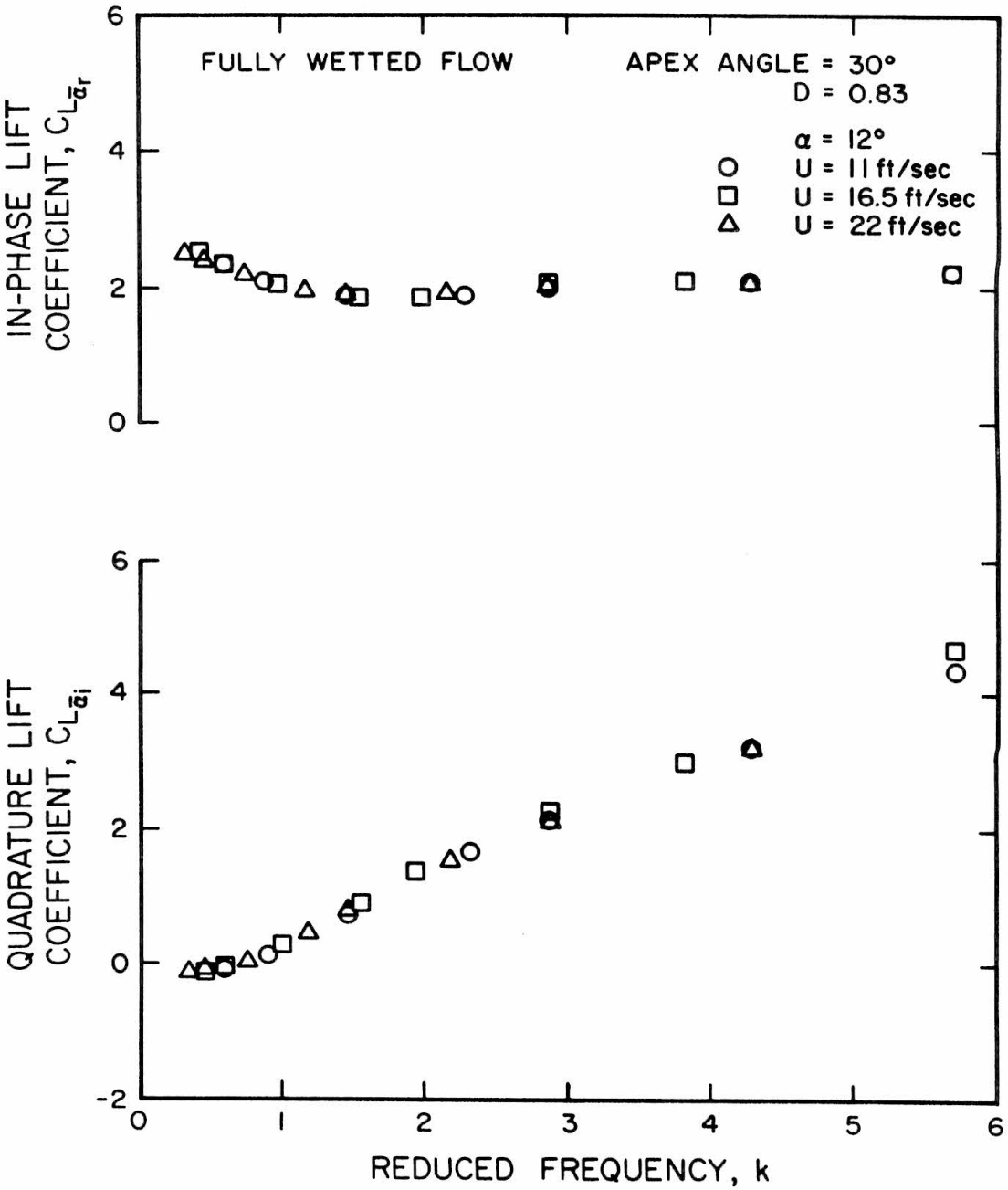

Figure 39 - Unsteady lift coefficients showing the effect of free stream velocity.

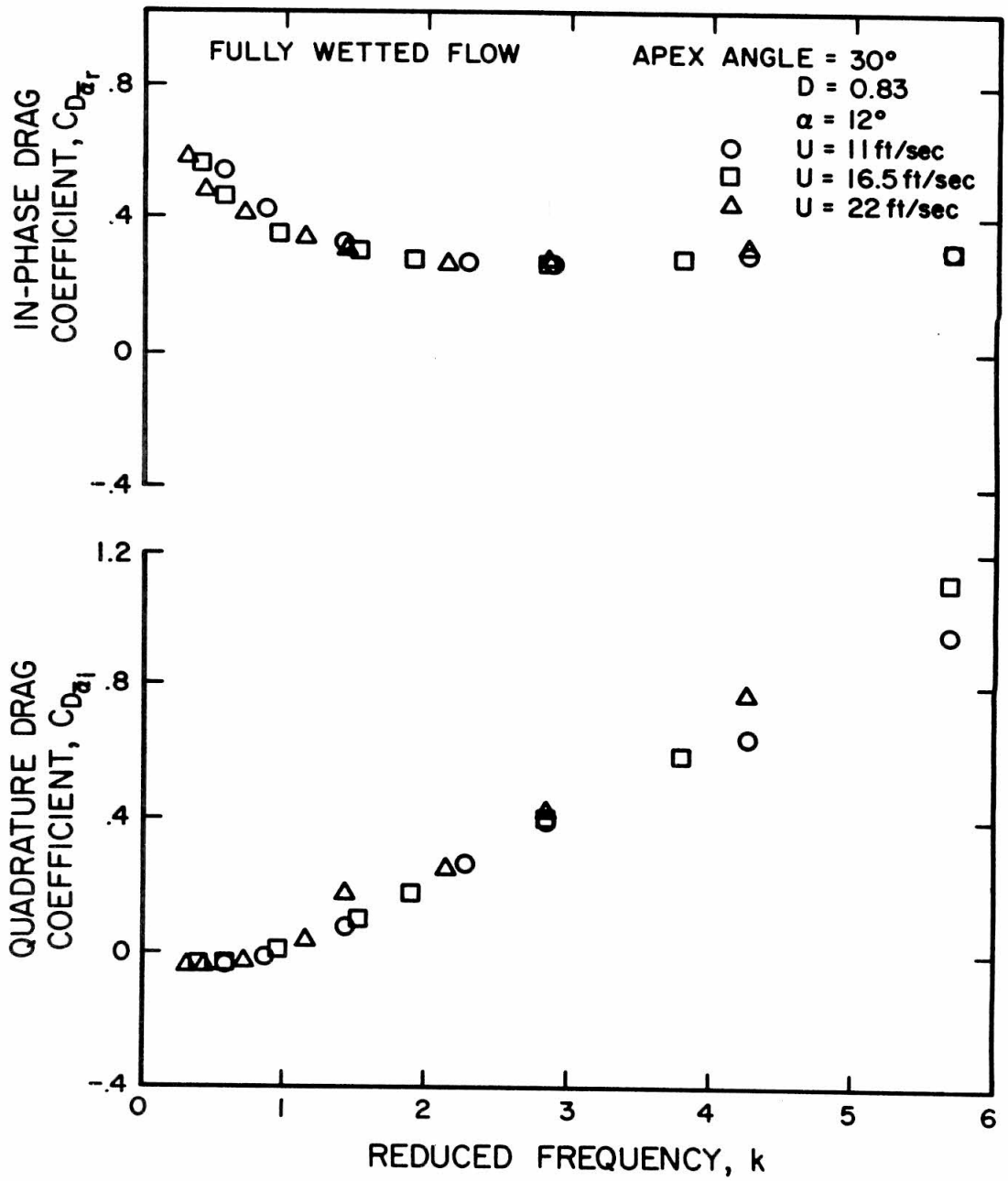

Figure 40 - Unsteady drag coefficients showing the effect of free stream velocity.

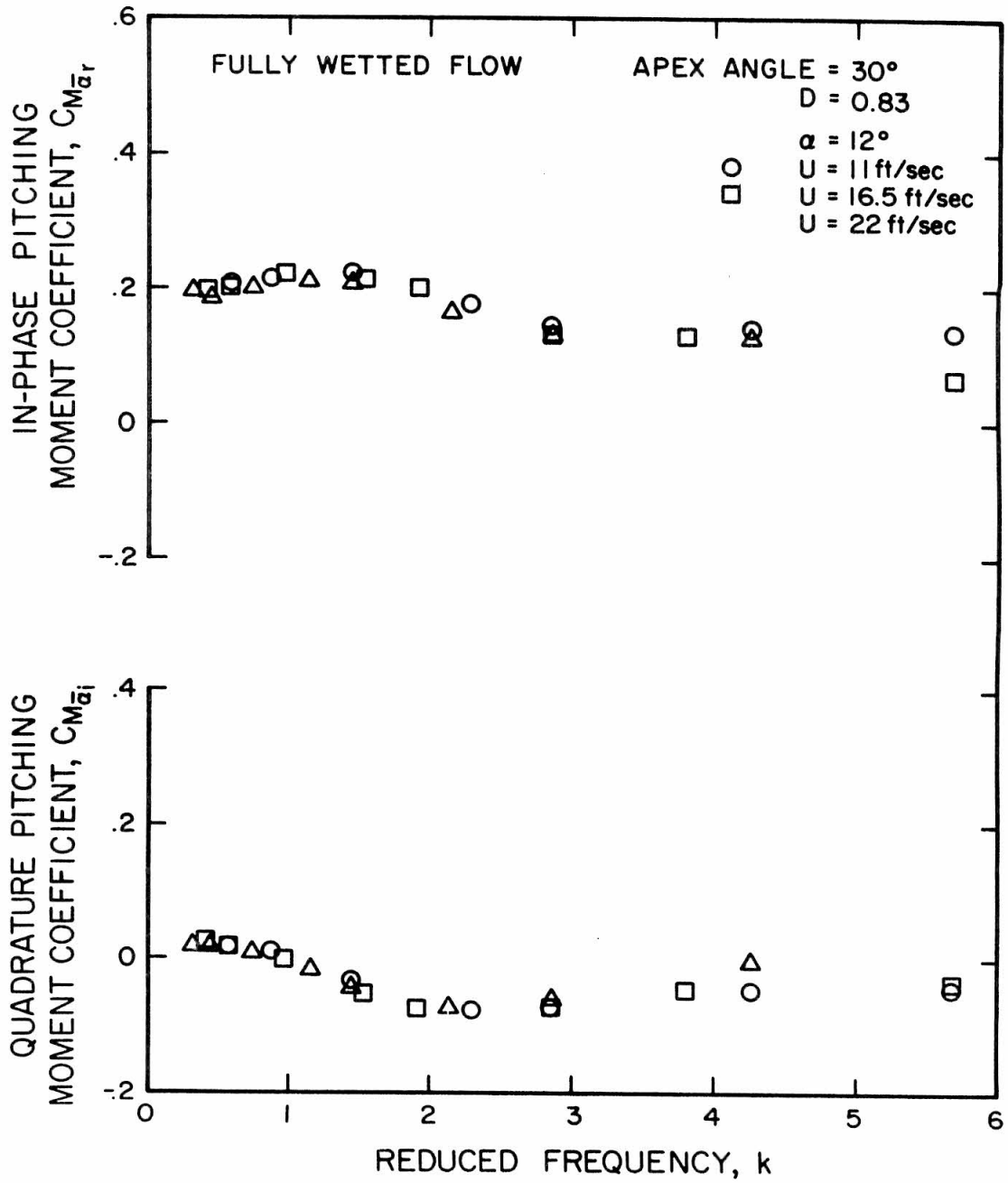

Figure 41 - Unsteady pitching moment coefficients showing the effect of free stream velocity.

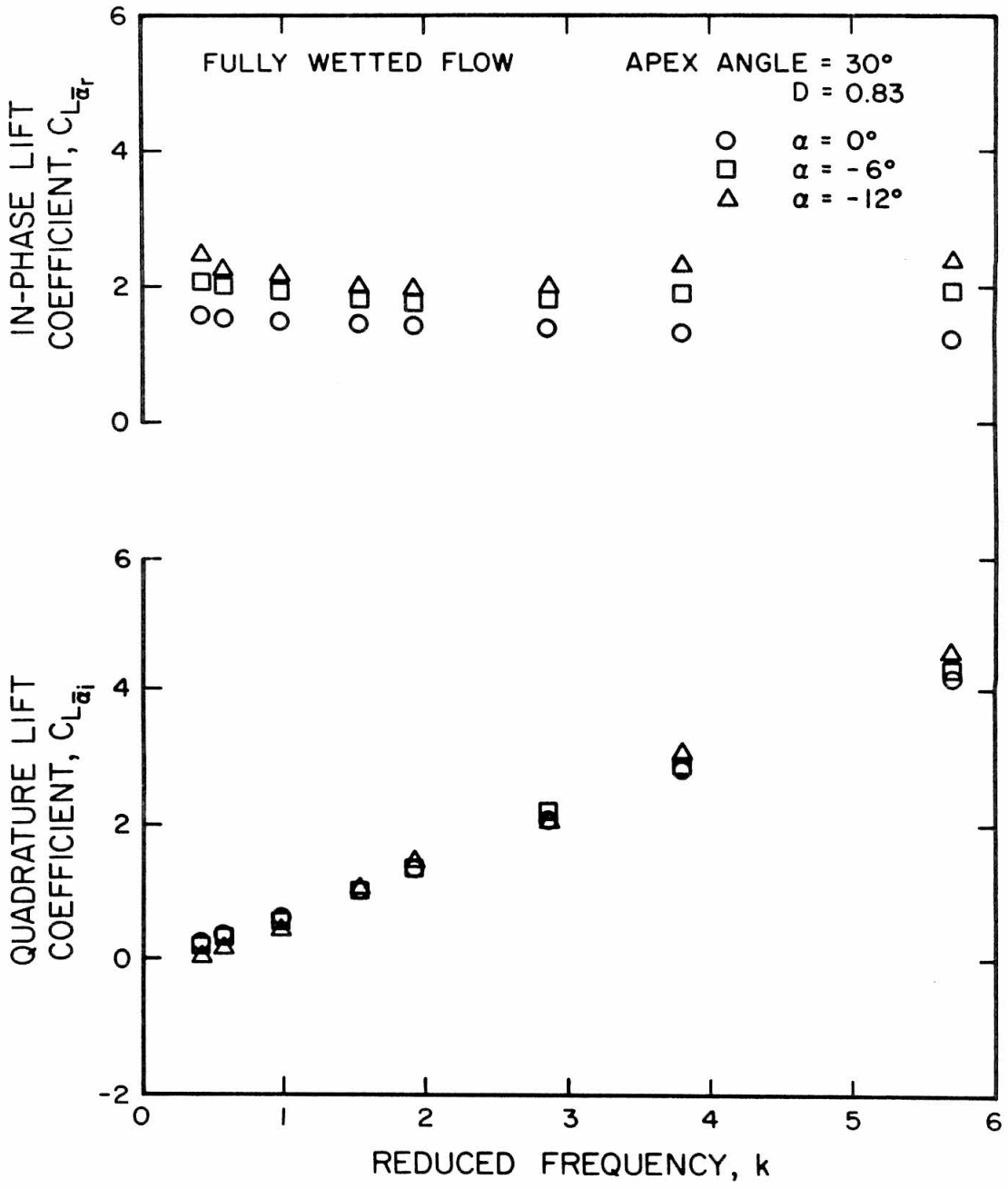

Figure 42 - Unsteady lift coefficients for negative angles of attack.

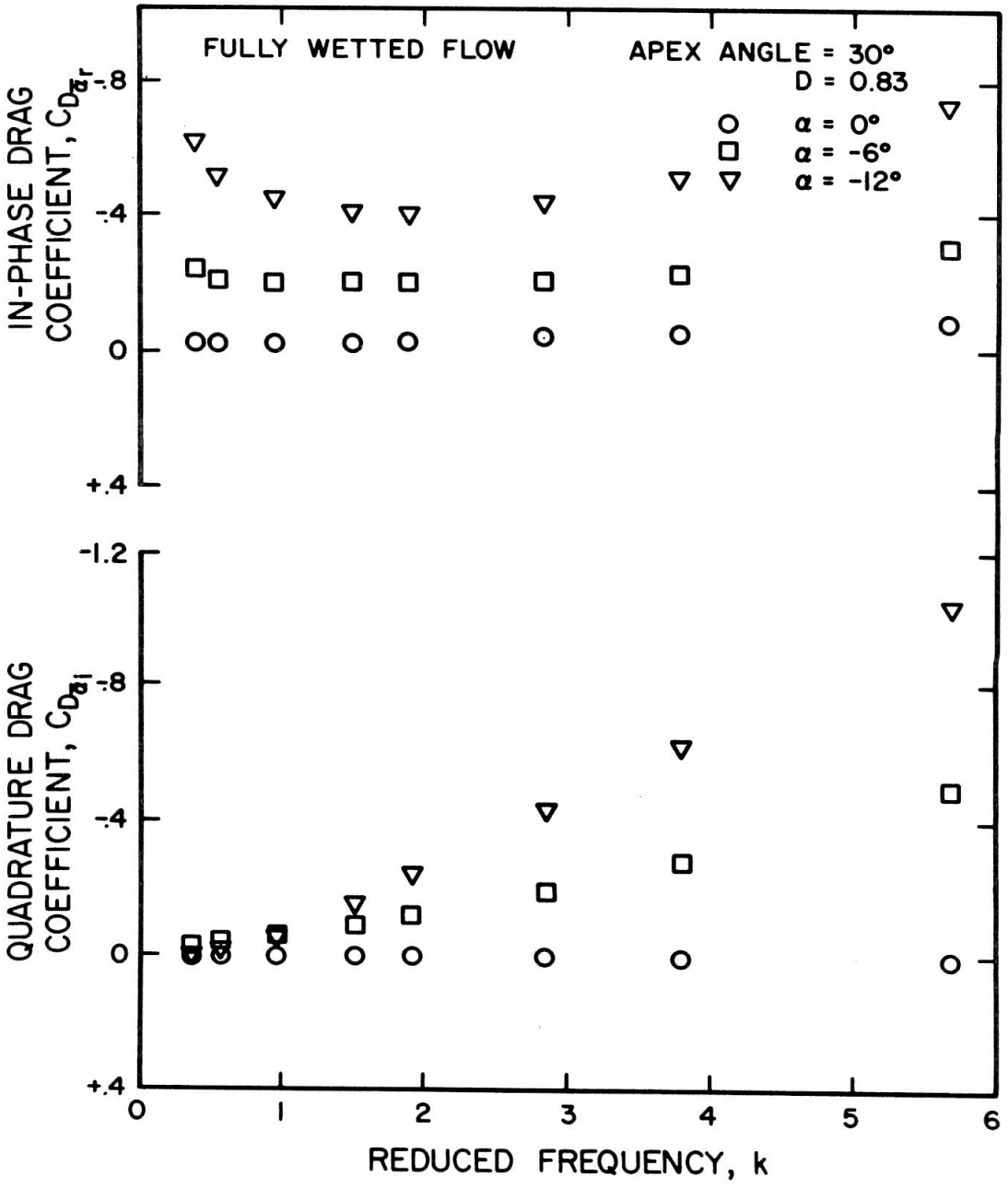

Figure 43 - Unsteady drag coefficients for negative angles of attack.

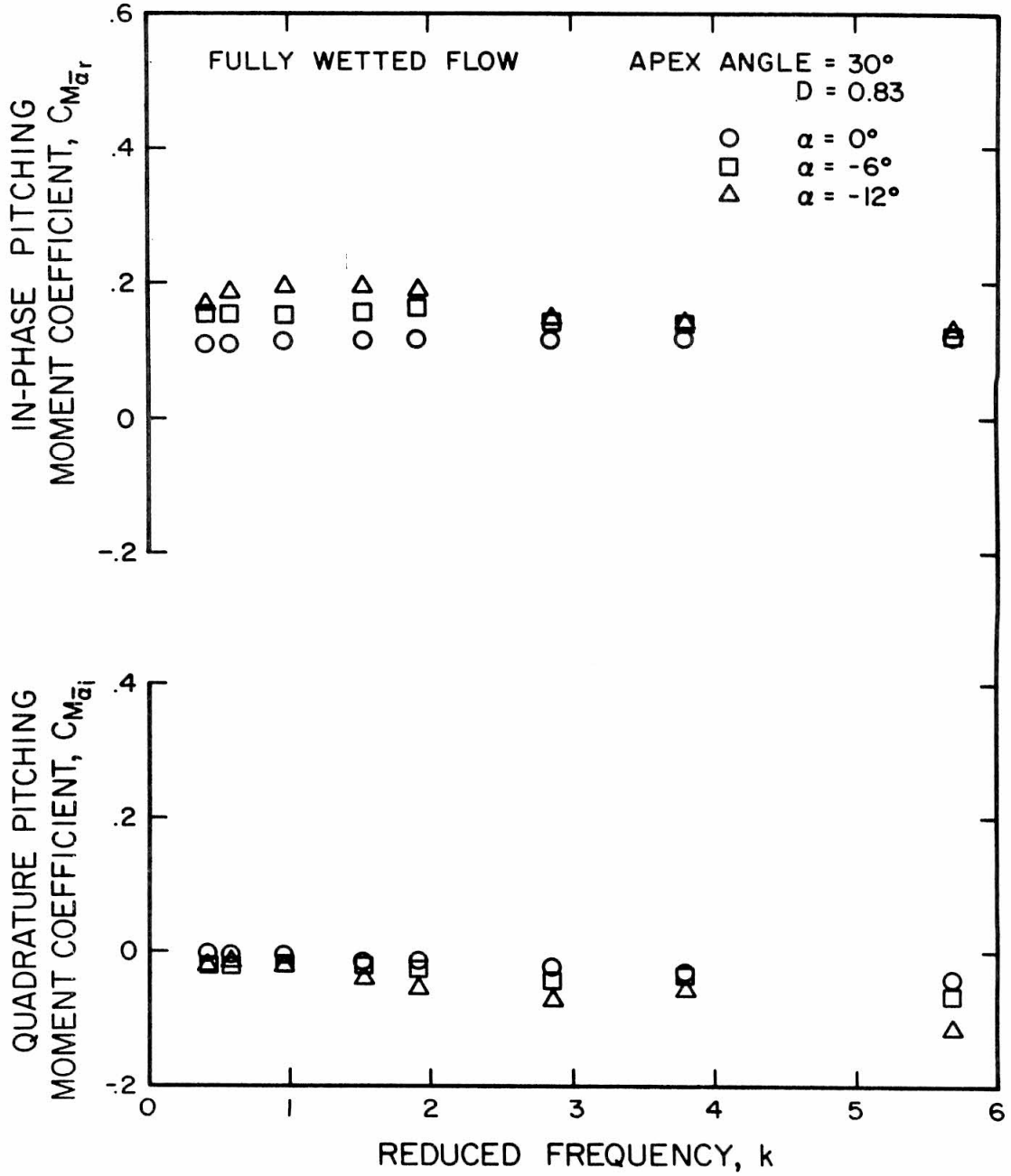

Figure 44 - Unsteady pitching moment coefficients for negative angles of attack.

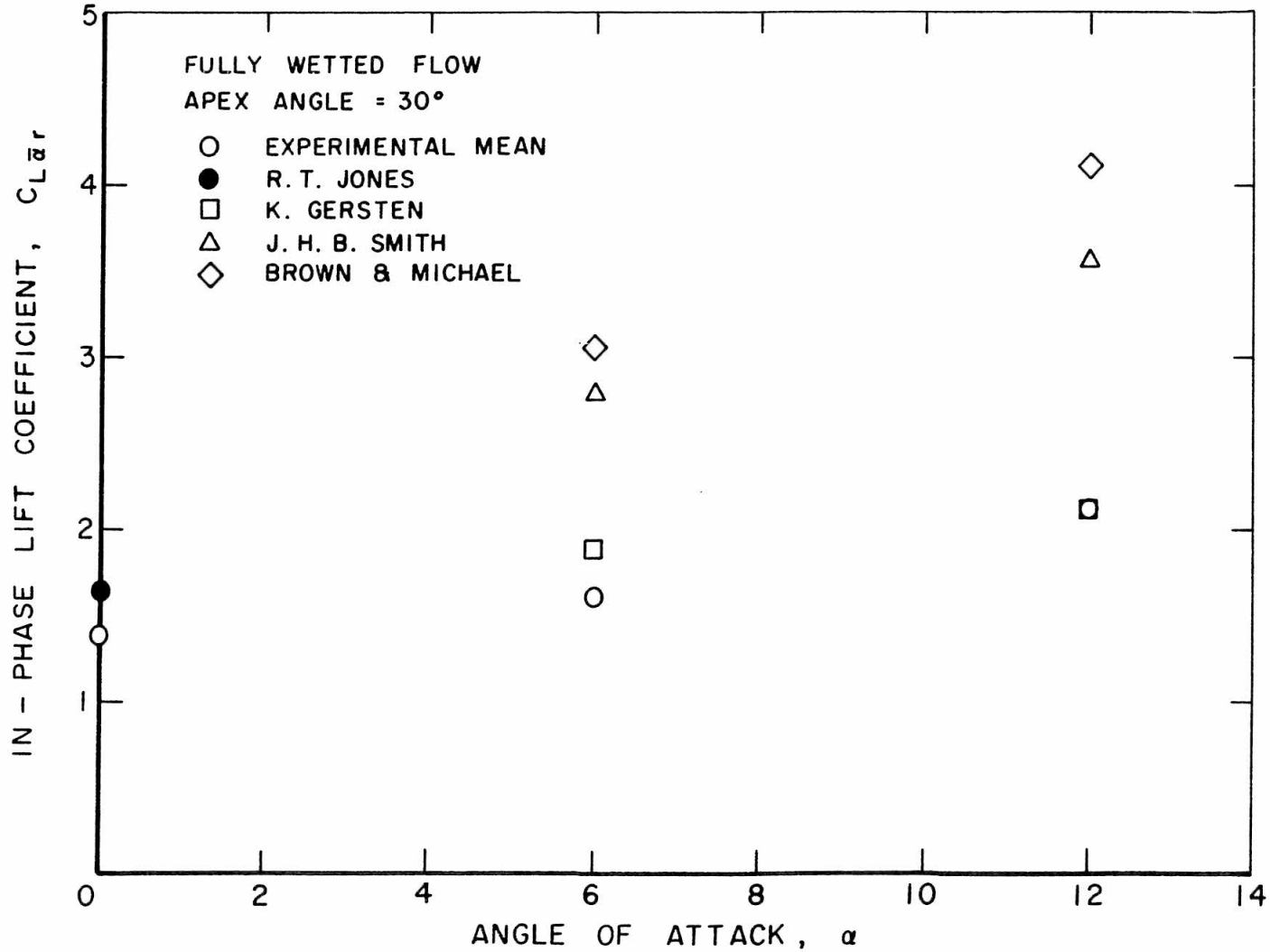

Figure 45 - Summary of steady theories calculated for the 30° delta wing and compared to the experimental in-phase lift coefficients.

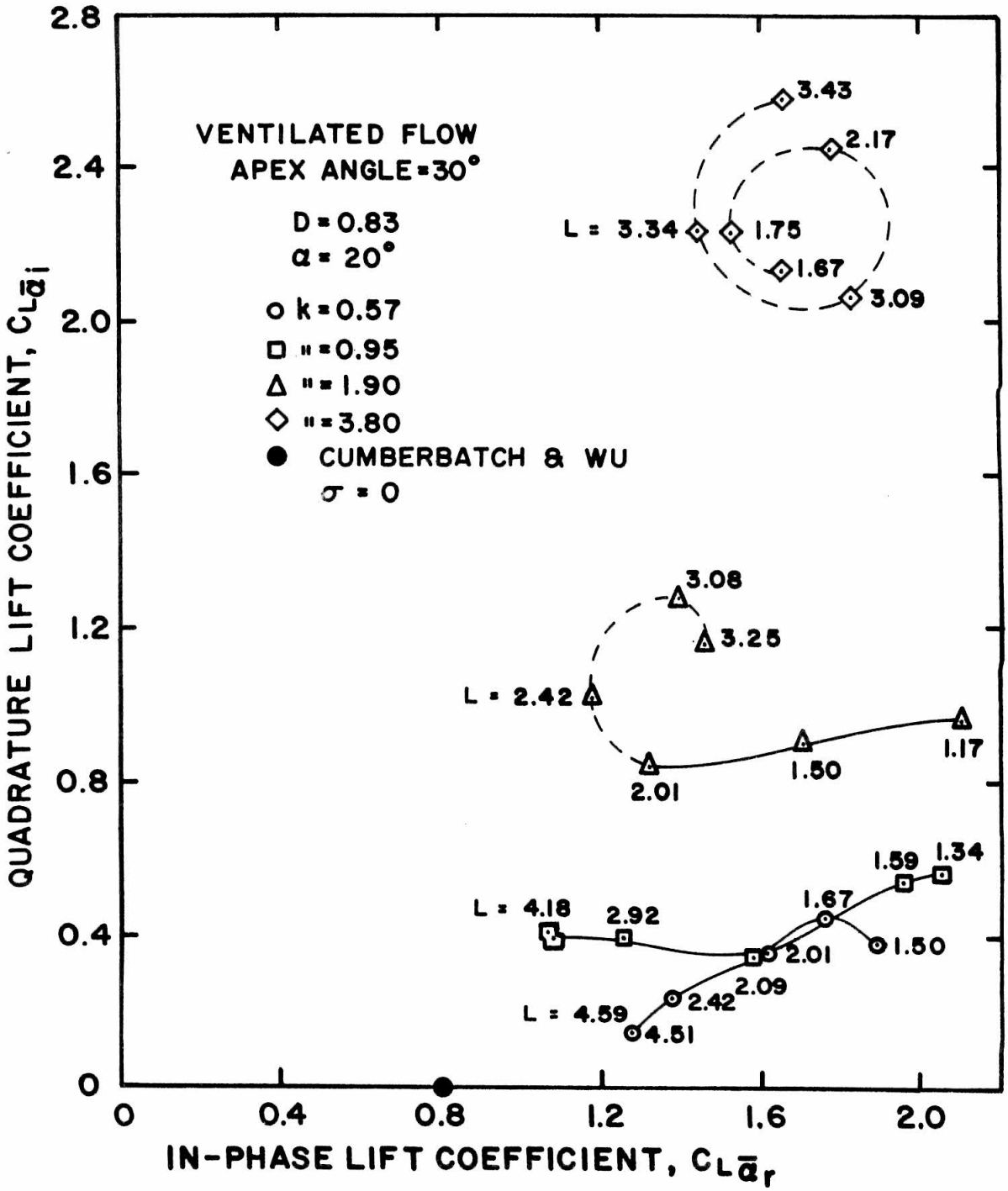

Figure 46 - Unsteady lift coefficients for ventilated flow at four reduced frequencies.

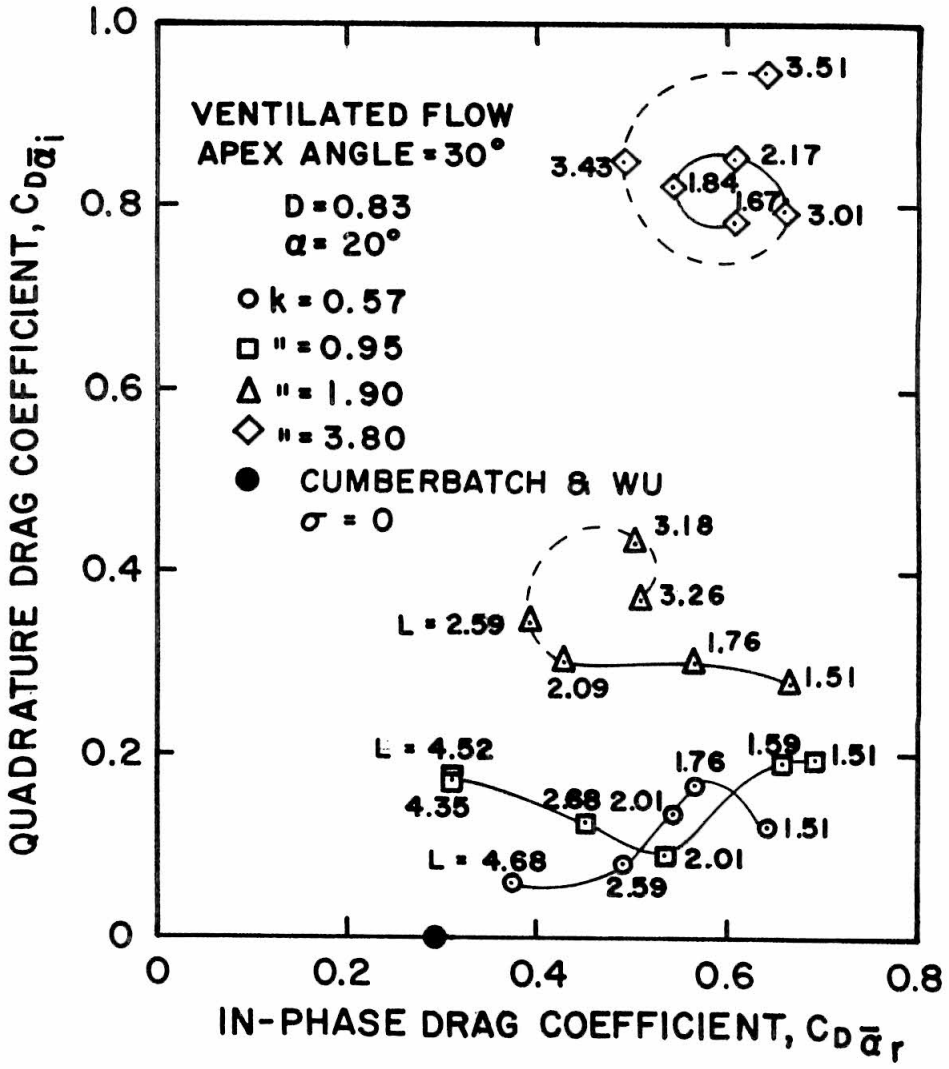

Figure 47 - Unsteady drag coefficients for ventilated flow at four reduced frequencies.

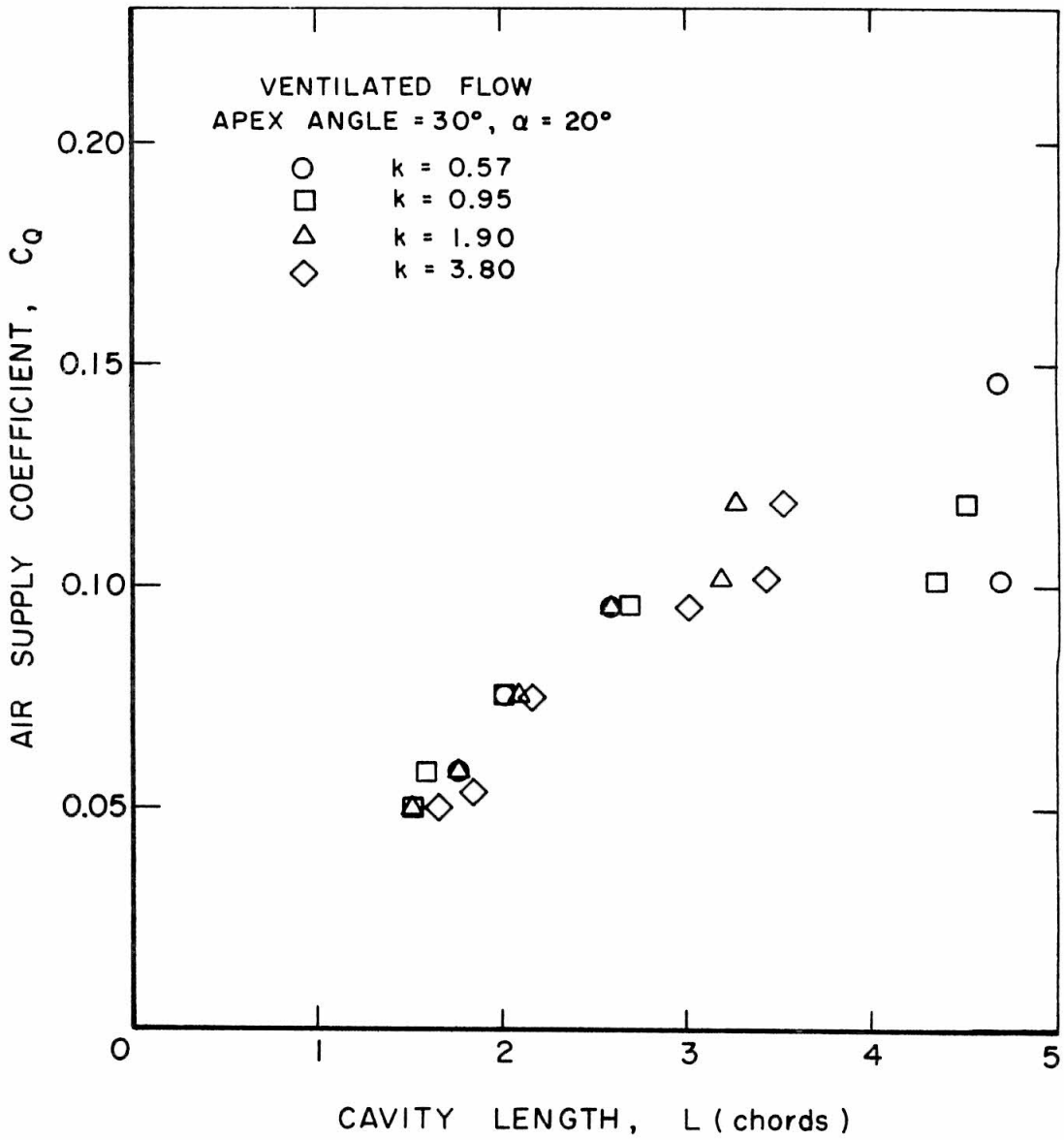

Figure 48 - Air supply coefficient as a function of cavity length showing the effect of reduced frequency.

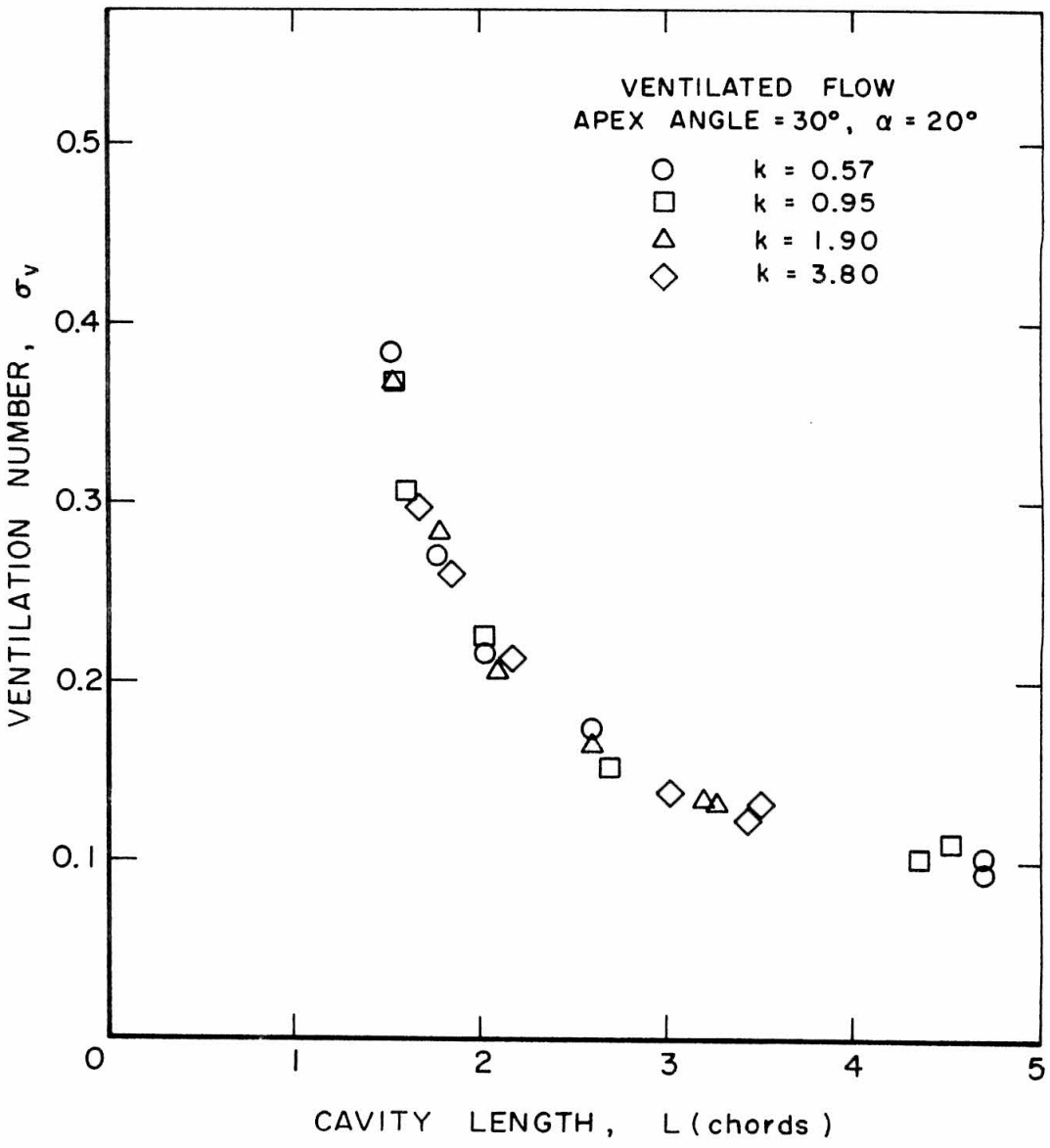

Figure 49 - Ventilation number as a function of cavity length showing the effect of reduced frequency.

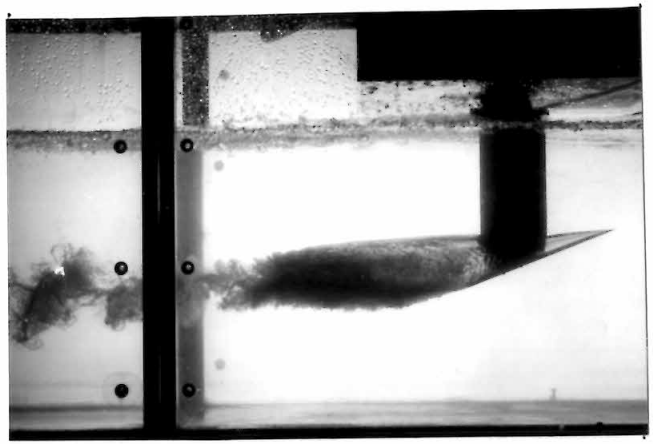

a) k = 0.57, C_Q = 0.086

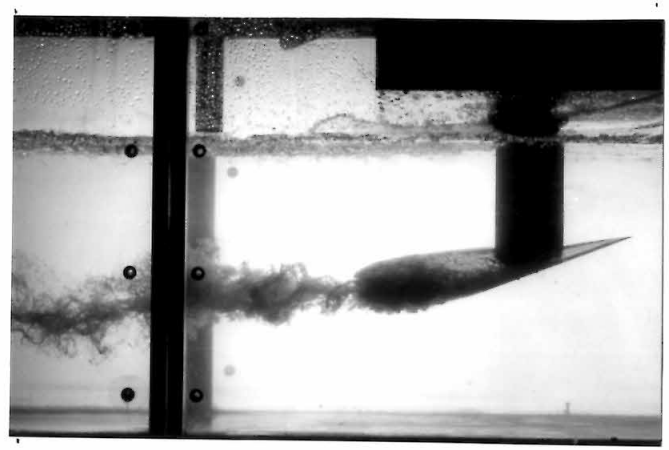

b) k = 1.90, C_Q = 0.055

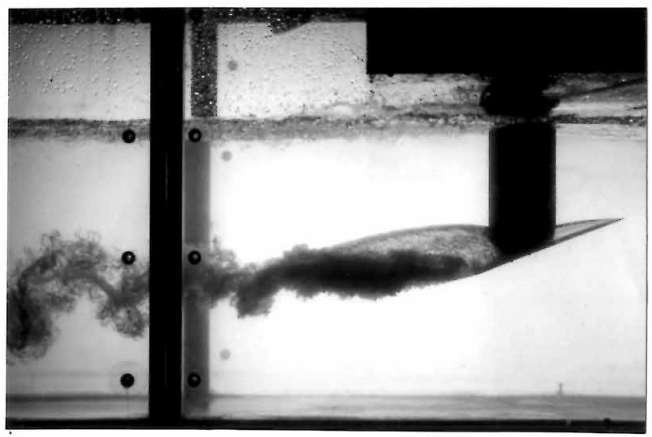

c) k = 3.80, C_Q = 0.065

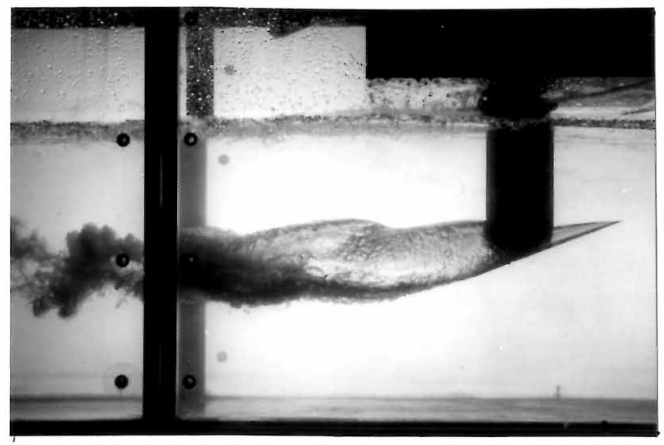

d) k = 3.80, C_Q = 0.110

Figure 50 - High speed flash photographs of the ventilated delta wing.

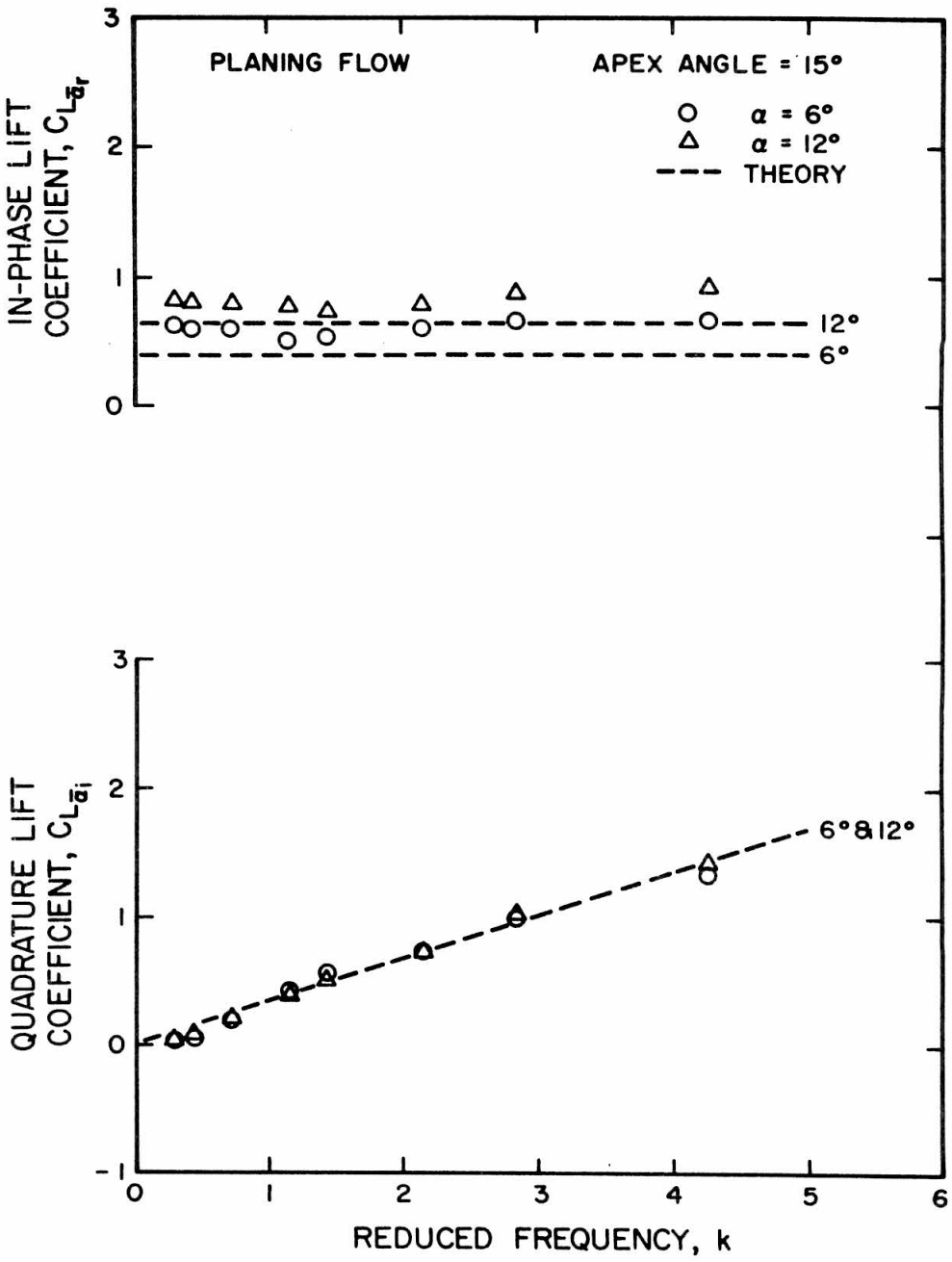

Figure 51 - Unsteady lift coefficients for the planing 15° delta wing.

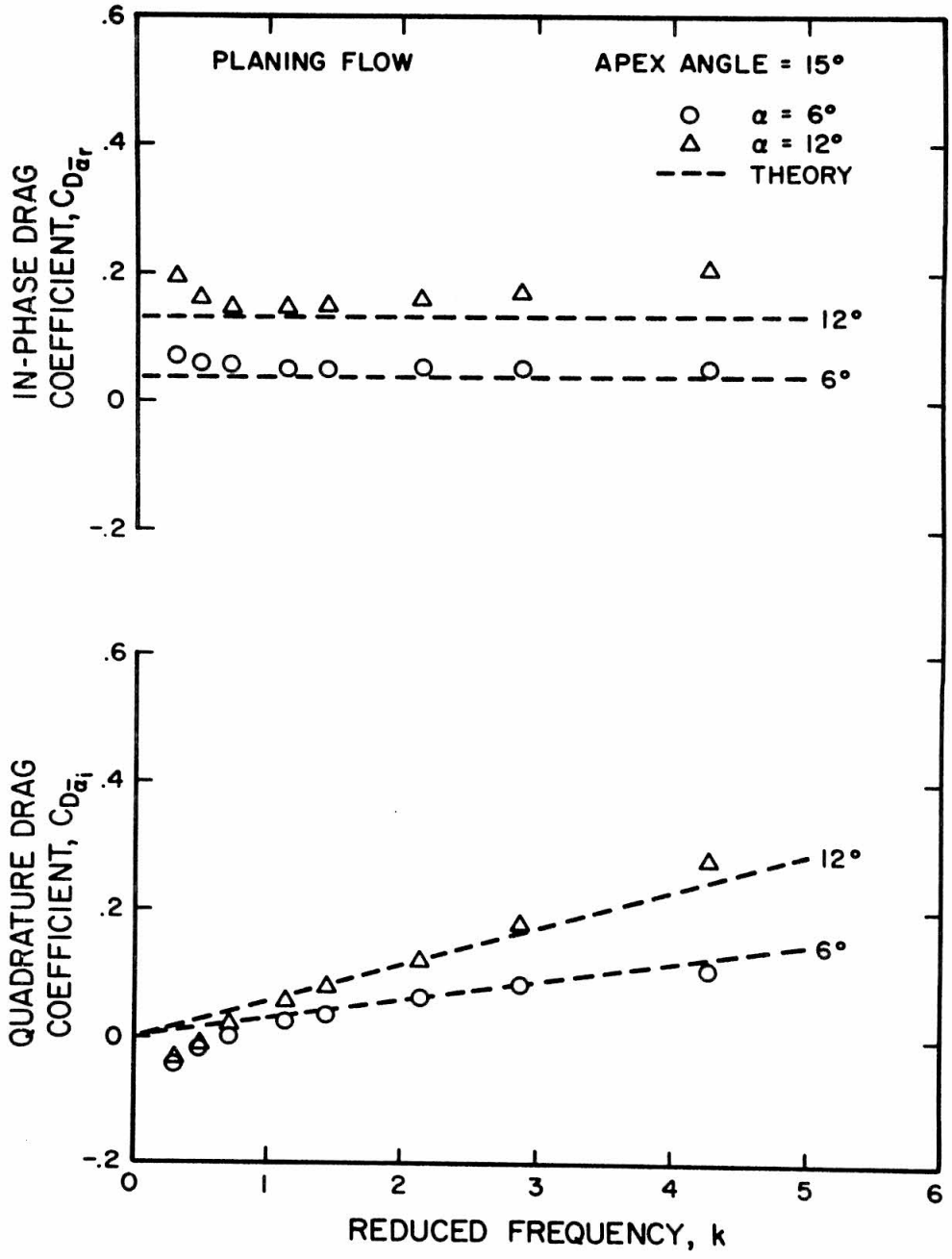

Figure 52 - Unsteady drag coefficients for the planing 15° delta wing.

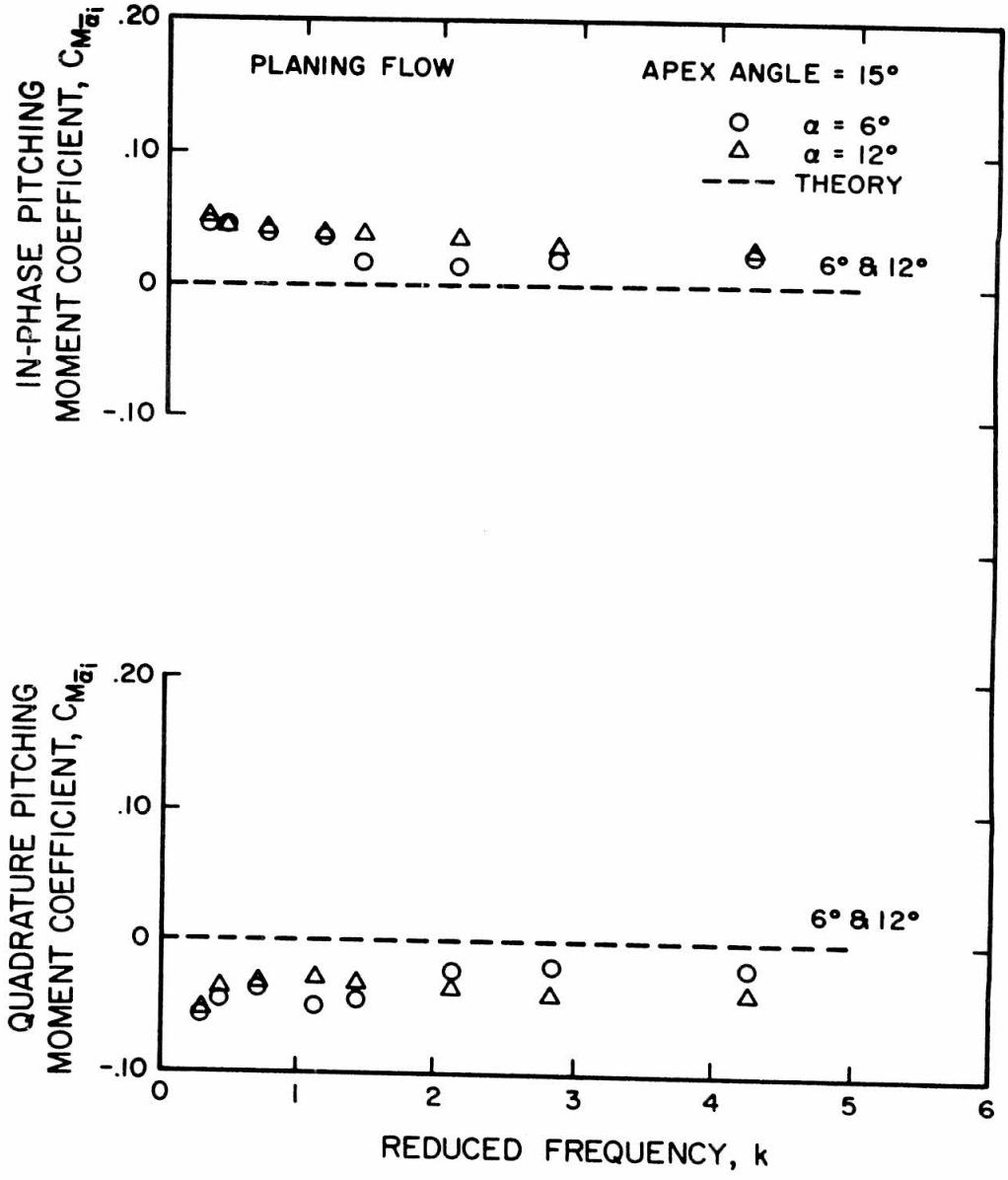

Figure 53 - Unsteady pitching moment coefficients for the planing 15° delta wing.

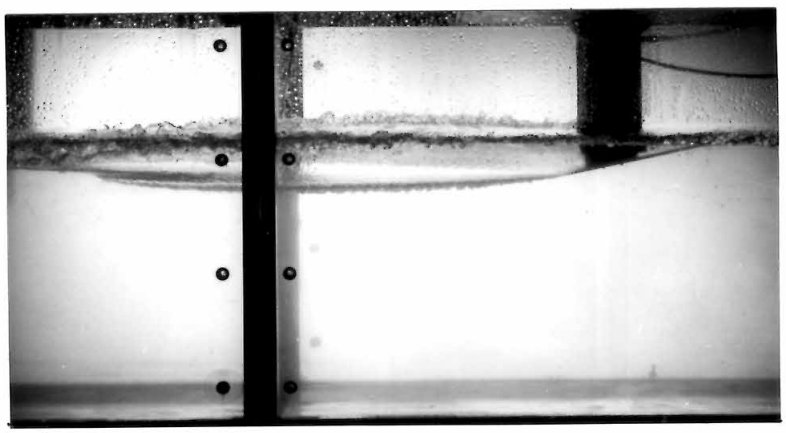

k = 0.0

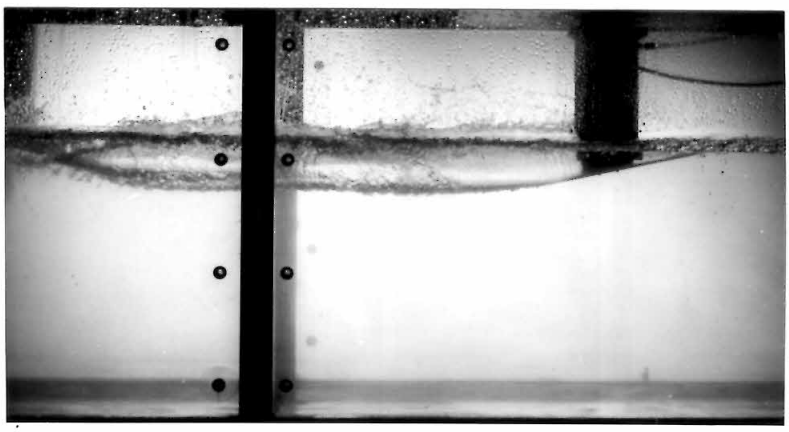

k = 1.42

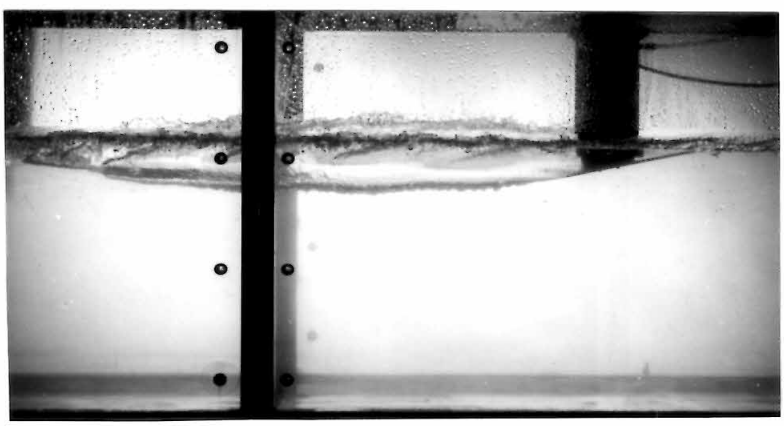

k = 4.27

Figure 54 - High speed flash photographs of the 15° delta wing planing at three different reduced frequencies.

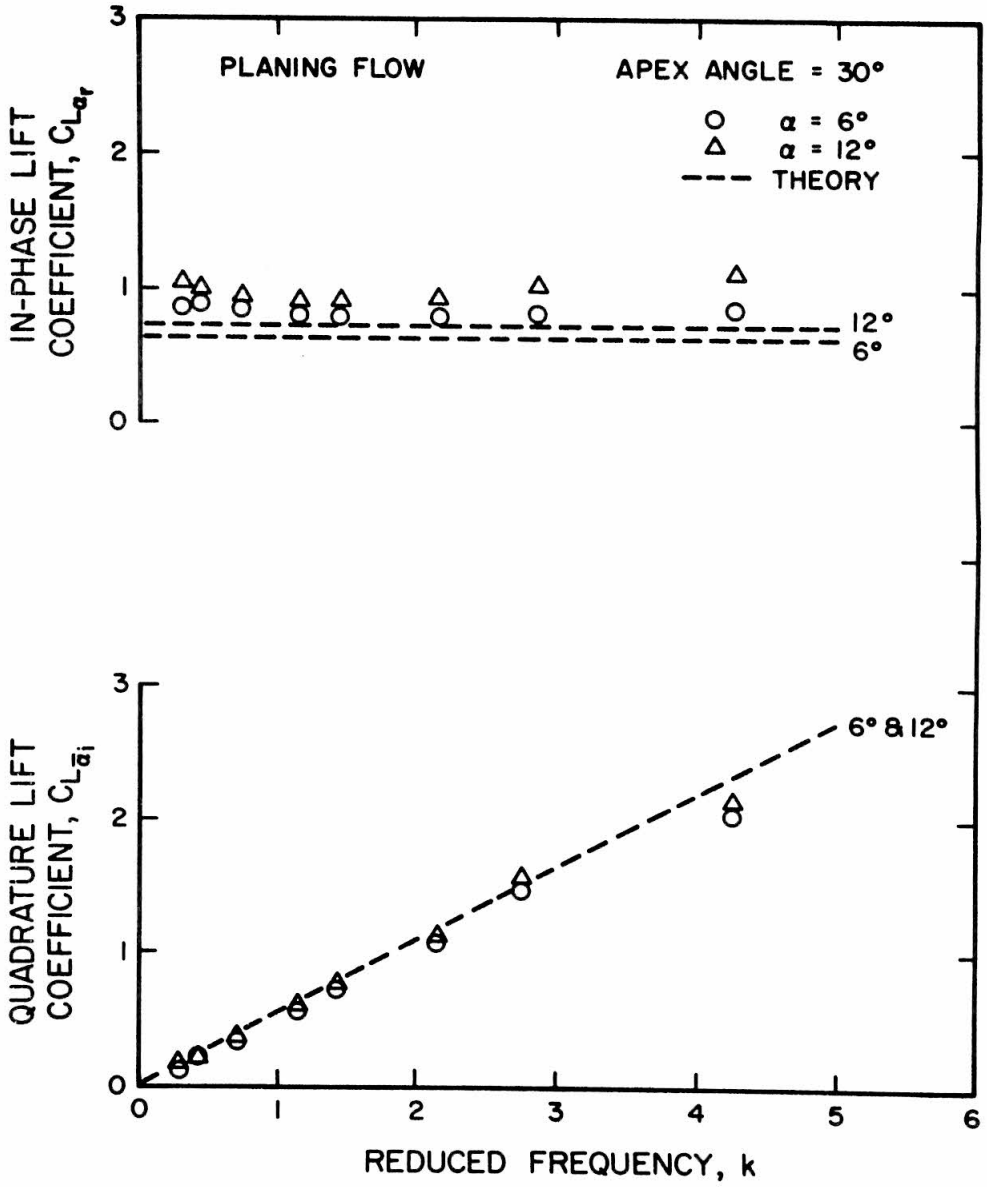

Figure 55 - Unsteady lift coefficients for the planing 30° delta wing.

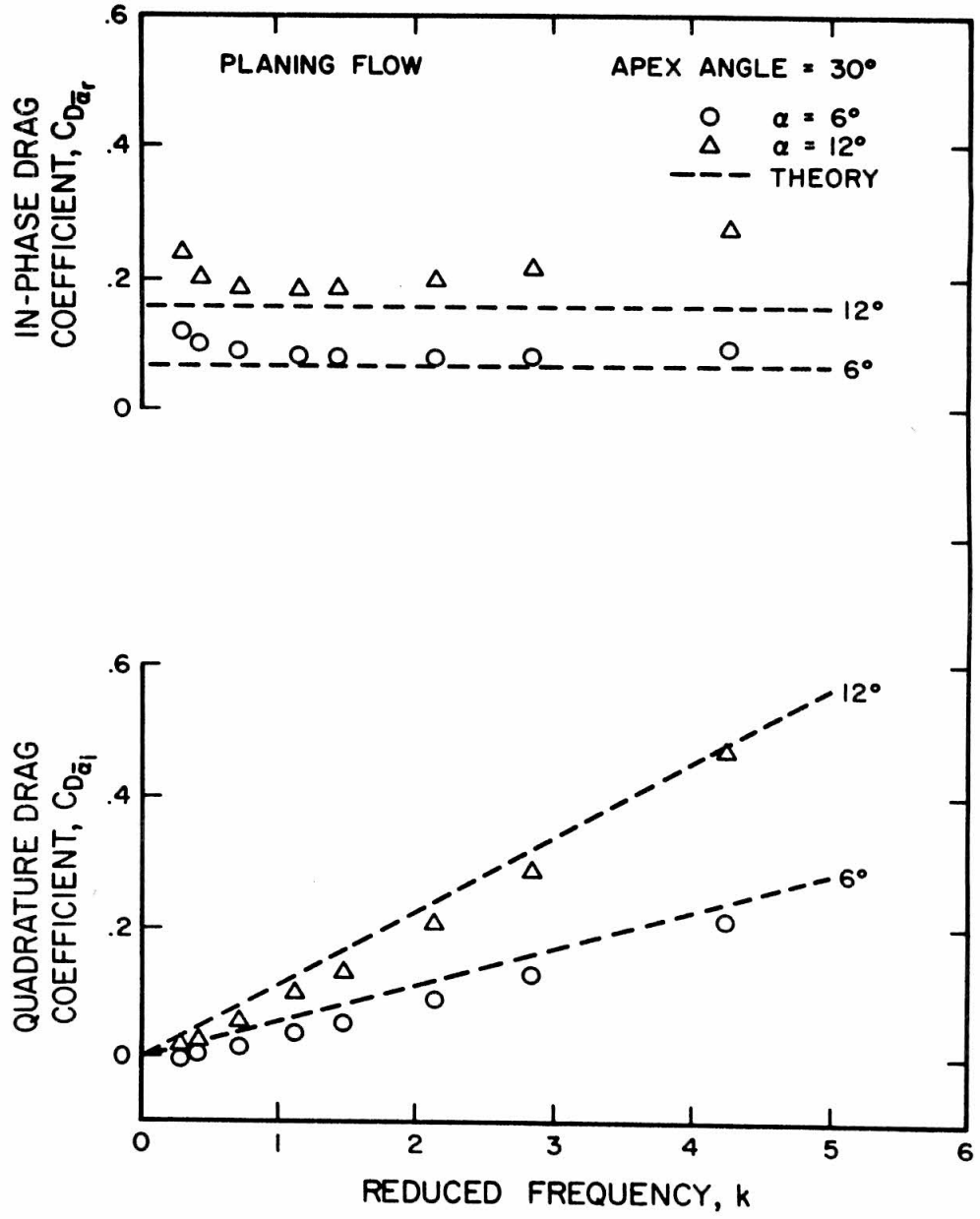

Figure 56 - Unsteady drag coefficients for the planing 30° delta wing.

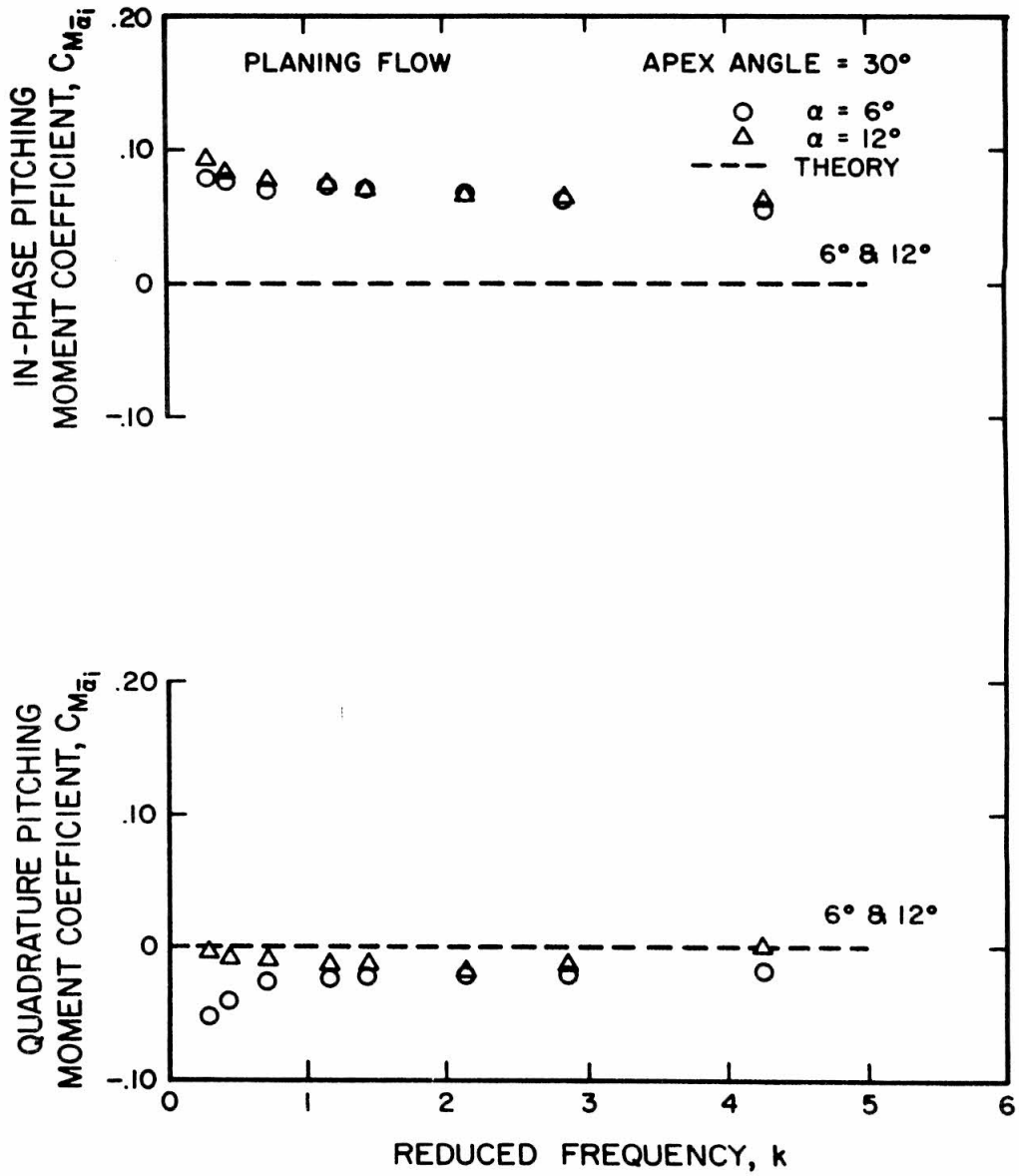

Figure 57 - Unsteady pitching moment coefficients for the planing 30° delta wing.

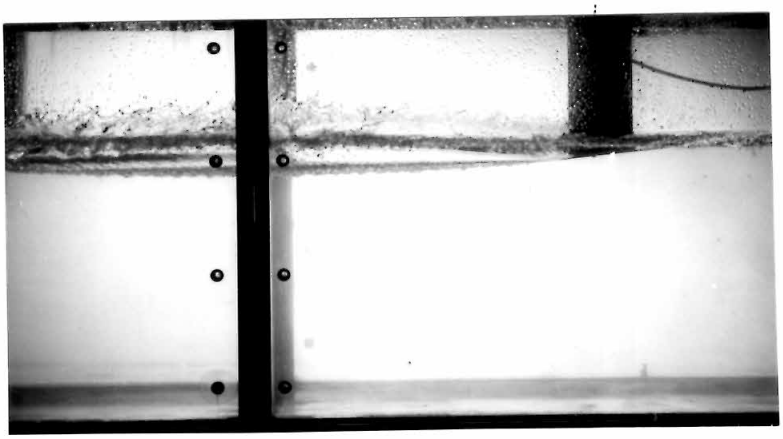

k = 0.0

k = 1.42

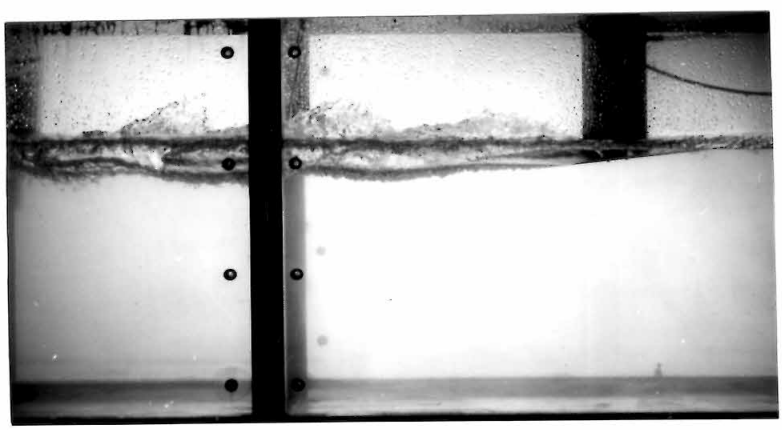

k = 2.84

Figure 58 - High speed flash photographs of the 30° delta wing planing at three different reduced frequencies.

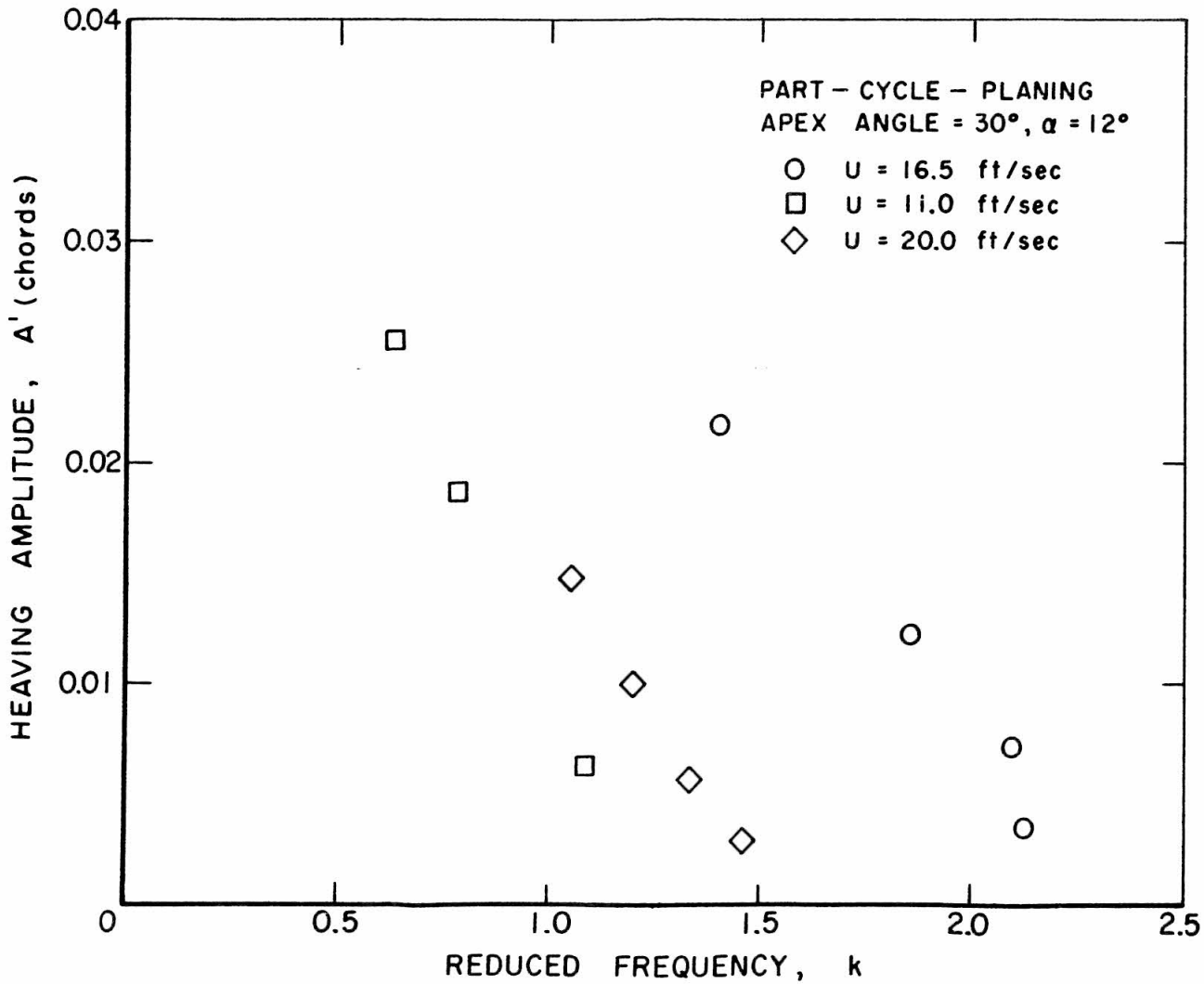

Figure 59 - Oscillation amplitude boundary for neutral stability during part-cycle-planing at three velocities.

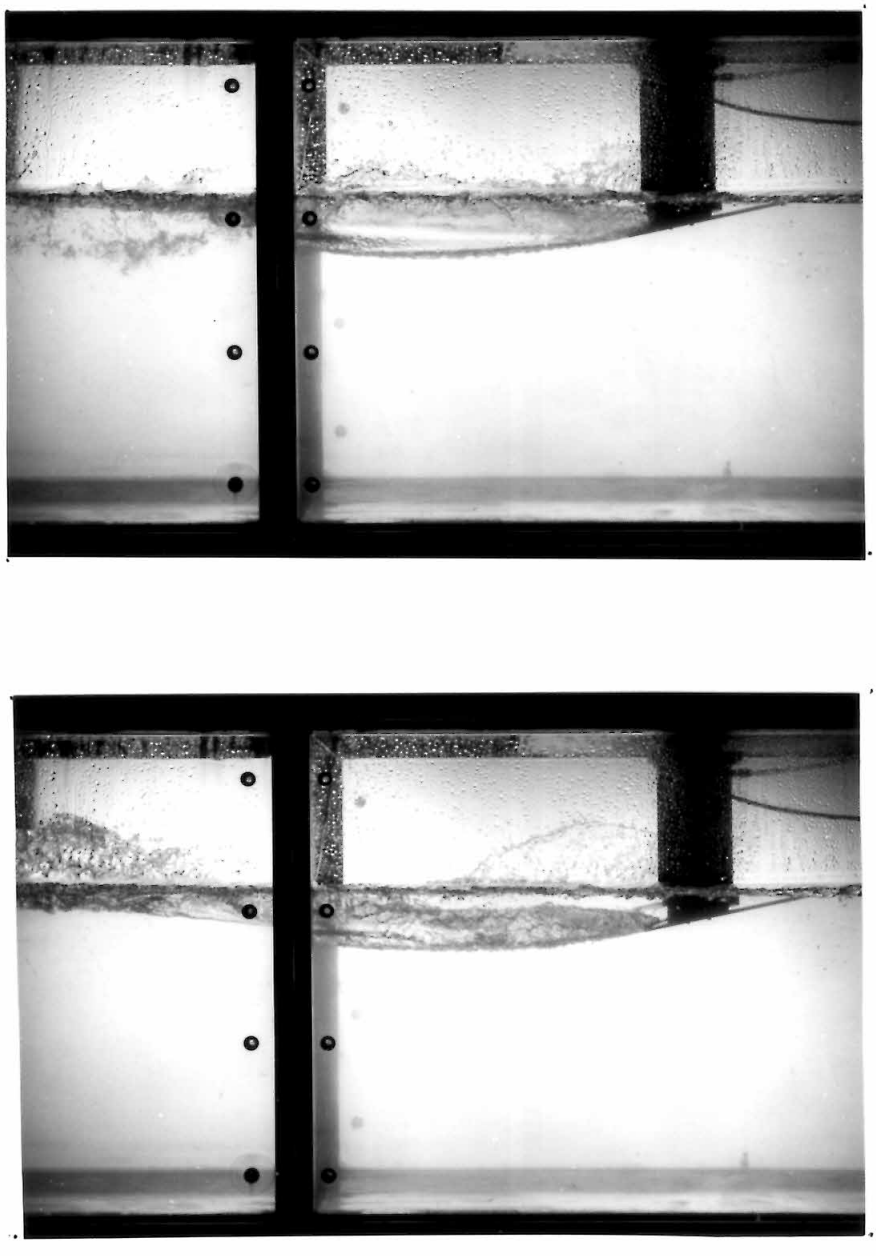

Figure 60 - High speed flash photographs showing examples of part-cycle-planing.

APPENDIX

Symbols and Notation

$a(x)$	local semi-span
A	foil planform area
A'	heaving amplitude
A_n	coefficient defined by equation (75)
b	spray position in reduced coordinates
b_1	$a(x)\, b$
$B(t)$	Bernoulli "constant"
c	model chord length
C	RSA factor
$C_{D_{\tilde{\alpha}}}$	unsteady drag coefficient
$C_{L_{\tilde{\alpha}}}$	unsteady lift coefficient
$C_{M_{\tilde{\alpha}}}$	unsteady pitching moment coefficient about foil planform centroid
C_N	normal force coefficient
C_Q	air supply coefficient (see p. 35)
$\tilde{D}$	processed drag signal
f	reduced perturbation velocity potential
F_1	displacement calibration factor
F_2	velocity calibration factor
F_3	lift calibration factor
F_4	pitching moment calibration factor
F_5	drag calibration factor

k	reduced frequency, $\frac{\omega c}{2U}$; also dummy variable
ℓ	calibration mass offset
ℓ'	tare mass offset
$\tilde{L}$	processed lift signal
m	total calibration mass; also summing index
m'	tare mass
$\tilde{M}$	processed moment signal
n	summing index
N	normal force
p	pressure; also dummy variable
$\vec{q}$	velocity vector in foil coordinates
Q	air supply rate corrected to atmospheric pressure
t	time
U	free stream velocity
$\vec{v}_b$	velocity of foil coordinate system with respect to an inertial system
$\tilde{v}$	heaving velocity amplitude
x, y, z	coordinates attached to foil (see Figure 12)
$y_o(x)$	foil camber function
α	angle of attack
$\bar{\alpha}$	apparent change of angle of attack
β	delta wing apex angle
$\gamma(\xi)$	local vortex strength
δ	ordering parameter

ϵ	$b(\xi) - 1$
ϵ_1	$a(x)\,\epsilon$
ζ	dummy variable
η, ξ	reduced cross-flow plane coordinates (see Figure 13)
θ	dummy variable
ν	defined to be $v_b + U y_o' - U\alpha$
ρ	density of water
σ_v	ventilation number (see p. 35)
τ	dummy variable
φ	perturbation velocity potential
Φ	total velocity potential
ω	oscillation angular frequency

Subscripts

x, y, z, η, ξ, t	differentiation by the subscripted variable (Note: dot above symbol sometimes used for time differentiation and prime sometimes denotes differentiation by argument)
c	cavity conditions
i	component 90^o out of phase with apparent change of angle of attack
r	component in-phase with apparent change of angle of attack
∞	free stream conditions